UNDERSTANDING OCEAN IRON DYNAMICS AND IMPACTS ON MARINE ECOSYSTEMS

A Dissertation
Presented to
The Academic Faculty

By

Anh Le-Duy Pham

In Partial Fulfillment
of the Requirements for the Degree
Doctor of Philosophy in the
School of Earth and Atmospheric Sciences

Georgia Institute of Technology

December 2019

UNDERSTANDING OCEAN IRON DYNAMICS AND IMPACTS ON MARINE ECOSYSTEMS

Approved by:

Dr. Takamitsu Ito, Advisor
School of Earth and Atmospheric Sciences
Georgia Institute of Technology

Dr. Jennifer Glass
School of Earth and Atmospheric Sciences
Georgia Institute of Technology

Dr. Martial Taillefert
School of Earth and Atmospheric Sciences
Georgia Institute of Technology

Dr. Joseph Montoya
School of Biological Sciences
Georgia Institute of Technology

Dr. Thomas Weber
Department of Earth and Environmental Sciences
University of Rochester

Date Approved: October 18, 2019

This dissertation is dedicated to my parents.

ACKNOWLEDGEMENTS

First and foremost, I would like to express the utmost gratitude to my advisor Taka Ito for his advice and support throughout my study at Georgia Tech. Working under his supervision helps me not only grow as a student but also inspire me of the scientist I would like to become. His clear way of thinking, his attention to detail as well as the big picture, and his passion for fundamental problems will always be my role model of a scientist. I am grateful to Thomas Weber for all the fruitful discussions on the trace metal cycling and the ocean inverse model. I also wish to thank Jennifer Glass, Martial Taillefert, and Joseph Montoya for accepting to be my committee members and for their insightful comments on my work. Outside research, I thank Martial for his help extending my I-20, and I have learned from Jen the importance of commitment to diversity and inclusion.

Being a graduate student at Georgia Tech for me is like a window to the new world. I have learned a lot not only from the oceanography classes by Emanuele Di Lorenzo and Annalisa Bracco but also from the discussions on research fields way outside of mine with other graduate students and professors. I thank James Wray, Yuanzhi Tang, Chris Reinhard, Raj Lal, Zijian Li, George Zaharescu, and Fabrizio for teaching me about planetary sciences, atmospheric chemistry, air quality, geology, astrobiology, and machine learning.

I am grateful to members of the oceanography group and my friends in the EAS department. Thanks to Dan, Yohei, Mer, Giovanni, Jackie, Sebastian, Youngji, Daoxun, Filippos, Fabrizio. They welcomed me when I first came to Atlanta and helped me survive my first two years of graduate school. Thanks to Zijian and Sara for being great office-mates. Thanks to Raj for teaching me about the NBA and American culture. Thanks to Guangpeng for the Chinese hot pot.Thanks to Sven for being my fellow at the CRC. Your coming to CRC at 7pm and your one-hour workout on the elliptic running almost every day inspires me a lot about discipline and commitment. Thanks to Olivia, Laura, Natasha, Jason, Mark, and other EAS staff members. I have been bothering them with computer problems and

paperwork issues for more than five years. You all make Atlanta my true home.

I am in debt to my family for their boundless love and support. My parents encouraged me to study abroad, even half the globe away, despite them being alone. My brother introduced me to oceanography and earth sciences when I was still in high school. He also inspired me to pursue a Ph.D. in the US. He teaches me a lot on chemistry and writing and gives me advice every time I struggle.

Finally, I cannot say thank enough to my wife, Huyen. A long-distance relationship is hard, not to mention doing that half the globe away for five years and with a 12-hour difference. I will always be grateful to her for staying strong through those years. She has been patiently listening to me talking about oceanography, earth sciences, and a lot of times about my other interests such as philosophy and religion, the stuffs that have no relation to her own interests. I am also grateful to her for making me smile during difficult times. Above all, her love is my greatest source of joy.

TABLE OF CONTENTS

LIST OF TABLES

LIST OF FIGURES

LIST OF SYMBOLS AND ABBREVIATIONS

Fe Iron

dFe Dissolved iron

P Phosphorus

N Nitrogen

Massachusetts Institute of Technology general circulation MITgcm

Estimating the Circulation and Climate of the Ocean ECCO

Parekh et al. 2005 P05

Dutkiewicz et al. 2005 D05

Dissolved inorganic carbon DIC

Phosphate PO_4^{3-}

Dissolved organic phosphorus DOP

Oxygen O_2

Tagliabue and Völker 2011 TV11

Misumi et al.2013 M13

Dissolved organic carbon DOC

Apparent Oxygen Utilization AOU

Carbon C

OGCBMs Ocean General Circulation Biogeochemistry Models

silica Si

Nitrate NO_3^-

High-Nutrient Low-Chlorophyll HNLC

SUMMARY

Fe is one of the most important nutrients for phytoplankton growth in the ocean, making it a crucial element in the regulation of the ocean carbon balance and biogeochemical cycles. Atmospheric deposition of dFe to the ocean has increased over the last decades partly due to human activities, which can significantly alter marine ecosystems. Thus, a comprehensive understanding of how the ocean Fe cycling operates and how it will respond to human perturbations is urgently needed. In this work, I first significantly improve the Fe parameterization in a global ocean biogeochemistry model, constrained by new high-quality ocean Fe datasets. Then, I identify key mechanisms that control the ocean Fe cycle in various ocean basins and examine the responses of marine phytoplankton to an increasing Fe deposition through a suite of model simulations. These simulations are performed in an ocean biogeochemistry and an ecosystem models, which incorporate the newly improved Fe scheme.

The refinement of model Fe parameterization and its evaluation are undertaken in chapters two to four. In these chapters, I show that my newly developed Fe scheme displays a remarkable improvement in reproducing observations over the old scheme. Through a suite of model simulations, I reveal the crucial role of the concurrent release of dFe and ligands from sinking organic particles in forming and maintaining the subsurface dFe maxima observed in many ocean transects. Moreover, the inclusion of spatially varying ligand classes with different binding strengths in the model is important to explain the strong vertical dFe gradient observed in the upper ocean. I also identify the relative roles of different external dFe sources in different ocean basins. While atmospheric deposition is an important source of dFe in the Atlantic and Indian Oceans, sedimentary and hydrothermal dFe inputs are more important in the Pacific Ocean.

The relative contributions of external sources and ocean interior processes on regulating the upper ocean dFe pattern are explored in chapter five. This task is done by analyzing the

dFe budget and the dFe distribution field simulated in different ocean Fe models, using an unsupervised classification technique. The results show that the upper ocean dFe patterns are largely controlled by interior ocean processes and that without an appropriate representation of these processes, Fe models cannot reproduce observations, even with a correct magnitude of the external fluxes.

In chapter six, I explore the impact of an increasing dFe atmospheric deposition on the Indian Ocean phytoplankton and carbon balance by using an ocean ecosystem model, which incorporates the newly improved Fe scheme. I found that while diatom growth and export organic carbon flux are enhanced south of 40°S, they decrease in some regions in the northern Indian Ocean, compensated by increases in coccolithophores growth and carbonate carbon export. These changes lead to a decrease in the carbon dioxide uptake over the Indian Ocean.

CHAPTER 1
INTRODUCTION

1.1 Ocean iron cycling

The ocean Fe cycle presents an intriguing and unique paradox. Fe is the fourth most abundant element in the Earth's crust and is essential for various processes involved in the growth of phytoplankton such as those linked with photosynthesis, respiration, and nitrogen fixation (Raven, 1988; Tagliabue et al., 2017). However, the dFe (operationally defined by the filter size of $< 0.2\mu$m) concentration in the ocean is extremely low, on the order of subnanomolar level ($10^{-6}mol/l$) (Liu and Millero, 2002). This is because of the tendency of Fe to hydrolyze and precipitate out of the water column and to be scavenged by marine particles (Blain and Tagliabue, 2016). For this reason, biological productivity in around half of the world ocean is restricted by the availability of dFe (Moore et al., 2013). Moreover, the low concentration of dFe makes its measurements in the ocean difficult, limiting our high-quality Fe data (Blain and Tagliabue, 2016). It was not until recent years that developments in measurement techniques and international efforts helped expand the dataset of ocean dFe distribution (Tagliabue et al., 2016, 2012). This expanding dataset has revealed important processes of ocean Fe cycling that have been previously overlooked (Schlitzer et al., 2018).

Oceanic Fe cycling (Figure 1.1) is distinct from those of major nutrients like P and N because of the involvement of a diverse and complex array of processes (Tagliabue et al., 2017). First, there are several external sources of dFe to the ocean. Although it was previously considered that atmospheric deposition is the only major source of dFe (Archer and Johnson, 2000; Johnson et al., 1997), new observations demonstrate that continental shelves (Elrod et al., 2004; Johnson et al., 1999) and hydrothermal vents (Fitzsimmons

and Boyle, 2014; Resing et al., 2015; Tagliabue et al., 2010) also release a considerable amount of dFe. Second, Fe exists in various forms in the ocean. The most thermodynamically stable form of Fe in the oxygenated seawater is the ferric (Fe(III)) species, which has very low solubility and precipitates quickly to form particulate Fe (Moore et al., 2013). Fe can also be attached to marine particles through biological uptake, coagulation of colloidal Fe (defined by the filter size between 0.02 - 0.2μm), and scavenging (Revels et al., 2015). Whereas previous studies focused on the scavenging role of biogenic (organic) particles (Parekh et al., 2005), recent studies have argued for scavenging by particles with lithogenic (inorganic) origin, especially in high dust regions (Ye and Völker, 2017). Particulate Fe can aggregate and gravitationally sink through the water column (Fowler and Knauer, 1986; Jeandel et al., 2015). Some of the particulate Fe can return to dissolved form along the sinking pathway through desorption and particle remineralization (Boyd et al., 2000). Remineralized Fe can be scavenged again or transported back to the surface via upwelling and vertical mixing (Tagliabue et al., 2014a).

However, studies by Rue and Bruland, (1995), Berg, (1995) and Wu and Luther, (1995) showed that the majority of dFe in seawater ($\sim$ 99%) is protected from scavenging and precipitation by binding with organic ligands. The crucial role of ligands for the ocean Fe cycling leads to measurements of their concentration in the ocean (Boye et al., 2001; Ibisanmi et al., 2011) as well as their inclusion in Fe modeling studies (Parekh et al., 2005; Völker and Tagliabue, 2015). A traditional and still widespread approach in ligand modeling is to assume a uniform distribution and a constant concentration of 0.6 or 1 nM for the most dominant ligand observed in the ocean (Parekh et al., 2005). Recent ligand observations (Buck et al., 2018; Gerringa et al., 2016) challenge this assumption and suggest a large variation in the ligand concentration and a spectrum of ligand classes with different binding strengths with dFe (Hassler et al., 2017).

The new dFe datasets also showed unique features of the ocean dFe pattern that are not correctly represented in many ocean biogeochemistry models (Tagliabue et al., 2016).

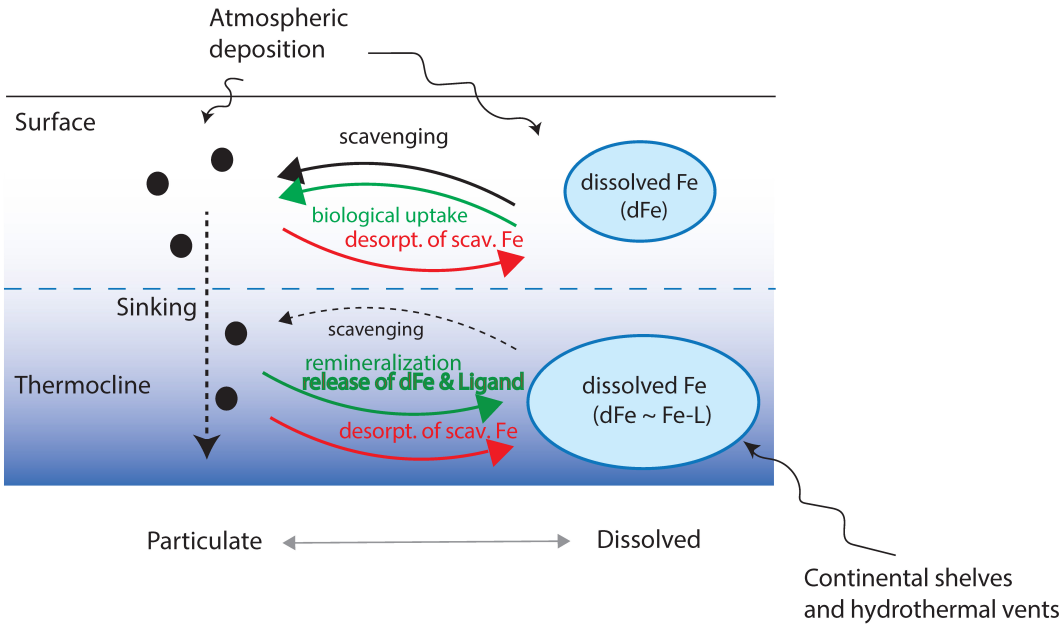

Figure 1.1: Schematic depiction of ocean dFe cycling. The schematic shows the interaction and transformation between dissolved (on the right side) and particulate (on the left side) forms of Fe. dFe enters the ocean through atmospheric deposition, continental shelves, and hydrothermal vents. Atmospheric deposition supplies both particulate and dissolved Fe.

Among these features are the subsurface ($\sim$ 300-1000m) dFe maxima observed in several GEOTRACES ocean transects (Hatta et al., 2015; Rijkenberg et al., 2014), which could be an important source of dFe to phytoplankton in the euphotic zone. These subsurface maxima tend to be underestimated in ocean models that used the Fe parameterization following Parekh et al., (2005), which was developed when the ocean Fe observations were still sparse. This parameterization applied traditional approaches which assumed only one uniformly distributed ligand class and considered atmospheric deposition as the only dFe source. Biases in the model Fe distribution hinder our projection of changes in ocean productivity and hence the ocean carbon balance and climate system under the impact of human perturbations, among which is the increasing anthropogenic atmospheric dFe input to the ocean (Jickells et al., 2005). Moreover, ocean acidification, stratification, warming, and deoxygenation are expected to cumulatively alter the bioavailability, chemistry, recycling, and particle dynamics of Fe (Hutchins and Boyd, 2016). Consequently, it is crucial to improve the Fe parameterization in ocean biogeochemistry models, examine processes regulating the ocean Fe dynamics, and evaluate their responses to future changes. The new Fe dataset from the GEOTRACES program provides a unique opportunity to achieve these tasks.

1.2 Objectives of this dissertation

In this dissertation, I first aim to improve the Fe representation in an ocean biogeochemistry model, which still uses the parameterization developed by Parekh et al., (2005), and test the ability of this representation to reproduce the dFe distributions observed in GEOTRACES ocean transects. Then, I aim to answer three scientific questions:

- (I) What are mechanisms supporting the formation and maintenance of the subsurface dFe maxima observed in various GEOTRACES transects?
- (II) What are the relative contributions of external sources versus internal processes

in controlling the upper ocean (0-1000m) dFe pattern?

- (III) What are the impacts of an increasing anthropogenic atmospheric dFe deposition on nutrient distribution, phytoplankton production, and carbon uptake of the ocean?

The modeling improvements and validations are undertaken in chapter 2 and chapter 3. Questions (I) and (II) are partly addressed in chapter 3 and chapter 4 through a suite of model simulations. Chapter 5 provides further insight on question (II) by analyzing the balance of dFe budgets simulated in different Fe models using a statistical method. Question (III) is addressed in chapter 6 by coupling our Fe cycling scheme to a state-of-the-art ocean ecosystem model (Dutkiewicz et al., 2014), focusing on the Indian Ocean, where the phytoplankton community is diverse and can significantly respond to perturbations. Chapter 7 summarizes the results of this work, discusses their implications, and suggests important questions for future research.

CHAPTER 2

MODEL DESCRIPTION

The ocean biogeochemistry model used in this study is based on the MITgcm model (Marshall et al., 1997a,b), configured for a global bathymetry in a 1°x1°longitude-latitude grid and 23 non-uniform vertical z-levels. At this resolution, mesoscale eddies are parameterized using the isopycnal tracer and thickness diffusion scheme (Gent and McWilliams, 1990; Redi, 1982; Solomon, 1971) and the mixed-layer processes are parameterized using the K-Profile Parameterization scheme (Large et al., 1994). The model is run offline, using the climatological monthly circulation fields taken from the ECCO product version 3 (Wunsch and Heimbach, 2007). The biogeochemical component of the model is modified from Parekh et al., (2005) and Dutkiewicz et al., (2005) (hereafter P05 and D05), which carries DIC, alkalinity, PO_4^{3-}, DOP, dFe, and O_2. Biological productivity is controlled by the availability of light and nutrients (PO_4^{3-} and dFe) using Monod function. There are some notable differences in the parameterization of the Fe cycling relative to the earlier versions of MITgcm in P05 and D05, as described in details below. Values for all model parameters are provided in table 2.1.

In this study, the biological Fe uptake in the subarctic Pacific and Southern Oceans can be varied as a function of the dFe concentration, which represents the luxury Fe uptake of diatoms in these regions where silica is abundant (Ingall et al., 2013). In addition, I include three external sources of dFe (atmospheric deposition, continental shelves, and hydrothermal vents) as opposed to only atmospheric deposition as in P05 and D05.

2.1 Atmospheric Dust Deposition

Atmospheric deposition of dFe under pre-industrial condition is obtained from recent modeling studies, which employed the three-dimensional atmospheric chemical transport model

GEOS-Chem coupled with a comprehensive dust-Fe dissolution scheme (Ito et al., 2016; Johnson and Meskhidze, 2013). The solubility of dust Fe varies spatially. The majority of the deposited dust Fe is likely in the insoluble form especially in the high dust region. Ocean biogeochemistry models tend to overestimate the surface dFe concentration under high-dust regions in the Indian and tropical Atlantic Oceans if a uniform solubility is used (Tagliabue et al., 2016). Thus, I manipulate the solubility of dust Fe for these regions, reducing it by two orders of magnitude. I acknowledge the limitation of this approach and are aware of a new approach from Ye and Völker, (2017) by explicitly solving for lithogenic particles, however there is still large uncertainty in the dissolution kinetics of particulate dust Fe (Mahowald et al., 2009) and in the magnitude of dust deposition itself (Anderson et al., 2016).

2.2 Shelf Sediments

The input of dFe from sea-floor sediments is calculated by following Moore and Braucher, (2008). The essence of this parameterization is to represent the release of Fe from unresolved continental shelves in the coarse resolution ocean model. To do so, I first estimate the biological productivity over the continental shelves using remotely sensed ocean color data (Behrenfeld and Falkowski, 1997). Second, I calculate the e-ratio as a function of total productivity and sea surface temperature, following Laws et al., (2011), and assume a parameterized remineralization profile below the euphotic layer (Martin et al., 1987) to estimate the sinking organic flux at the depths of continental shelves using the ETOPO2 (2-min global ocean bathymetry). The sedimentary dFe flux is then calculated and mapped onto the coarse-resolution model grid points based on a ratio with the organic carbon flux (Elrod et al., 2004). This ratio was measured at a few upwelling locations and did not take into account the effect of the bottom O_2 concentration, which likely leads to an overestimation of the sedimentary dFe flux when applied globally. Dale et al., (2015) addressed this problem by calculating the sedimentary dFe input as a function of carbon oxidation rates

and bottom water O_2 concentrations. Following this approach, I use the O_2 concentration from the World Ocean Atlas O_2 data (Garcia and Gordon, 1992) to vary the ratio used by Elrod et al., (2004) between different regions. Specifically, this ratio is set to 0.68 $\times 10^{-3}$, which is the same as in Elrod et al., (2004) for the low-O_2 waters ($[O_2] < 30$ μM) but is reduced by 1 order of magnitude for well-oxygenated regions ($[O_2] > 30$ μM).

2.3 Hydrothermal Vents

The hydrothermal dFe flux is scaled with ^{3}He flux, following Tagliabue et al., (2010) with some modifications. Previous work reported the mismatches of hydrothermal dFe signals between state-of-the-art Fe biogeochemistry models and observations (Tagliabue et al., 2016; Tagliabue and Resing, 2016), especially along the slow-spreading ridges (Saito et al., 2013). The coefficient relating the hydrothermal dFe to ^{3}He fluxes is unlikely a uniform constant, thus I vary it for different ocean basins. The same ratio as in Tagliabue et al., (2010) is used for the Southern Ocean, but is increased by a factor of 80 in the Atlantic Ocean as suggested by Saito et al., (2013), and by a factor of 10 and 10^3 for the Indian and Pacific Oceans, respectively, to better match observations (Nishioka et al., 2013; Resing et al., 2015).

The vertical profile of horizontally integrated dFe fluxes into the ocean from all three sources in the model is shown in Figure 2.1. Atmospheric dust deposits $\sim$ 100 mol dFe/m/s into the surface water, while hydrothermal vents release dFe mostly at water levels from 2000 to 4000m ($\sim$ 200 mol dFe/m/s) and very little elsewhere. Shelf sediments supply a significant amount of dFe in the upper 1000m water (nearly 400 mol dFe/m/s in the upper 200m). Of the three external dFe inputs, sedimentary dFe flux is the most significant source (37.65 Gmol dFe/year) even though it is confined near coastal regions, whereas dust dFe flux is least significant (2.03 Gmol/year), but it is an important source of dFe to the surface open ocean.

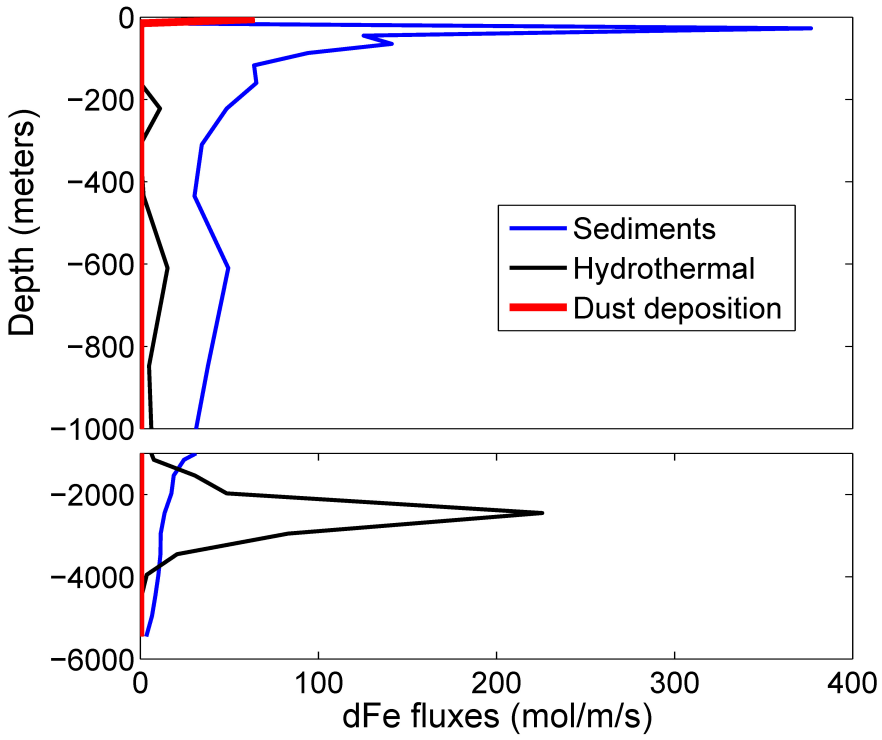

Figure 2.1: The vertical profile of horizontally integrated dFe fluxes from shelf sediments, hydrothermal vents, and dust deposition into the ocean in the model

2.4 Organic Ligands

Following previous studies by Tagliabue and Völker, (2011) and Misumi et al., (2013) (hereafter TV11 and M13), I parameterize multiple, spatially-varying ligand classes as functions of DOC and AOU. These ligand classes have different binding strengths to the free dFe in the seawater. This approach is an improvement from the previous studies of P05 and D05 which used a single, uniform organic ligand. In this dissertation, I essentially consider three ligand classes (L_1, L_2, and L_3). Of the three ligands, L_1 is considered to have the strongest binding strength (K_{L1} = 10^{12} L/mol), while L_2 and L_3 have weaker binding strengths (K_{L2} = 10^{11} L/mol and K_{L3} = 10^{10} - 10^{11} L/mol). Based on previous studies, I assume that L_1 is primarily composed of the biologically produced siderophores with relatively high conditional stability constant (K_{L1} = 10^{12} L/mol) (Adly et al., 2015; Macrellis et al., 2001). L_2 and L_3 are assumed to be primarily composed of humics, which may be produced by the remineralization of the particulate organic matter (Laglera and Berg, 2009; Velasquez et al., 2016; Vraspir and Butler, 2009). The binding strength for humic-like ligand is not certain, as some studies suggested to be $< 10^{11}$ L/mol (Gledhill and Buck, 2012). Recent ligand measurements in the subtropical Atlantic GA03 transect supported the existence of a refractory-DOC component ligand class L_3 with a weak binding strength of K = $10^{10} L/mol$. Based on these assumptions, I parameterize the spatial distributions of L_1 and L_2 as linear functions of DOC and AOU, whereas the highly refractory component of humics DOC (L_3) is represented in the model as a constant background $L_{refract}$ (Hassler et al., 2011) (eqs 2.1 - 2.3).

$$L_1 = \alpha[DOC_{labile}] \tag{2.1}$$

$$L_2 = \gamma\beta[AOU] \tag{2.2}$$

$$L_3 = (1-\gamma)[L_{refract}] \tag{2.3}$$

α is calibrated based on the observed surface ligand and labile DOC distributions along the GA02 western Atlantic transect, where I assume the observed minimum DOC as the proxy for the labile component of DOC (Gerringa et al., 2015; Middag et al., 2015; Salt et al., 2015). The empirical coefficients for L_2 and L_3 (β and γ) are calibrated by fitting to the observed ligand distribution along the GEOTRACES transects (Mawji et al., 2015) in a least-square sense. In the model, DOC_{labile} is represented in terms of DOC, and is calculated as DOC_{labile} = R_{CP}DOP, where R_{CP} (set to 120) is the stoichiometric C:P ratio of the organic matter. DOP in the model is generated by photosynthesis and has an e-folding decay timescale of 6 months. The mean magnitude of DOC_{labile} in our model is generally an order of magnitude smaller than the mean magnitude of observed minimum DOC along the GA02 transect ($\sim$ 0.1 μM versus $\sim$ 1 μM), thus I increase the magnitude of α by a factor of 10 in order to reproduce the observed magnitude of L_1. β is calibrated based on the observed subsurface ligand and AOU along two oceanic transects (the GA02 and GA03 - subtropical North Atlantic Ocean) (Buck et al., 2015; Middag et al., 2015; Voelker et al., 2015). AOU is calculated from dissolved O_2, temperature, and salinity data (Garcia and Gordon, 1992). Parameterizing L_2 in terms of AOU leads to an artificial loss of ligand when the subsurface waters upwell to the surface and AOU decreases to zero on the timescale of air-sea O_2 exchange ($\sim$1 month). Although the decay of AOU in the surface waters could be analogous to the photochemical loss of ligands reported in a previous study (Barbeau et al., 2001), I acknowledge that it may cause biases in the ligand parameterization. The binding of these three parameterized ligand classes to free dFe is solved iteratively as described in the subsection 2.4.1 below.

To evaluate our ligand parameterization, the total ligand concentration (L_1 + L_2 + L_3) in the model is compared against available data from the GEOTRACES program along the west Atlantic GA02 (Gerringa et al., 2015) and subtropical Atlantic GA03 transects (Buck et al., 2015) (Figure 2.2). I focus only on the comparison for the upper 1000m ocean since the dFe and ligand patterns here have more impact on the marine productivity than

the abyssal ocean. Along the GA02 transect, our ligand parameterization is able to capture the right magnitude of the total ligand concentration in this region ($\sim$ 2.0 nM) and some features of the ligand pattern such as the high ligand concentration in the subsurface water (600 - 1000m) near the equator and near the surface around 50°N. Along the GA03 transect, our model significantly underestimates the magnitude of the total ligand concentration by two times (note the difference in the scale for observations and model for this transect - Figure 2.2, lower panels). However, the observed ligand pattern in this transect is generally reproduced by our model such as the high ligand concentration in the subsurface water. In general, the data-model comparison for total ligand concentrations shows that our simple ligand parameterization starts reproducing some features of the large-scale ligand pattern in the ocean but also reveals its significant biases and limitations. It is important to note that this parameterization is fundamentally limited by the availability of observational data to calibrate the coefficients, and the ligand parameters and formulations may need to be updated as more data becomes available. Moreover, this parameterization encapsulates our current mechanistic understanding of how different ligand classes are produced in the ocean, which is also uncertain and can change in the future.

With these limitations in mind, I show the mean vertical profile of three modeled ligand classes in Figure 2.3 to illustrate how these three ligands are simulated in the model. L_1 is confined to the upper 200m with a concentration of $<$ 0.5 nM. L_2 is produced in the subsurface water by the remineralization of organic particles with a maximum concentration of $\sim$ 1.3nM at around 1500m. The concentration of L_3 is 1.38 nM at all depth levels. The mean contribution of each ligand class to the total ligand concentration at each depth level is shown in Figure 2.4a in percentage. L_1 accounts for $\sim$ 20% of the total ligand concentration at the surface, then disappears below 400m (dark shading). L_2 contributes $> \sim$ 40% of the total ligand concentration in the subsurface water (red shading), whereas the L_3 percentage varies from 80% at the surface to 50% in the deep ocean (green shading). The effect of Fe-binding ligands on the ocean dFe species is demonstrated in Figure 2.4b as the

mean vertical profile of different dFe species (dFe free, FeL_1 , FeL_2, FeL_3, and FeL_3) in percentage of the total dFe. The free dFe (blue shading) only accounts for $< 5\%$ of the total dFe speciation in the upper 200m water and disappears in the subsurface water and deep ocean. The existence of free dFe in the upper 200m water is due to a significant amount of dFe inputs from dust deposition and shelf sediments. Although L_1 concentration is relatively low in the surface water ($\sim$ 0.3 nM), FeL_1 (black shading) still accounts for $\sim 50\%$ of the Fe speciation at this depth level because of the strong binding strength of this ligand class. FeL_1 percentage declines significantly below $\sim$ 300m due to the disappearance of L_1 in the subsurface. The contribution of FeL_3 to the total dFe speciation (green shading) is nearly 40% at the surface then declines to $\sim 15\%$ in the subsurface. The percentage of FeL_2 species (red shading) is nearly 0% at the surface, starts increasing significantly below 200m, gets peak ($\sim 80\%$) at $\sim$ 600m and stays relatively constant below that level. It is clear that FeL_2 is the most dominant dFe species in the subsurface water in our model due to the high concentration of L_2 there ($\sim$ 1 nM) and its relative strong binding strength (K_{L2} = 10^{11} L/mol). In the upper 200m, FeL_1 and FeL_3 contribute roughly equally to the total dFe species due to the compensation in their distribution (Figure 2.3) and binding strength. L_1 has a strong binding strength but is confined to the surface with a relatively low concentration, whereas L_3 concentration stays high throughout the water column but its binding strength is weak.

2.4.1 The binding of multiple ligand classes with free dFe

I consider N classes of co-existing ligands in seawater with varying binding strength to dFe. The binding strength for each ligand class is expressed by the conditional stability constant, K_n:

$$K_n = \frac{[FeL_n]}{[Fe'][L'_n]} \tag{2.4}$$

where $[L'_n]$, $[FeL_n]$ are the concentrations of the free (unbound) and complexed forms of the n^{th} ligand respectively, and [Fe'] is the concentration of the free (unbound) inorganic dFe. Accordingly, the local concentration of the n^{th} ligand can be written as the sum of free $[L'_n]$ and complex forms $[FeL_n]$.

$$[L_n] = [L'_n] + [FeL_n] \tag{2.5}$$

Similarly, the local dFe concentration can be written as follows:

$$[Fe_T] = [Fe'] + \Sigma[FeL_n] \tag{2.6}$$

Combining three equations (2.4 - 2.6), we can eliminate $[FeL_n]$ and $[L'_n]$ to arrive at a N+1 order polynomial of [Fe'] for a given set of K_n, L_n, and $[Fe_T]$, which can be solved using the Newton-Raphson method.

$$f([Fe'], K_n, L_n, [Fe_T]) = 0 \tag{2.7}$$

While this framework allows for an arbitrary number of ligand classes, I use three classes of ligands throughout this study. Additional ligand classes can be easily included if needed.

2.5 Scavenging

The free dFe (Fe') that is not bound to ligands is subject to scavenging losses by three mechanisms. First, Fe' can be scavenged onto particulate organic matter based on a first-order bulk scavenging rate following Parekh et al., (2005) and Galbraith et al., (2010). This scavenging process is parameterized as a function of the concentration of the particulate organic matter and the Fe' concentration,

$$Fe^{org}_{scav} = k_{org} C_p^{0.58} [Fe'] \tag{2.8}$$

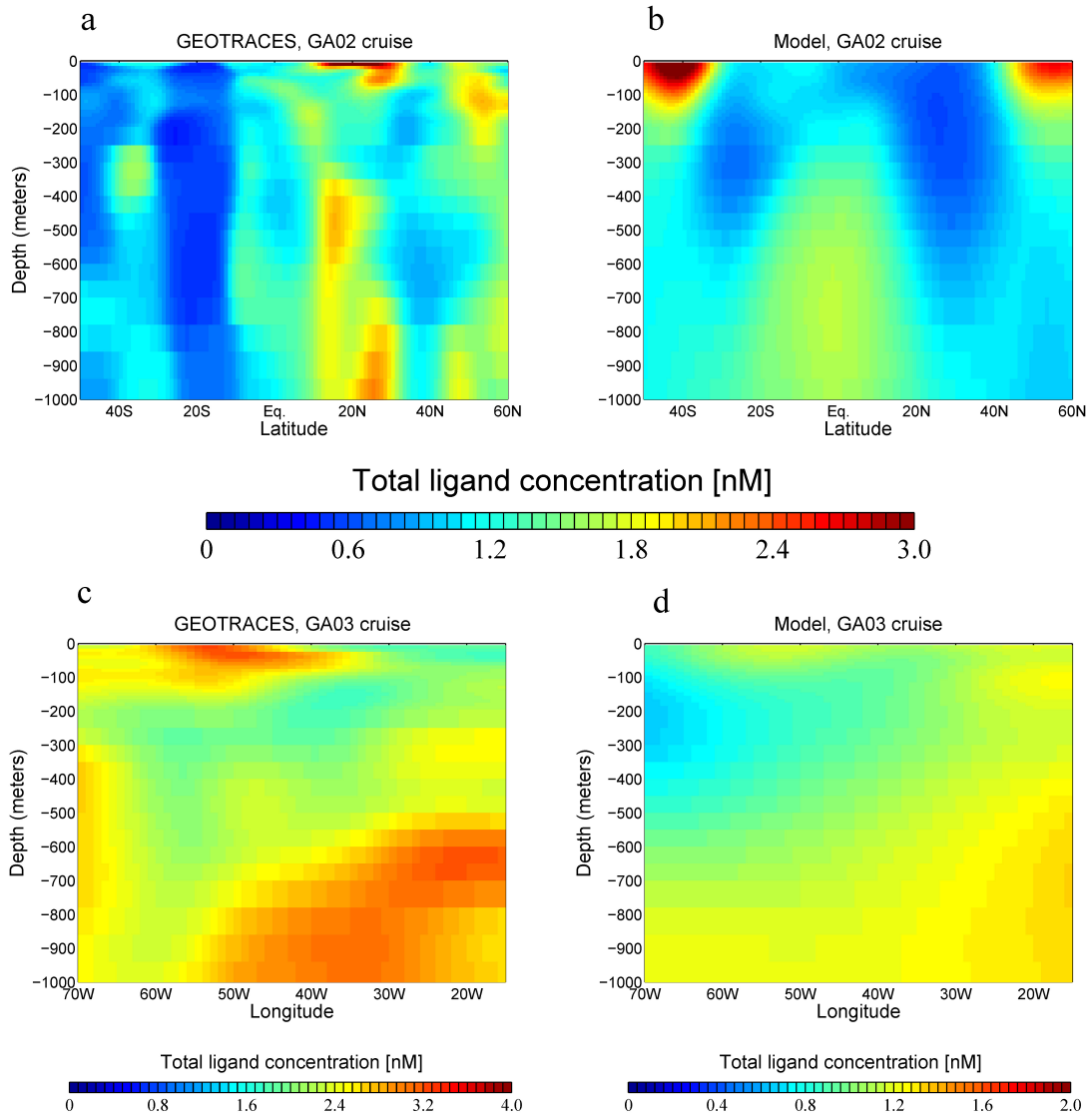

Figure 2.2: The total ligand concentration in the western Atlantic GA02 (upper panels) and subtropical North Atlantic GA03 transects (lower panels) measured by observations (left panels) and simulated in the model (right panels). Model output (annual mean) is objectively mapped onto the cruise track.

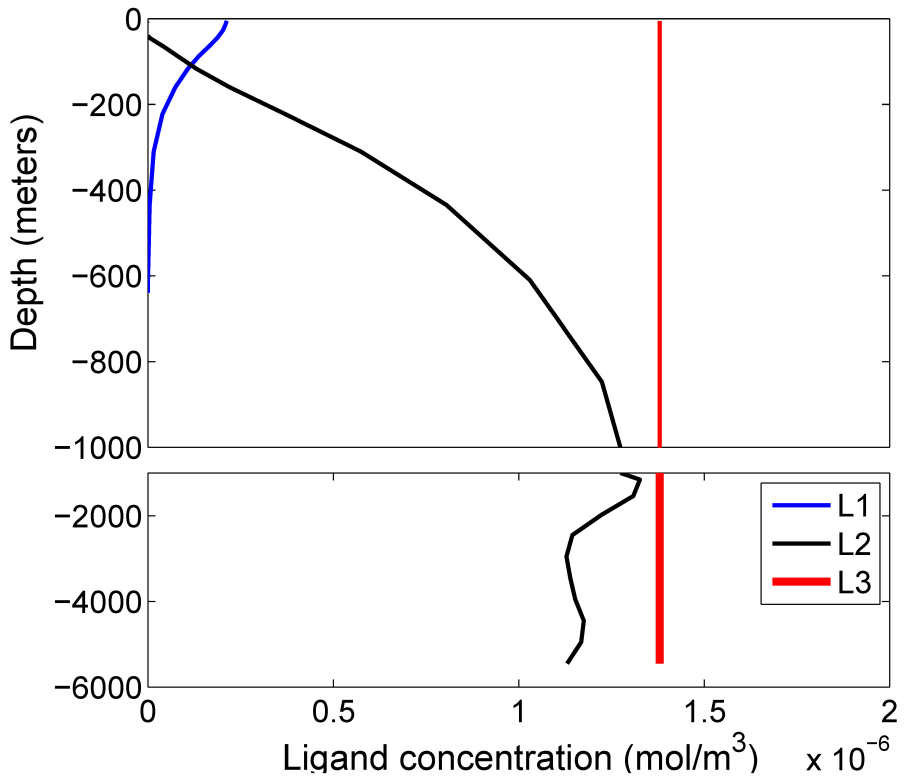

Figure 2.3: The mean vertical profile of three modeled ligand classes in the ocean. The upper 1000m water level is expanded.

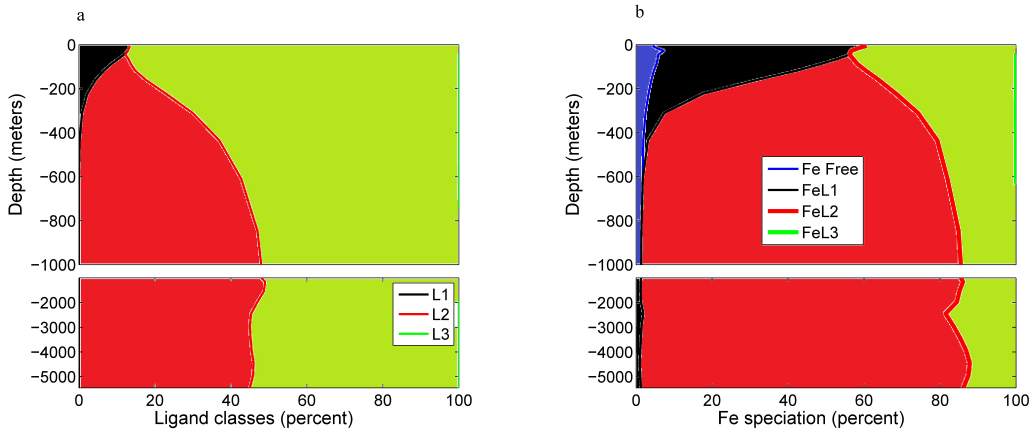

Figure 2.4: The mean ocean vertical profile in percent of different ligand classes (a) and dFe species (b) in the model. The upper 1000m water level is expanded.

where k_{org} is the rate constant and C_p is the particulate organic matter concentration. In this model, the concentration of particulate organic matter is not a prognostic variable and its vertical attenuation with depth is crudely parameterized as a power function modified from Martin et al., (1987). C_p is diagnosed from the sinking particle flux and its assumed sinking speed. The exponent of 0.58 follows the empirical study of Honeyman et al., (1988). Fe scavenged through this mechanism can be released back to the water column through the dissolution/remineralization of sinking organic particles (Boyd et al., 2010). The model calculates dFe released from organic particles in two components: cellular Fe and scavenged Fe. Remineralization of cellular Fe is determined by the Martin curve and the Fe:P uptake ratio. Because of scavenging and dissolution processes, the stoichiometric Fe:P ratio (R_{FeP}) of organic particles can change along the sinking pathway. The model explicitly calculates the vertically variable R_{FeP} by integrating the particulate Fe mass balance, and determines the vertical profile of Fe release from organic particles. A detailed description of this parameterization is provided in the subsection 2.5.1 below.

Second, Fe' can be scavenged onto inorganic particles, which are not produced by biological processes and may have lithogenic origin (Boyd et al., 2010; Galbraith et al., 2010; Tagliabue et al., 2014b). As in Galbraith et al., (2010), inorganic scavenging is parameterized as a first order loss process with a rate coefficient, k_{inorg},

$$Fe^{inorg}_{scav} = k_{inorg}[Fe']. \tag{2.9}$$

Elevated dust deposition enhances the inorganic scavenging process because of the increase in lithogenic particle concentration under high dust deposition (Ye and Völker, 2017). Therefore, I scale the rate constant by the dFe flux from atmospheric deposition as follows:

$$k_{inorg} = k_{inorg0}\left(\frac{JFe_{dust}}{\langle JFe_{dust}\rangle}\right) \tag{2.10}$$

where JFe_{dust} is the atmospheric dFe dust flux at each model grid cell in the surface ocean,

and $\langle JFe_{dust} \rangle$ is the global mean dust Fe flux. Thus, k_{inorg} can vary spatially in the surface water as a function of the atmospheric dFe flux, but its value below the surface is still set to k_{inorg0}. In addition, the minimum value for k_{inorg} is also set as k_{inorg0}, keeping it from being extremely low under the regions of low dust deposition such as the Southern Ocean. The scavenged Fe through this mechanism can also return to the water column by desorption from sinking particles. This return dFe flux is calculated in the model from the vertical profile of sinking inorganic scavenged-Fe flux, which is represented by a power function with a coefficient of -0.4.

Finally, another scavenging loss process represents the precipitation of Fe' (Fitzsimmons et al., 2015; Honeyman and Santschi, 1989). The solubility of Fe' is very low in the oxygenated seawater (Liu and Millero, 2002); therefore, the model removes the excess concentration of Fe' that is beyond the Fe solubility, [Fe'$_{max}$], set to 0.3nM. I acknowledge the crude parameterization of this type of Fe' loss, but it occurs only in a small fraction of the model domain with an intense Fe deposition. In addition, another potential loss mechanism for dFe by the coagulation of colloidal Fe (defined by the filter size usually between 0.02 - 0.2μm), which termed colloidal pumping (Honeyman and Santschi, 1989; Tagliabue et al., 2016), is not yet represented in our model.

2.5.1 An implicit scheme calculating the Fe:P ratio in particulate organic matter

In the interior ocean, although dFe can be released from sinking organic particles through remineralization, it can be re-attached to those particles by scavenging (Boyd et al., 2017). The balance between these remineralization and scavenging processes controls the Fe content of sinking particles. These processes decouple the Fe and P content of the particulate organic matter. Since particulate Fe and P are not the prognostic variables in our model, they have to be implicitly calculated. In the water column, the vertical convergence of particulate P flux gives the remineralization rate of P.

$$\frac{\delta f_p}{\delta z} = Remin_P \tag{2.11}$$

The vertical convergence of particulate Fe flux is equal to the difference between the remineralization rate of Fe and the scavenging of free Fe onto the particulate organic matter.

$$\frac{\delta f_{Fe}}{\delta z} = Remin_{Fe} - k_{org} Fe' \tag{2.12}$$

where $Remin_P$ and $Remin_{Fe}$ are the remineralization rates of P and Fe. The sinking fluxes and remineralization rates for Fe and P are linked through the stoichiometric ratio R_{FeP} that can change along the sinking pathway.

$$f_{Fe} = f_P R_{FeP} \tag{2.13}$$

$$Remin_{Fe} = Remin_P R_{FeP} \tag{2.14}$$

Combining (2.12) and (2.13), we get:

$$R_{FeP}\frac{\delta f_P}{\delta z} + f_P \frac{\delta R_{FeP}}{\delta z} = Remin_{Fe} - k_{org} Fe' \tag{2.15}$$

Plugging (2.11) and (2.14) into (2.15), we can simplify (2.15) to:

$$f_P \frac{\delta R_{FeP}}{\delta z} = -k_{org} Fe' \tag{2.16}$$

Integrating equation (2.16) vertically from the base of euphotic layer downward, we can calculate the vertical profile of R_{FeP} of the particulate organic matter.

$$R_{FeP(z)} = R_{FeP(eu)} + \int_z^{eu} \frac{k_{sc} Fe'}{f_P} dz \tag{2.17}$$

where $R_{FeP(eu)}$ is set to the Fe:P uptake ratio in the euphotic layer. The vertical integral of

Table 2.1: Model parameters

α(unitless)	6.1 $\times 10^{-5}$
β(unitless)	1.3 $\times 10^{-5}$
γ(unitless)	0.5
$L_{refract}$(mol/m^3)	2.76 $\times 10^{-6}$
K_1 (L/mol)	10^{12}
K_2 (L/mol)	10^{11}
Total L (mol/m^3)	variable
k_{org} (m^3g$C^{-1}s^{-1}$)	1.16 $\times 10^{-5}$
k_{inorg} (s^{-1})	2.0 $\times 10^{-7}$
R_{FeP} (unitless)	variable
Global Sed.dFe flux(mol/s)	11938
$dFe/^3$He	variable

scavenging rate normalized by the sinking P flux determines the excess Fe contained in the particulate organic matter. In high Fe and low-productivity regions (such as the subtropical North Atlantic), the integral in equation (2.17) can sometimes lead to numerical instability. In order to avoid large computational errors, I set a maximum value of 0.01 for R_{FeP}. This condition only occurs in a small number of model grid points and the specific choice of the maximum value does not significantly alter the model solution.

CHAPTER 3

FORMATION AND MAINTENANCE OF THE GEOTRACES SUBSURFACE DISSOLVED IRON MAXIMA IN AN OCEAN BIOGEOCHEMISTRY MODEL

This chapter is modified from an article published in *Global Biogeochemical Cycles* as

Pham A.L.D., and T. Ito. (2018), Formation and maintenance of the GEOTRACES subsurface dissolved iron maxima in an ocean biogeochemistry model, Global Biogeochem. Cycles, 32. https://doi.org/10.1029/2017GB005852

Abstract

Recent GEOTRACES transects revealed basin-scale patterns of dFe in the global oceans, providing a unique opportunity to test numerical models and to improve our understanding of the Fe cycling. Subsurface maxima of dFe in the upper ocean thermocline are observed in various transects, which can play an important role in regulating marine productivity due to their proximity to the surface euphotic layer. An ocean biogeochemistry model with refined parameterizations of Fe cycling is used to examine the mechanisms controlling the formation and maintenance of these subsurface maxima. The model includes the representation of three dFe sources including dust deposition, continental shelves, and hydrothermal vents. Three classes of organic ligands are parameterized as functions of DOC and AOU. Parameterizations of particle-dependent scavenging and desorption are included. Although the model still struggles in fully capturing the observed dFe distribution, it starts reproducing some major features, especially in the main thermocline. A suite of numerical sensitivity experiments suggests that the release of scavenged Fe associated with sinking organic particles forms the subsurface dFe maxima in high-dust regions of the Indian and Atlantic Oceans. In low-dust regions of the Pacific basin, the subsurface dFe extrema are sustained by inputs from the continental shelves or hydrothermal vents. In all cases, subsurface ligands produced by the remineralization of organic particles retain the dFe and

play a central role in the maintenance of the subsurface maxima in our model. Thus, the parameterization of subsurface ligands has a far-reaching impact on the representation of global Fe cycling and biological productivity in ocean biogeochemistry models.

3.1 Introduction

The micronutrient Fe limits the biological productivity of about half of the world's oceans including the subpolar Pacific, the equatorial Pacific, and the Southern Ocean, thereby influencing the marine ecosystems and global carbon cycle (Boyd and Ellwood, 2010; Moore et al., 2013). For this reason, processes driving the ocean Fe cycling have been studied intensely over past decades. Oceanic Fe cycling is distinct from those of other nutrients because of the extremely low concentration of dFe and the involvement of diverse and complex array of processes. In the oxygenated seawater, Fe mostly exists as ferric (Fe(III)) species with the solubility at a subnanomolar level (Liu and Millero, 2002) and thus rapidly precipitates to form colloidal Fe oxides (Wu et al., 2001). The very low concentration of dFe has made it difficult to accurately determine its global distribution. At the same time, the diverse source and sink processes and their interactions pose a significant modeling challenge. Ocean biogeochemistry models integrate these mechanisms and their interactions in the context of the global ocean circulation and have indeed provided important insights, but the models still show significant biases (Tagliabue et al., 2016; Tagliabue et al., 2017). The existence of significant model biases indicates problems in the current parameterizations of Fe cycling and the quantification of Fe sources and sinks.

There are several sources of dFe to the ocean including atmospheric deposition (Duce and Tindale, 1991; Jickells et al., 2005), continental shelves (Elrod et al., 2004; Johnson et al., 1999), and hydrothermal vents (Fitzsimmons et al., 2014; Resing et al., 2015; Tagliabue et al., 2010). There are also multiple processes removing Fe from the seawater such as biological uptake (Sunda, 2012), precipitation, and scavenging onto organic and inorganic particles (Dutay et al., 2015; Jackson and Burd, 2015). Furthermore, Fe can take many

different forms in the water column. As stated earlier, ferric (Fe(III)) species, the primarily form of Fe in the seawater, has the solubility at a sub-nanomolar level and thus quickly precipitates. Fe can also be bound to marine particles either through biological incorporation or scavenging process (Revels et al., 2015). The particle-bound Fe, referred to as particulate Fe, can aggregate and gravitationally sink through the water column (Fowler and Knauer, 1986; Jeandel et al., 2015). Some of the sinking particulate Fe can return to dissolved form through desorption and particle remineralization (Boyd et al., 2000). Remineralized Fe can be scavenged again or be transported back to the surface via upwelling and vertical mixing (Tagliabue et al., 2014a). However, dFe can be protected from scavenging and precipitation by forming complexes with organic ligands (Berg, 1995; Macrellis et al., 2001). The crucial role of organic ligands in protecting dFe was first demonstrated in the 1990s by Rue and Bruland, (1995), Berg, (1995) and Wu and Luther, (1995), who showed that the majority of dFe in seawater ($\sim$ 99%) is bound to ligands. Recent observational and experimental studies further confirmed the vital role of ligands by showing that marine bacteria produces ligands to facilitate the retention and biological uptake of dFe (Buck et al., 2010; Hutchins et al., 1999; Kustka et al., 2015; Witter et al., 2000).

There is an emerging opportunity to improve our understanding of these processes as quality-controlled Fe dataset is rapidly expanding along the GEOTRACES transects (Mawji et al., 2015). These transects confirmed the existence of subsurface dFe extrema as a prominent feature in many parts of the oceans, which was observed by Johnson et al., (1997) through various vertical dFe profiles in the Pacific, North Atlantic, and Southern Oceans. A common pattern of dFe maxima has been shown by GEOTRACES cruises in the main thermocline (300 - 1,000m) as well as in the deep waters (>2,000m) of various ocean basins. The thermocline dFe maxima are likely formed by the release of dFe from remineralization processes (Nishioka et al., 2013; Noble et al., 2012; Rijkenberg et al., 2014) and/or by external dFe sources (Nishioka and Obata, 2017; Resing et al., 2015). The deep (>2,000m) dFe maxima are likely associated with hydrothermal sources (Nishioka

et al., 2013; Resing et al., 2015). This study will focus on the mid-depth dFe maxima embedded in the main thermocline due to their proximity to the surface euphotic layer with a potential to influence biological productivity. The upwelling of thermocline waters can be an important source of dFe to marine phytoplankton, especially Fe-limited upwelling regions (Tagliabue et al., 2014a).

The objective of this chapter is twofold. First, I aim to test the ability of an ocean biogeochemistry model to reproduce the subsurface dFe maxima observed in the new GEOTRACES transects. The model includes a number of refinements in the Fe cycle parameterizations including three classes of spatially varying organic ligands, scavenging onto and desorption from organic and inorganic particles, and inputs from external sources. Second, I aim to better understand the mechanisms supporting the formation and maintenance of the subsurface dFe maxima through a suite of sensitivity experiments. I purposefully turn off the Fe cycling parameterizations one at a time. The importance of a specific mechanism is inferred from the disruption in the dFe distribution caused by its removal from the model, indicating its contribution to the model's ability to reproduce the observed dFe distribution.

I specifically examine parameterizations controlling the transformation of Fe between dissolved and particulate pool via scavenging, desorption and remineralization mediated by the presence of organic ligands. Organic ligands bind dFe and prevent it from being scavenged onto marine particles, thus playing central roles in the retention of Fe in the dissolved pool (Hutchins and Boyd, 2016). The sources, sinks, and molecular compositions of organic ligands are not yet fully understood (Hassler et al., 2017) and the parameterizations of organic ligands in ocean biogeochemistry models still have significant uncertainty. Although a variety of ligands exists in the oceans (Hunter and Boyd, 2007), existing measurements often define three discrete ligand classes based on their distribution and binding strength with dFe estimated by measuring the conditional stability constant K_n. They are: a strong, surface ligand (L_1), a weak, subsurface ligand (L_2), and a weak, refractory-DOC component ligand (L_3) (Hassler et al., 2017). Several approaches have been taken to rep-

resent ligands in ocean biogeochemistry models. Earlier generations of models assumed a spatially homogeneous single ligand by either limiting the scavenging at a constant threshold (Archer and Johnson, 2000) or explicitly resolving the local partitioning of free and ligand-bound Fe (Parekh et al., 2005). Subsequent development included the spatially variable ligand distribution, often by linking it to the pattern of DOC and/or AOU (Misumi et al., 2013; Tagliabue and Völker, 2011). The uncertainties in the representation of ligands can lead to biases in the model dFe distribution (Tagliabue et al., 2016). However, observational techniques to identify Fe-ligand complex are being improved (Boiteau and Repeta, 2015) and the data coverage for organic ligands has expanded in recent years (Buck et al., 2015; Gerringa et al., 2015), providing an opportunity to improve ligand parameterizations. A recent modeling study by Völker and Tagliabue, (2015) explicitly simulated a single ligand as a prognostic variable by representing its sources and sinks. Although it requires specifications of the ligand sources and sinks that are still uncertain, the inclusion of a prognostic ligand clearly improved the subsurface dFe distribution in ocean biogeochemistry models (Tagliabue et al., 2016). This study takes a relatively simple approach where ligands are parameterized based on calibrating empirical coefficients against the available observations. The parameterization itself is not new; I aim to keep the algorithm as simple as possible while still capturing the essential mechanisms as demonstrated by earlier studies (Misumi et al., 2013; Tagliabue and Völker, 2011). This approach is simple to implement and delivers spatially resolved representation of organic ligands, and thus can be easily manipulated in the sensitivity experiments.

This chapter is organized as follows. In section 2, I describe the model configuration and set up the experimental design. In sections 3 and 4, I present results of sensitivity experiments. In section 5, I summarize and discuss the implication of these results.

3.2 Model Configuration and Experimental Design

The ocean biogeochemistry model used in this chapter is based on the MITgcm model described in chapter 2. In brief, there are three major sources of dFe into the ocean: atmospheric deposition, shelf sediments, and hydrothermal vents. Three Fe-binding ligand classes, protect dFe from being scavenged and precipitated, are considered. Of the three ligands, L_1 is considered to have a stronger binding strength (K_{L1} = 10^{12} L/mol), while L_2 and L_3 have weaker binding strengths (K_{L2} = 10^{11} L/mol and K_{L3} = 10^{10} - 10^{11} L/mol). In this chapter, I set the binding strengths (conditional stability constants) for L_2 and L_3 the same (K_{L3} = K_{L2} = 10^{11} L/mol) since both ligand classes are assumed to be DOC humics and the binding strength for humic-like ligand is not yet certain (Gledhill and Buck, 2012). Thus, only two ligand classes (L_1 and L_2) are mechanistically represented in the model in this chapter.

3.2.1 Experimental design

The model was spun up for 1,000 years to achieve a quasi steady state with the standard set of parameters (*Full* run). At the end of the spinup, the model drifts in the global inventories of dFe (<0.01 percent/year) and the biological carbon uptake ($<$ 0.02 percent/year) are minimal. Six sensitivity experiments are initialized from the end of the spinup run with altered parameterizations and integrated for additional 1,000 years to reach new quasi steady state. The purpose of these simulations is to evaluate the relative roles of organic ligands, scavenging, remineralization processes, and external sources in regulating the ocean dFe cycling. The six experiments are designed as follows.

- "*constL*" run uses a uniform constant concentration for ligand (1 nM) with K_L=10^{11} L/mol.
- "*const*K_L" run uses the same conditional stability constant for L_1 and L_2 (set to $10^{11.5}$ L/mol).

- "*Large* ΔK_L" run uses increased difference in the conditional stability constants between L_1 (set to 10^{13} L/mol) and L_2 (set to 10^{10} L/mol).

- "*No Fe redissolution*" run suppresses the dissolution of scavenged Fe associated with organic particles.

- "*Weak sed*" run reduces the shelf Fe source by 70%.

- "*Weak hydro*" run reduces the hydrothermal Fe source by applying a uniform dFe/^{3}He ratio as in Tagliabue et al., (2010).

The first three sensitivity runs will examine different aspects of the ligand parameterization. Comparing *constL* and *Full* run will illustrate the importance of the nonuniform ligand distribution. In contrast, *constKL* and *Large* ΔK_L runs will show the importance of different binding strengths between the two types of ligand. The last three runs will examine different sources of Fe to the water column. Scavenging of Fe' onto particulate organic matter is a major removal process of dFe, but the scavenged Fe can return to dissolved form in the deeper waters when particles are remineralized. Thus, sinking organic particles can effectively transfer dFe downward in the water column. In the *No Fe re-dissolution* run, this process is suppressed in order to assess the importance of the coupled scavenging-dissolution process as a subsurface source of dFe. Other model parameters for *Full* and sensitivity runs are provided in the Supporting Information Table 3.1.

3.3 Mechanism Behind the Subsurface DFe Maxima

The annual mean of the last-year output dFe distribution of the model is compared with observations in six GEOTRACES transects: the GA02 (Figure 3.2; Rijkenberg et al., 2014), CoFeMUG (Figure 3.3; Noble et al., 2012; Saito et al., 2013), GI04 (Figure 3.4; Nishioka et al., 2013), GP02 (Figure 3.5; Nishioka and Obata, 2017), GP13 (Figure 3.6; Ellwood et al., 2018), and GP16 (Figure 3.7; Resing et al., 2015). While comparing the annual mean dFe output with GEOTRACES dFe data could lead to some mismatches due to large

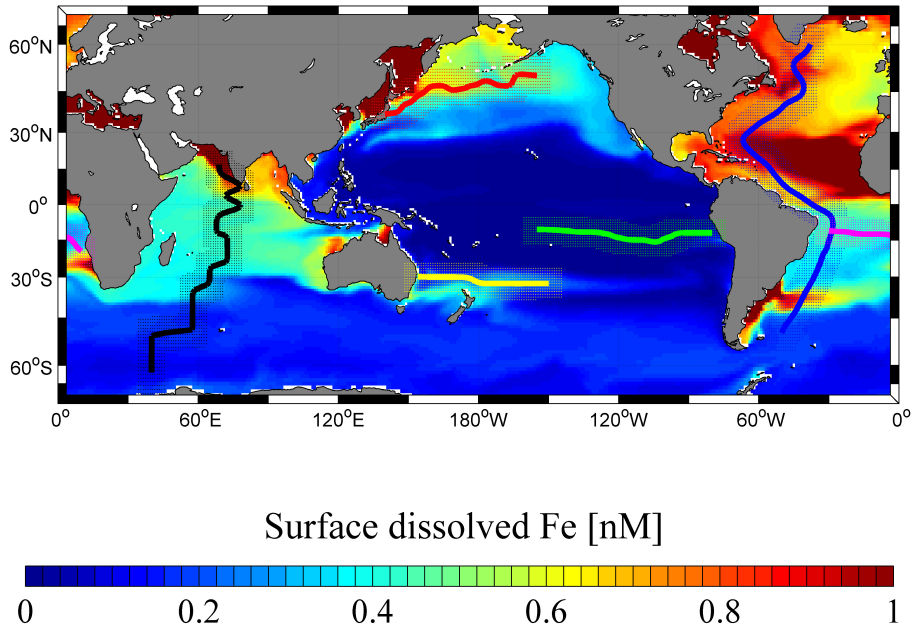

Figure 3.1: Modeled (*Full* run) surface dFe distribution (black, red, yellow, green, blue, and magenta lines indicate cruise tracks of GI04, GP02, GP13, GP16, GA02, and CoFeMUG cruises from GEOTRACES, respectively)

seasonal changes in surface observations (Sedwick et al., 2005; Wu and Boyle, 2002), these comparisons can still provide us insights into how our model performs and improve our understanding of the subsurface dFe distributions. Observational dFe data is obtained from the GEOTRACES 2017 intermediate data products (Mawji et al., 2015) and I used the objective mapping method to interpolate model and observational dFe data onto the same grid which has spatial resolution of 1°and vertical resolution of 10m near the surface to 100m at depth. More details on the model-data comparison method are provided in the Supporting Information. The surface model dFe concentration is low in the sub-polar North Pacific, the tropical Pacific, and the Southern Oceans and is high in the tropical Atlantic and Indian Oceans because of their proximity to major dust sources (Figure 3.1).

The two transects covering the Atlantic basin reveal unique features of the dFe distribution that are distinct from macronutrients (Figures 3.2 and 3.3). Specifically, dFe shows

weak signature of major water masses likely due to the distinct patterns of sources and sinks such as atmospheric deposition, continental shelves, and particle scavenging (Rijkenberg et al., 2014).

The Indian Ocean transect displays a stark contrast in the dFe distribution between the tropical and subtropical waters (Figure 3.4a; Nishioka et al., 2013). The three Pacific basin transects display typical features of the dFe distribution for high-nutrient-low-chlorophyll (HNLC) regions. The low dFe concentration is ubiquitous at the surface despite the high dFe levels in the subsurface and deep waters, which are supplied from the low-oxygen continental shelves and hydrothermal vents (Nishioka and Obata, 2017; Resing et al., 2015). All these transects show a pattern of dFe maximum at around 300 - 1000m depth, typically near the oxygen minimum layer and thus can be a signal of remineralization process (Nishioka et al., 2013; Noble et al., 2012; Rijkenberg et al., 2014). I focus on the model-data comparison for the upper 1,000m by expanding the depth from 0 - 1000m and compressing the rest of the water column in Figures 3.2-3.7. While the model shows biases in dFe distribution, some general features of the subsurface dFe maxima are reproduced, especially in the main thermocline.

3.3.1 Atlantic and Indian Oceans

The GA02 section maps the meridional dFe distribution along the western Atlantic basin (Rijkenberg et al., 2014). The surface dFe enrichment around 20°N and the strong dFe maximum around 300 - 1,000m at 10°N are both reproduced in the *Full* run of the model (Figures 3.2a and 3.2b), but our model displaces the depth of the subsurface dFe peak to a shallower depth than observed ($\sim$400m in the model versus $\sim$600m depth in the observation). Our model also underestimates the magnitude of the surface dFe at 20°N by about 0.4 nM. The model also reproduces the elevated subsurface dFe observed at 35 - 40°S, but underestimates its magnitude and somewhat displaces its location further south than observations. This feature, which is not captured by most models analyzed in Tagliabue

et al., (2016), might be explained by the dFe flux from shelves or the Rio de la Plata River (Rijkenberg et al., 2014). Another model bias is in the subsurface waters around 40°N, where our model captures the observed dFe maximum from 400 - 1000m, but its extension is up to the surface, while observed surface dFe is low. Several other models mentioned in Tagliabue et al., (2016) also have this problem and it may indicate bias in the scavenging scheme. Our model also fails to capture features of the hydrothermal signal in the deep ocean. Specifically, the modeled hydrothermal dFe signal seems to be displaced and overestimated, especially around 2000-3000m at 20 - 30°S. Although the model exhibits some biases, I find the overall results encouraging. With the inclusion of a relatively simple, spatially varying ligand parameterization, the model starts to reproduce the observed subsurface dFe maxima at 10°N and at 35 - 40°S, which were not captured by Dutkiewicz et al., (2015) whose Fe cycling is based on the earlier version of our model.

The mechanism behind the observed subsurface maxima is explored through six additional sensitivity experiments. Figures 3.2-3.7 shows a subset of the sensitivity runs. The *constL* and *No Fe rediss.* runs respectively suppress the release of ligand and scavenged Fe associated with organic particles. The *Weak sed* and *Weak hydro* runs reduce the Fe input from continental shelves and hydrothermal vents respectively. The subsurface maximum of dFe at 10°N disappears in both *constL* and *No Fe rediss.* runs (Figures 3.2c and 3.2d), whereas it almost stays intact in *Weak sed* and *Weak hydro* runs. Similarly, the subsurface rich dFe water at 40 °N is greatly decreased in the *constL* and *No Fe rediss.* runs, but just slightly decreases in the other two experiments. On the other hand, the elevated subsurface dFe at 35 - 40°S is significantly reduced in *constL*, *Weak sed*, and *No Fe rediss* runs. The *Weak hydro* experiment shows the decrease of dFe only in the deep ocean (Figure 3.2f) where the hydrothermal dFe flux dominates. These results suggest that the remineralization sources of ligand and dFe are required to sustain the observed dFe subsurface maxima in the GA02 western Atlantic transect. In addition, the shelf Fe source might be important for the subsurface dFe concentration in the South Atlantic.

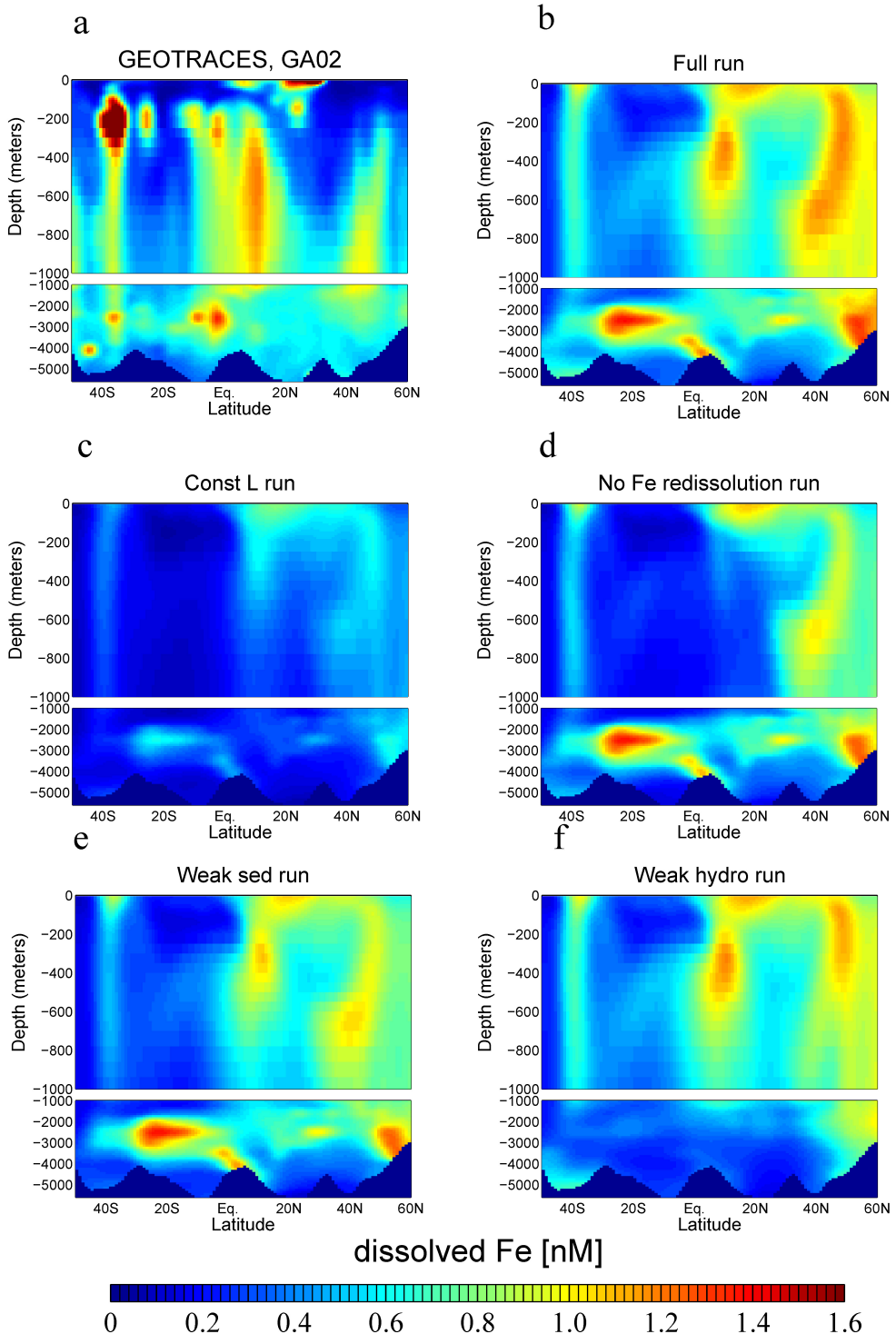

Figure 3.2: dFe distribution along the GA02 transect: (a) Observations, (b) *Full* run, (c) *ConstL* run, (d) *No Fe redissolution* run, (e) *Weak sed* run, and (f) *Weak hydro* run

The CoFeMUG section maps the horizontal dFe distribution along the subtropical South Atlantic (Noble et al., 2012; Saito et al., 2013). The subsurface dFe maximum around 300-800m at 8-10°E near the eastern margin is captured in the *Full* run, but its magnitude is underestimated while its westward extension is overestimated (Figures 3.3a and 3.3b). This maximum is suggested to be associated with remineralization process and/or sediment input from continental shelves (Noble et al., 2012). Our model cannot reproduce the elevated hydrothermal dFe concentration around 3000m at 15°W, and it generally underestimates the deep dFe concentration along this transect. The mechanism behind the observed subsurface dFe maximum is explored through four sensitivity experiments (Figures 3.3c-3.3f). Similar to the GA02 transect, the subsurface maximum of dFe disappears in both the *constL* (Figure 3.3c) and *No Fe redis.* (Figure 3.3d) runs. In the *Weak sed* run, this feature is reduced in magnitude (Figure 3.3e). In the *Weak hydro* run, only the hydrothermal Fe signal in the western part of the transect at 3000m is reduced (Figure 3.3f). These results suggest that the observed subsurface dFe maximum in the CoFeMUG subtropical South Atlantic transect is formed mostly by the simultaneous release of ligand and dFe from organic particles, with the sedimentary Fe flux acting as an additional contributing factor.

The GI04 section maps the meridional dFe distribution in the Indian Ocean (Nishioka et al., 2013) (Figure 3.4). The model captures the pattern of upper ocean dFe distribution reasonably well in this region (Figures 3.4a and 3.4b). Specifically, the model captures the strong meridional gradient of dFe centered at around 10°S where the tropical thermocline exhibits the highest dFe concentration. The model also reproduces the subsurface peak of dFe in the north Arabian Sea ($\sim$ 10°N), but its amplitude and extension are overestimated. This feature could be formed by remineralization and/or adjacent reducing sediments. The model also overestimates the surface dFe concentration around 10°N, and cannot reproduce the hydrothermal signal around the Central Indian Ridge segment. The overestimation of surface dFe concentration under the high-dust region at 10°N could indicate the potential

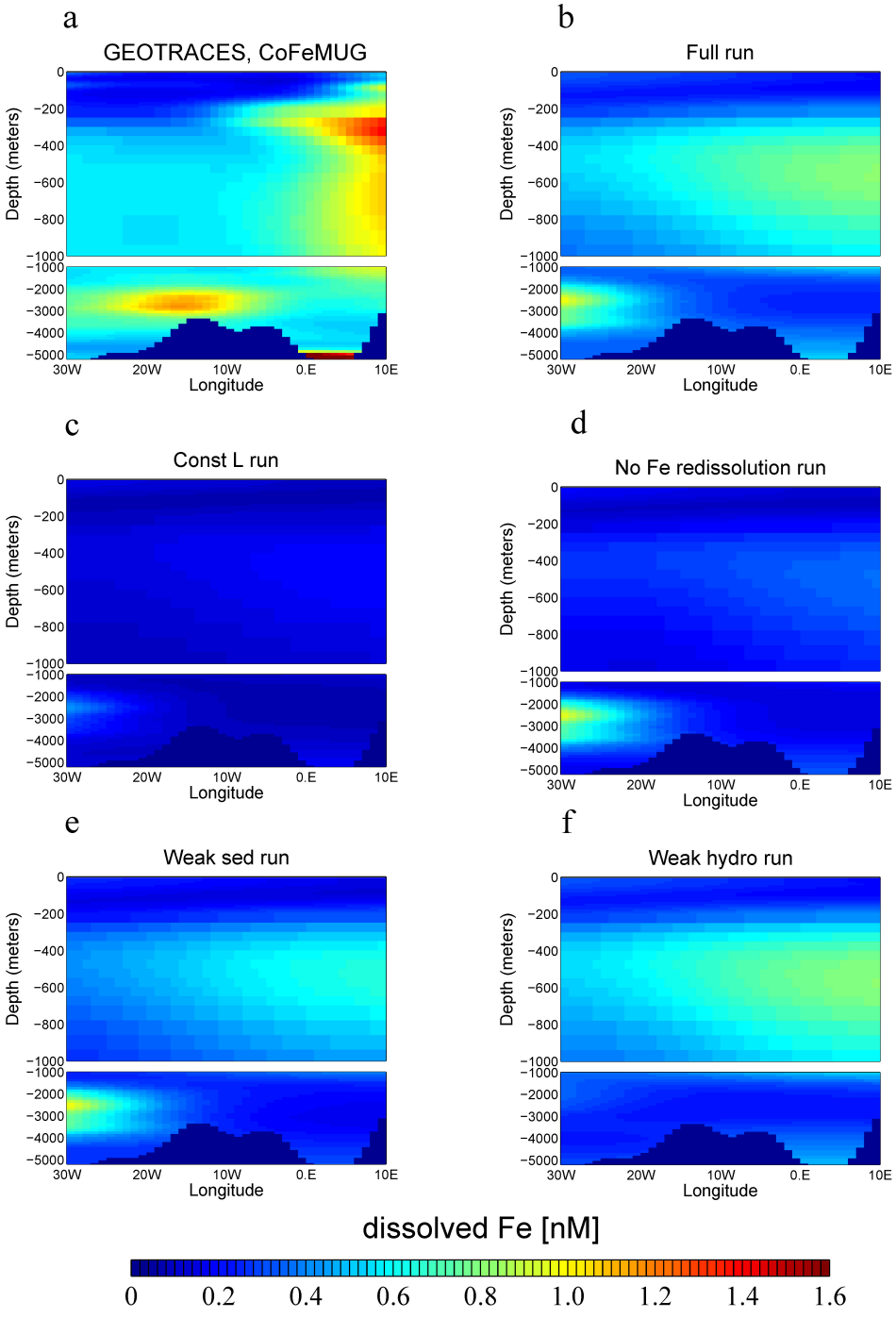

Figure 3.3: dFe distribution along the CoFeMUG transect: (a) Observations, (b) *Full* run, (c) *ConstL* run, (d) *No Fe redissolution* run, (e) *Weak sed* run, and (f) *Weak hydro* run

role of scavenging by lithogenic particles as suggested by Ye and Völker, (2017) for the tropical Atlantic Ocean. Comparing the five model runs in Figure 3.4, it is clear that the release of ligand and dFe from organic particles is important to form the dFe maximum. When the ligand is decoupled from the particle remineralization (*constL* run), the subsurface dFe maximum disappears entirely (Figure 3.4c). When the dissolution of organic scavenged Fe is suppressed (*No Fe rediss.* run), this dFe maximum is significantly reduced in magnitude and extension (Figure 3.4d). In contrast, the sedimentary Fe flux has a moderate impact only (Figure 3.4e). Also, the hydrothermal flux has little effect on the dFe distribution in this transect (Figure 3.4f).

3.3.2 Pacific Ocean

The GP02 transect maps the zonal dFe distribution in the North Pacific Ocean (Nishioka et al., 2013) (Figures 3.5a and b). In this transect, there are several model biases. Our model exhibits the high dFe concentration around 800m extending from west to east along the transect (Figures 3.5a and b), but this feature is more zonally elongated than observation. Observations indicate a strong subsurface Fe source in the western Pacific, which is underestimated in the model. The surface dFe concentration is overestimated by 0.4 nM, whereas the deep dFe concentration (at $>$ 3000m) is significantly underestimated. The widespread overestimation of surface dFe comes from the upwelling of rich-dFe subsurface waters, which receive high dFe from the continental shelves. This may imply a weak scavenging rate or biases in the factors limiting the biological uptake, potentially related to the co-limitation of productivity by macronutrient and Fe (Ingall et al., 2013).

Despite these biases, processes controlling the simulated subsurface dFe maximum at about 800m are explored through four sensitivity experiments (*Full*, *ConstL*, *No Fe redissolution*, *Weak sed*, and *Weak hydro* runs). When the non-uniform ligand is suppressed in the (*constL*) run, this dFe maximum disappears entirely (Figure 3.5c). It is also greatly decreased in magnitude when the dFe sediment flux is decreased (*Weak sed* run, Figure 3.5e).

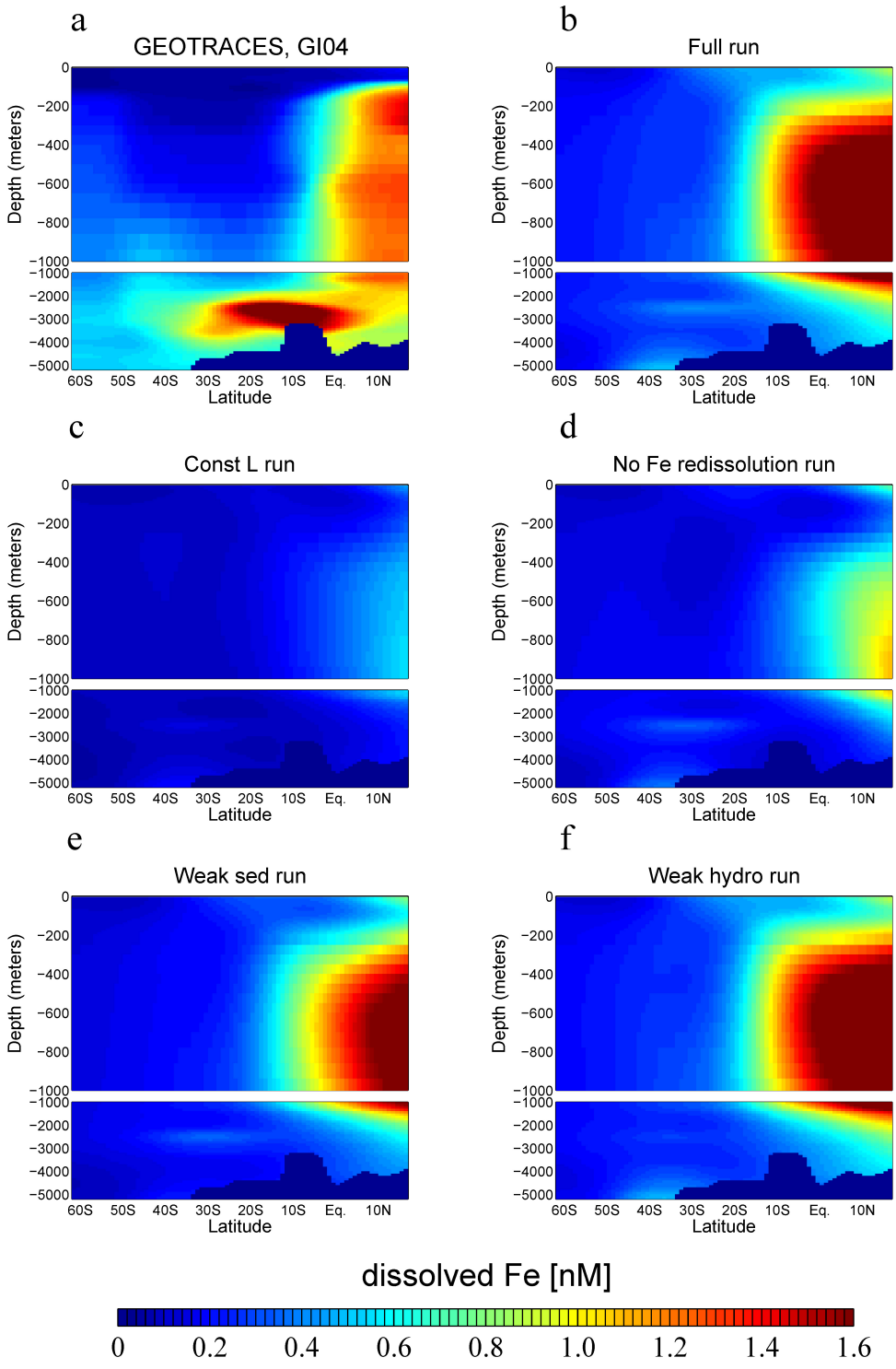

Figure 3.4: dFe distribution along the GI04 transect: (a) Observations, (b) *Full* run, (c) *ConstL* run, (d) *No Fe redissolution* run, (e) *Weak sed* run, and (f) *Weak hydro* run

On the contrary, dFe supply from the remineralization of scavenged Fe and hydrothermal vents seems to play only a small part (Figures 3.5d and 3.5f). This result is consistent with results of a recent observational study (Nishioka and Obata, 2017), suggesting that the high dFe concentration at mid-depth may come from a sedimentary Fe source. The model bias at this depth range could come from biases in the sedimentary Fe flux parameterization, which includes significant uncertainty.

The GP13 maps the zonal dFe distribution in the south western Pacific Ocean. The model reproduces several features of the dFe distribution in this region (Figures 3.6a and 3.6b). In particular, the model captures the elevated dFe concentration around 600-1000m from 160-170°E. Moreover, the model reproduces low surface dFe concentration observed across the transect. The strong zonal gradient of subsurface dFe concentration $\sim$ 175°W is reproduced in the model. However, the pattern of subsurface dFe extreme is more horizontally and vertically compressed than observed.

The elevated dFe centered around $\sim$ 175°E disappears when the non-uniform pattern of ligand is suppressed (Figure 3.6c) and is greatly decreased in magnitude and extension when the dFe hydrothermal flux is reduced (Figure 3.6f). On the other hand, this feature is only slightly decreased when the release of scavenged Fe associated with organic particles or the dFe supply from continental shelves is decreased (Figures 6d and 6e). Thus, our result, along with several observational studies (Ellwood et al., 2018; Fitzsimmons et al., 2014; Resing et al., 2015), confirms the role of the long-range transport (thousands of kilometers) of hydrothermal dFe from the southern East Pacific Rise to the dFe distribution in the upper 1000m of the South Pacific Ocean. In addition, our model result suggests that this transport is facilitated by the existence of a non-uniform, remineralized ligand class, protecting dFe from scavenging along the transport pathway.

The GP16 section maps the zonal dFe distribution across the subtropical South Pacific Ocean (Resing et al., 2015) (Figures 3.7a and 3.7b). In this transect, the model captures the low dFe concentration at the surface, which is a typical feature for the HNLC region (Fig-

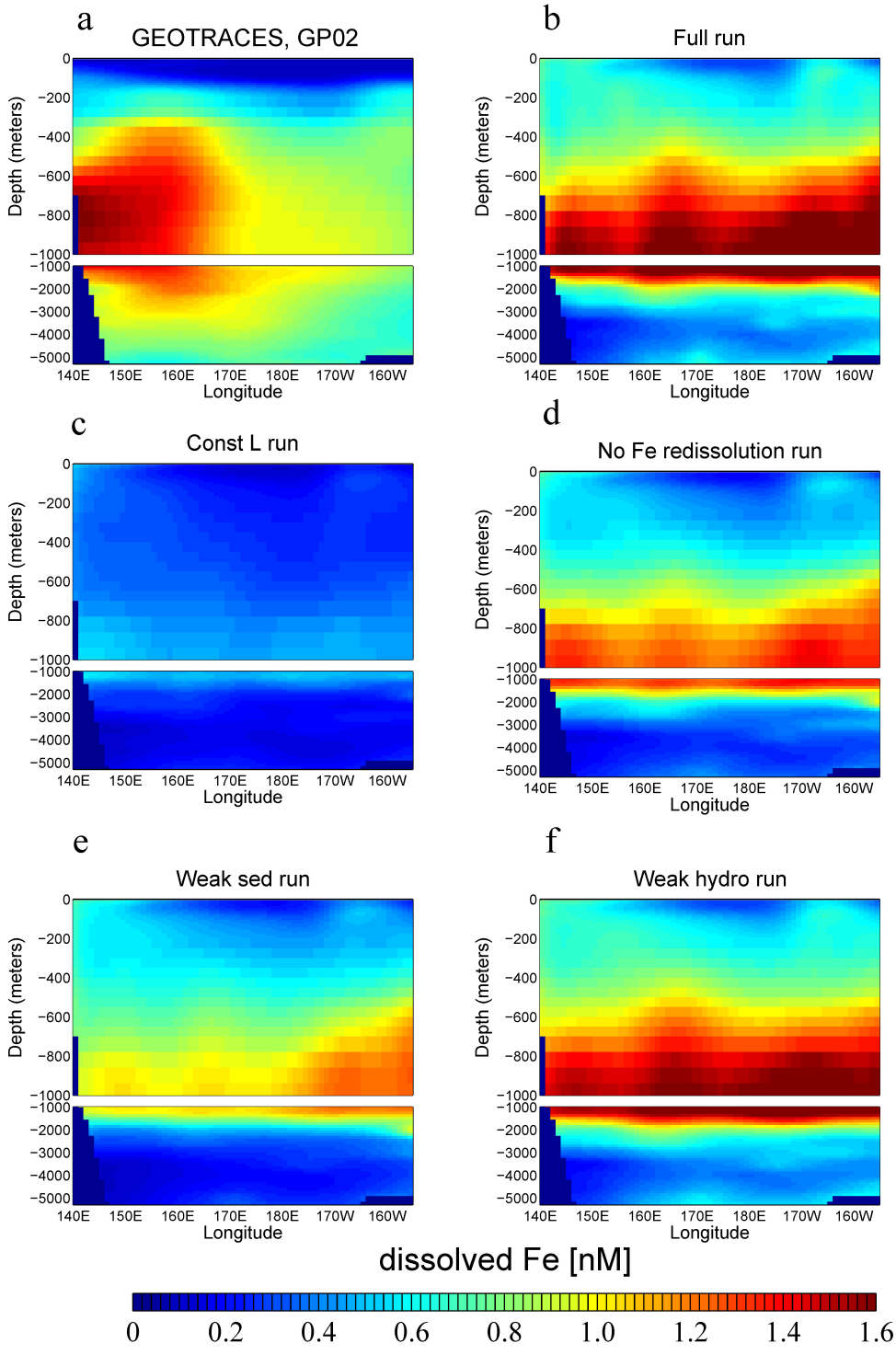

Figure 3.5: dFe distribution along the GP02 transect: (a) Observations, (b) *Full* run, (c) *ConstL* run, (d) *No Fe redissolution* run, (e) *Weak sed* run, and (f) *Weak hydro* run

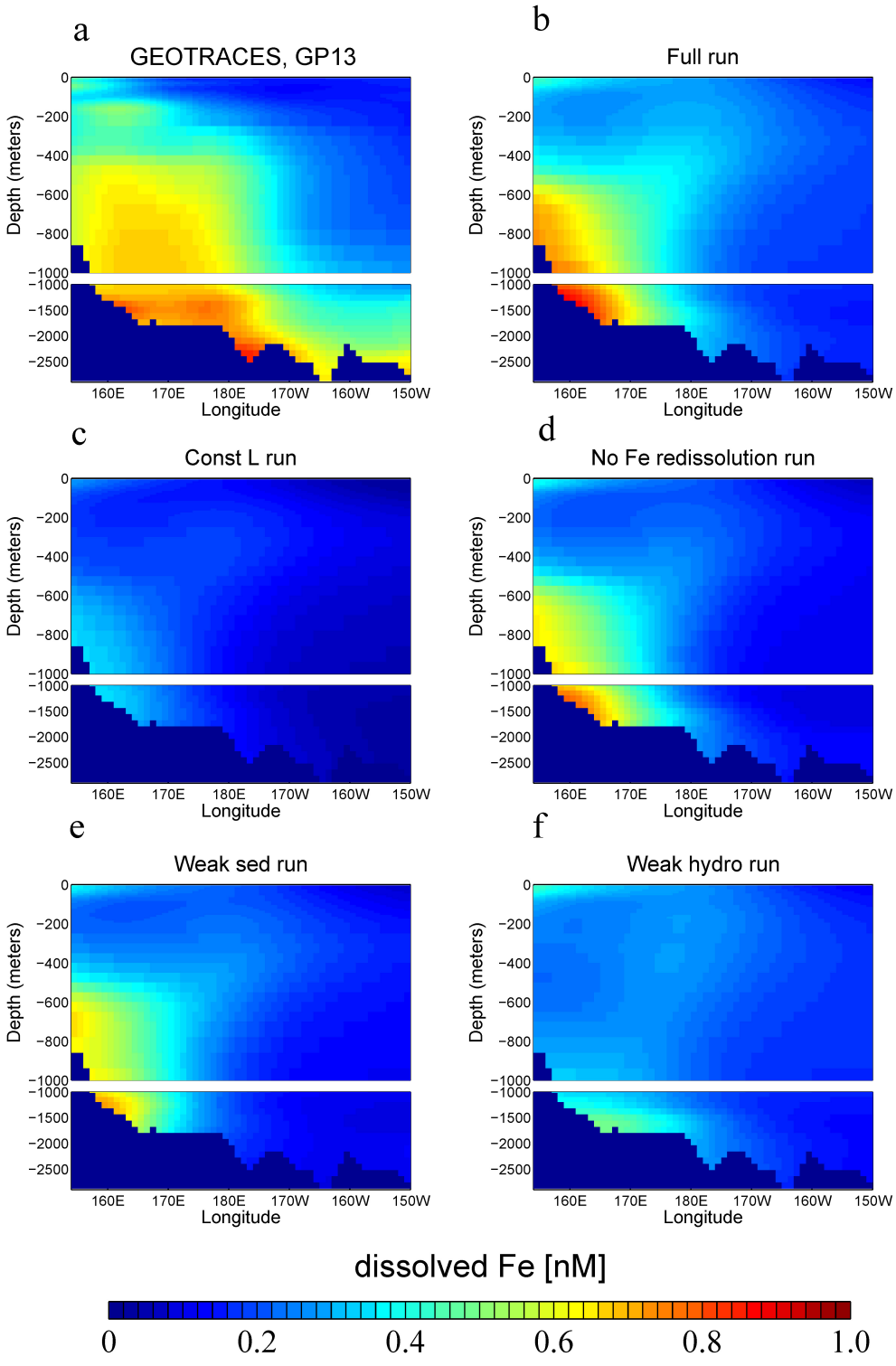

Figure 3.6: dFe distribution along the GP13 transect: (a) Observations, (b) *Full* run, (c) *ConstL* run, (d) *No Fe redissolution* run, (e) *Weak sed* run, and (f) *Weak hydro* run

ures 3.7a and 3.7b). However, the subsurface dFe maximum observed over almost the entire water column (from 200m to the bottom) in the eastern margin is greatly underestimated by the model. The model bias in this region is consistent with many other models analyzed in Tagliabue et al., (2016). Our model only shows a weak signal of this feature around 800-1000m with the concentration of 0.8 nM, about a half of the observation. This signal is disappeared in three sensitivity experiments: *ConstL*, *No Fe rediss.*, *Weak sed* (Figures 3.7c-3.7e). A recent observational study argued that this maximum could be a signal of a very persistent dFe flux from resuspended sediments (John et al., 2017). Furthermore, the observed hydrothermal signal around 3,000m at 110°W is displaced westward and greatly underestimated in our model. This hydrothermal signal is decreased in the model when a lower $dFe/^3He$ ratio from Tagliabue et al., (2010) is applied (Figure 3.7f).

Summarizing the results so far, the model-data comparison showed some strengths and weaknesses in reproducing the observed dFe distribution. The model was able to reproduce the general pattern and magnitude of the subsurface dFe maxima in many sections (GA02, CoFeMUG, GI04, GP13), but it also showed significant model biases in other sections (GP02 and GP16). Sensitivity runs showed the relative importance of different dFe sources in reproducing the observation and implied some potential causes for model biases. For deep waters, the hydrothermal vents are the most important dFe source. Thus, mismatches in the deep ocean between model and observed dFe concentration likely originate from biases in the model parameterization of hydrothermal dFe source. The mid-depth dFe in the GA02, CoFeMUG, and GI04 transects is particularly sensitive to the remineralization of scavenged Fe associated with the sinking organic particles. In contrast, the mid-depth dFe is sensitive to sedimentary dFe sources in GP02 and GP16 and to hydrothermal dFe inputs in GP13. Sensitivity experiments also revealed the important role of the non-uniform distribution of organic ligands in all of the sections. Elevated ligand concentration in the mid-depth water column plays a crucial role in the retention of dFe. Additional sensitivity experiments (*const*K_L and *Large* ΔK_L) are performed to examine the importance of

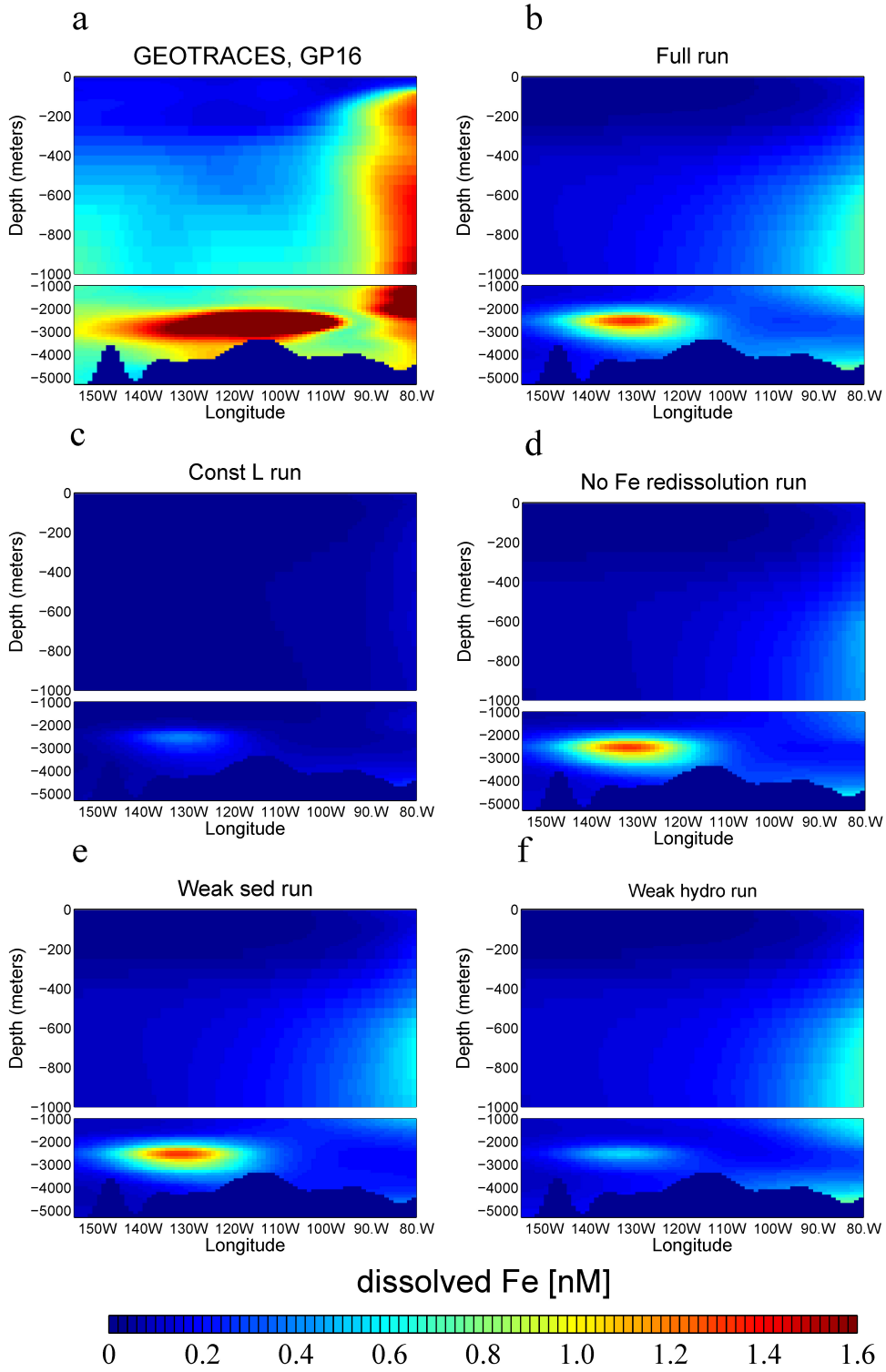

Figure 3.7: dFe distribution along the GP16 transect: (a) Observations, (b) *Full* run, (c) *ConstL* run, (d) *No Fe redissolution* run, (e) *Weak sed* run, and (f) *Weak hydro* run

different types of ligands.

3.4 The Sensitivity of dFe Distribution to the Ligand Binding Strength

Two sensitivity experiments are specifically designed to examine the role of ligands' binding strengths in controlling the dFe distribution. The *const*K_L run sets the two conditional stability constants to be at the intermediate value, $10^{11.5}$ mol^{-1}L. The *Large* ΔK_L run does the opposite, making the difference between these two values greater (10^{13}mol^{-1}L for L_1 and 10^{10}mol^{-1}L for L_2). Again the models are spun up for 1,000 years to reach a new steady state, and the results are displayed in Figures 3.8 and 3.9.

Due to the large increase in the dFe values, Figure 3.8 uses a different color bar relative to the six previous figures. Below the surface waters, the organic ligand is dominated by the L_2 ligand. In the *const*K_L run, the binding strength of the subsurface ligand L_2 is increased by a factor of 3 (from 10^{11} to $10^{11.5}$mol^{-1}L). In response, the amplitude of the subsurface dFe maxima increases by about factor of 2 in the model. This leads to an increase in the surface ocean dFe concentration even though the surface ligand class L_1 is decreased from 10^{12} to $10^{11.5}$mol^{-1}L. This increase is caused by the vertical supply of subsurface elevated dFe concentration to the surface waters via vertical mixing and upwelling (Tagliabue et al., 2014a) This result indicates the prominent role of L_2 in the retention of dFe throughout the water column, thus increasing the binding strength of L_2 caused a widespread overestimation of dFe in all of the transects.

Figure 3.9 shows the results from the *Large* ΔK_L run. In this case, the binding strength of the subsurface ligand L_2 decreases by a factor of 10 (from 10^{11} to 10^{10}mol^{-1}L), and the global dFe concentration in general decreases by a factor of 5. Figure 3.9 uses a different color bar relative to the previous figures because of the low dFe concentrations. Despite the increase in L_1 (from 10^{12} to 10^{13}mol^{-1}L), the overall dFe concentration in the water column is controlled by the binding strength of L_2. More importantly, all the observed GEOTRACES dFe maxima disappeared or are greatly reduced in magnitude in the *Large*

ΔK_L run. These results highlight the crucial role of the subsurface ligand class in maintaining mid-depth dFe maxima.

3.5 Discussion and Conclusion

The GEOTRACES program (Anderson et al., 2014; Henderson et al., 2007; Mawji et al., 2015) has significantly increased the data coverage for dFe and ligands in the global oceans, providing a unique opportunity to test ocean biogeochemistry models and improve the representation of biogeochemical processes essential for the Fe cycling (Tagliabue et al., 2016; Völker and Tagliabue, 2015). While there have been significant advances in the understanding and modeling capability of the Fe cycling in the last decade, the new observations revealed that there are many features of dFe distribution that are still missing or heavily biased in the current generation of models (Tagliabue et al., 2016). Motivated by the newly available dataset, I explored the processes driving the observed ocean dFe distribution by a suite of sensitivity experiments in an ocean biogeochemistry model with a refined parameterization for the Fe cycling. Specifically, our model includes three external dFe sources, which are modified from previous studies (Dutkiewicz et al., 2015; Moore and Braucher, 2008) to better reproduce the observations, and an improved ligand parameterization. Our ligand parameterization considers two spatially varying ligand classes, which have different binding strengths and distribution. Their distributions are parameterized as functions of DOC and AOU. The empirical constants in the ligand parameterizations are calibrated to fit the observed ligand distribution in the least square sense. While these parameterization themselves are not new and have some limitations (Gledhill and Buck, 2012; Velasquez et al., 2016), the simplicity of this approach allows us to disentangle the underlying mechanisms in a clear way.

Even though our model still has several biases when compared with observation, it starts capturing some major features such as the subsurface dFe maxima observed in various GEOTRACES transects in different ocean basins (Nishioka et al., 2013; Nishioka and

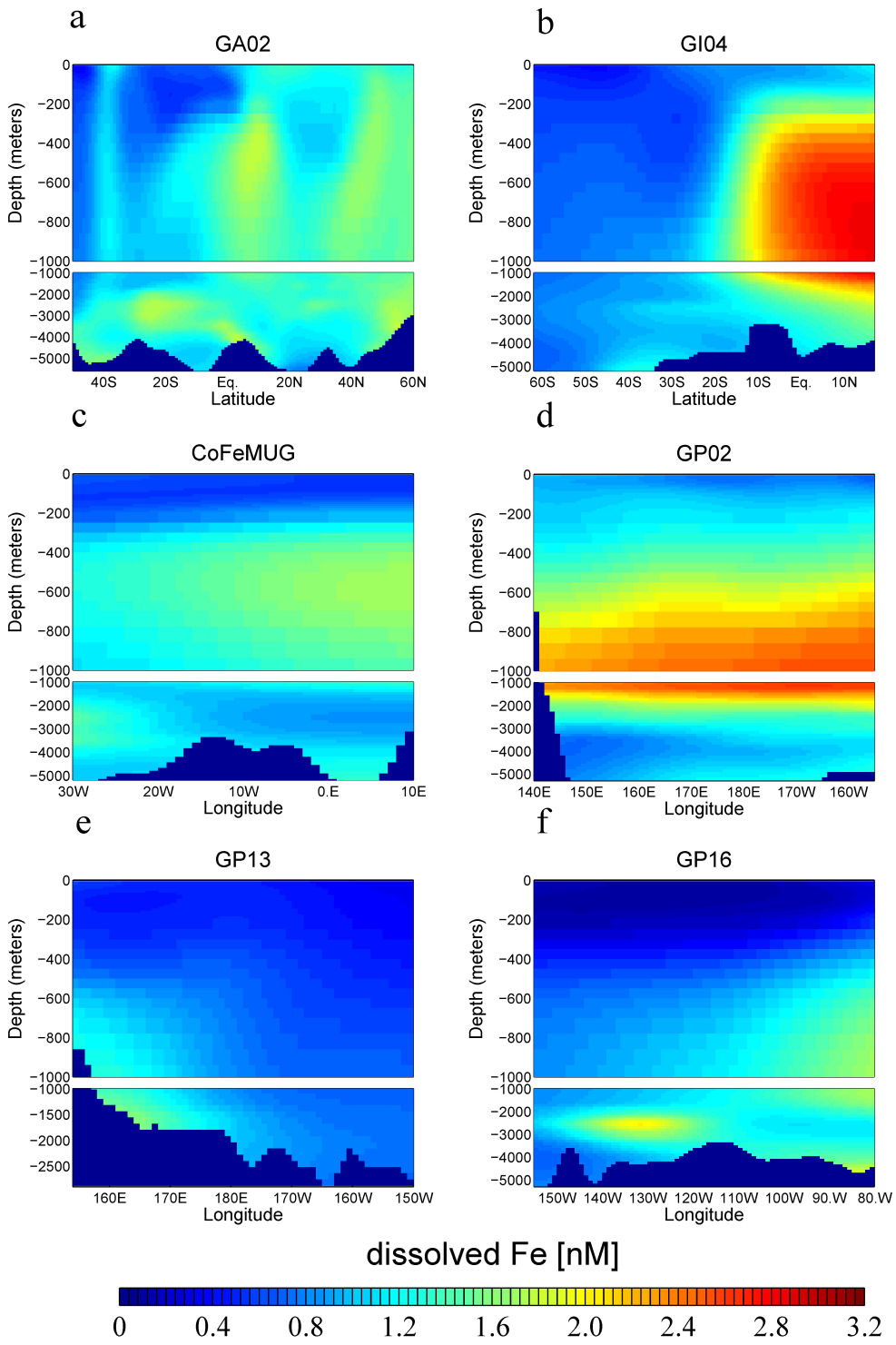

Figure 3.8: Modeled dFe distribution along the GEOTRACES transects from the *constK*$_L$ run: (a) GA02, (b) GI04 (c) CoFeMUG, (d) GP02, (e) GP13, and (f) GP16

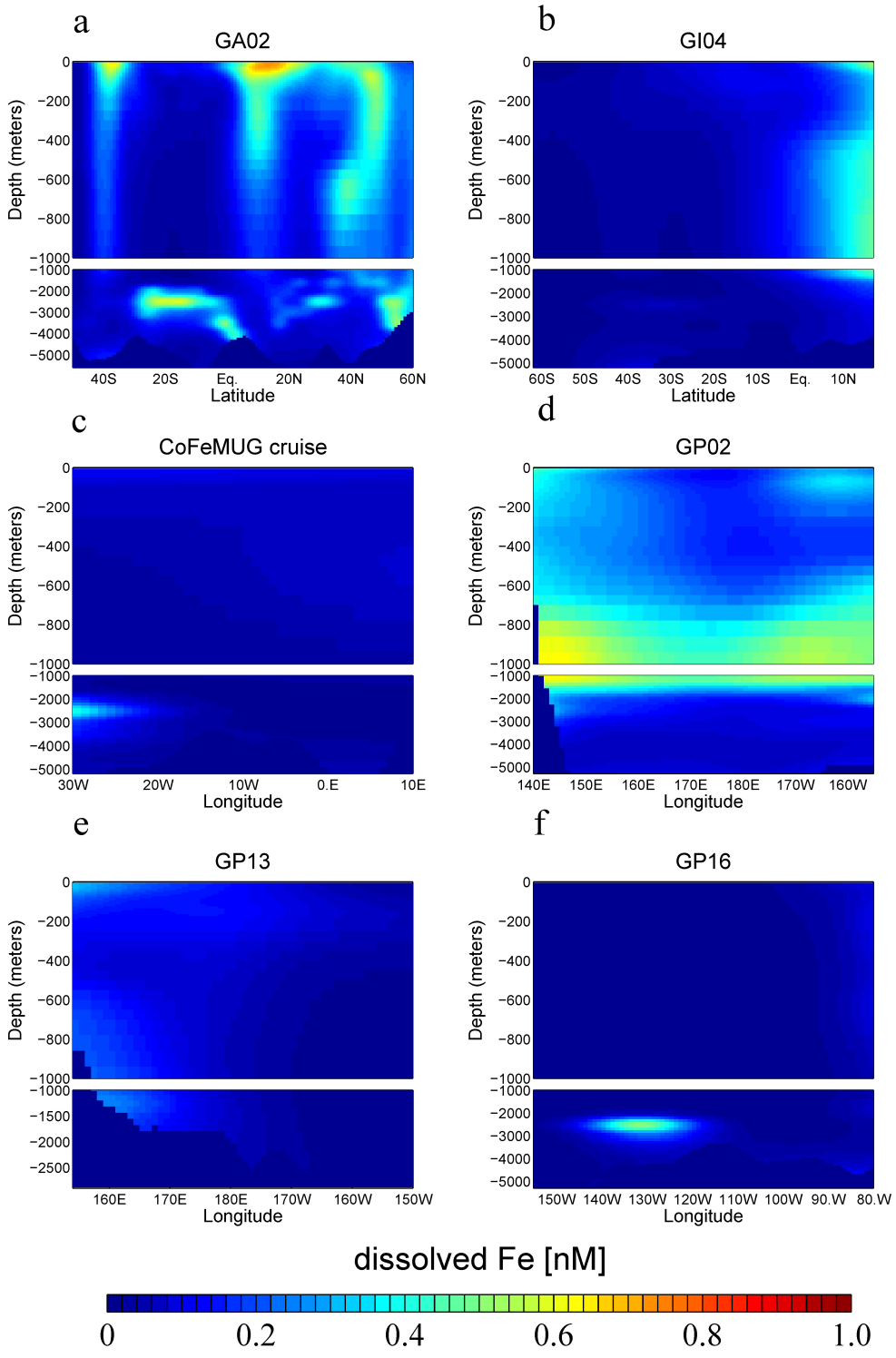

Figure 3.9: Modeled dFe distribution along the GEOTRACES transects from the *Large* ΔK_L run: (a) GA02, (b) GI04 (c) CoFeMUG, (d) GP02, (e) GP13, and (f) GP16

Obata, 2017; Noble et al., 2012; Resing et al., 2015; Rijkenberg et al., 2014), and provided an improved understanding of the mechanisms behind them. In particular, I examined the relative roles of the release of scavenged Fe back to the water column via the remineralization of sinking organic particles (Boyd et al., 2010; Velasquez et al., 2016) and of the external dFe supply from continental shelves and hydrothermal vents. Release of scavenged Fe turned out to be the crucial mechanism behind the subsurface dFe maxima in the thermocline of high-dust regions. In the surface of the tropical Atlantic and Indian Oceans, the deposited dust Fe is mostly scavenged onto organic particles, which then sink and remineralize at mid-depth level in the water column. In addition, the non-uniform distribution of weaker L_2 ligand was found to be the key factor for maintaining the subsurface dFe maxima in the model. Parameterizing the L_2 ligand using the AOU distribution was crucial to improve dFe distribution by representing the particle-remineralization as a source of the ligand. Similar results are reported in Tagliabue et al., (2016), who showed that the inclusion of the particle-remineralization source for ligands in ocean biogeochemistry models improves the reproduction of the subsurface dFe maxima. Earlier models (P05, D05) that applied a uniform constant ligand and neglected the dissolution of scavenged Fe did not reproduce the observed subsurface dFe maxima. When the release of either scavenged Fe or ligand from sinking organic particles is suppressed, the subsurface dFe maxima observed in the Indian and Atlantic Ocean transects are either disappeared or greatly reduced in magnitude in the model. Thus, in high dust regions of the Indian and Atlantic basins, the simultaneous release of ligand and scavenged Fe from organic particles not only supplies dFe to the subsurface waters but also protects dFe from being scavenged, maintaining a high level of subsurface dFe concentration. In fact, the model tends to overestimate the surface dFe in high dust regions, likely indicating bias in the representation of processes that remove dFe where dust deposition is high (Ye and Völker, 2017). This bias may reflect the missing colloidal pumping mechanism for dFe loss in our model, which could be important for high dust deposition regions (Fitzsimmons et al., 2015).

I found that Fe sources from the continental shelves and hydrothermal vents are important for subsurface dFe maxima in the thermocline of low-dust regions in the Pacific Ocean. The particle-remineralized ligand is also important in sustaining the subsurface dFe maxima in these regions, but the dFe supply from organic particles seems to be less important than from external sources. In the deep waters, the model still shows several biases including the significant underestimation of dFe hydrothermal signals. This underestimation is likely because our model does not represent the interaction between particulate and dissolved phases of Fe released from the vents, which could support the distal transport of dFe away from the vent sources (Fitzsimmons et al., 2017). Moreover, measurements by Fitzsimmons et al., (2017) show that a large portion of dFe released from hydrothermal vents can be nanoparticles of pyrite or Fe(III) oxides, which are also not represented in the model.

Figure 3.10 shows the dFe sources and sinks from all of the experiments. In terms of the external dFe sources, the hydrothermal and sedimentary dFe sources dominate the dFe input into the ocean. The largest removal mechanism is the scavenging onto inorganic particles, which is partially mediated by the release of Fe by remineralization and desorption.

When the external Fe input is reduced in *Weak sed* and *Weak hydro* runs, the removal of Fe by the inorganic scavenging is also reduced, thus balancing the input and output on the global scale. In these simulations, dFe maxima in high dust regions seem to be only slightly decreased, reflecting the dominance of atmospheric deposition and internal cycling processes in these regions.

When the dissolution of organic scavenged Fe is turned off (*No Fe rediss* run), the remineralization and desorption source of Fe is diminished in the global budget. However, the subsurface dFe maxima in the Pacific basin (GP13 and GP02) were not significantly affected in this run, reflecting the dominance of external inputs, in particular, the sedimentary and hydrothermal sources. Given the potential role of the subsurface dFe as a source for Fe-limited upwelling regions (Tagliabue et al., 2014a), these external sources can have

far-reaching effects on the marine ecosystems and the biological carbon pumps.

The sensitivity experiments with altered ligand parameterizations showed that the global dFe budget and distribution are sensitive to the strength and concentration of the subsurface ligand. When the binding strength of this ligand class increases or decreases, the global mean dFe concentration is increased or decreased. In particular, when the binding strength is reduced, almost all the mid-depth dFe maxima disappeared in the model. The impact of the siderophores-type surface ligand (L_1) seems to be negligible in controlling the subsurface dFe maxima and the global dFe budget in general. These effects are best seen by looking at the change of dFe concentration in ocean transects but are not as clear when examining the global dFe budget (Figure 3.10). These results suggest that the uncertainty in the binding strength of L_2 ligand class has a significant impact on the dFe cycling.

Finally, this study owes its existence to the hard work of the scientific community who joined the efforts to produce high-quality measurements of trace metal elements and associated biogeochemical variables across the global oceans. In this light, it is critical to maintain the observing capabilities and to develop an improved understanding of the mechanisms driving the ocean's trace metal cycling and its impact on the ecosystem and biogeochemical cycling.

3.6 Supporting Information

3.6.1 S1. Model - data comparison method

Observed dFe dataset is obtained from the GEOTRACES 2017 intermediate data product (Schlitzer et al., 2018). To compare the model and data, I used the method of objective mapping to interpolate the modeled dFe concentration along the GEOTRACES cruise tracks onto the grid that has a spatial resolution of 1°in longitude and latitude and vertical resolution of 10m near the surface to 100m at depth. The spatial correlation is assumed to have a Gaussian form with the horizontal decorrelation length scale of 3°. Similarly, observed values are objectively mapped onto the same horizontal and vertical grids. I used

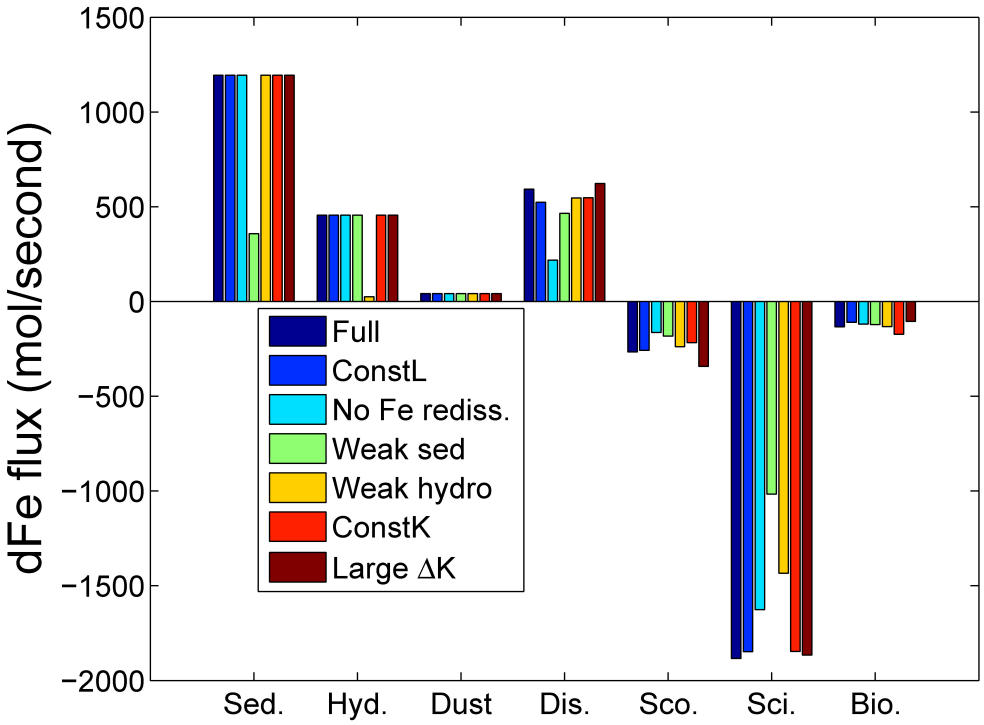

Figure 3.10: The globally integrated sources and sinks of dFe from each of the model runs. ”Sed” is the shelf sediment, and ”hyd” is for hydrothermal source. ”dis” is for release of dFe from remineralization and desorption, and ”sco” and ”sci” are the scavenging onto organic and inorganic particles respectively. ”bio” is for the loss of Fe due to the biological uptake.

the horizontal decorrelation length scale of 3 - 10°and the vertical decorrelation scale of 10 - 300m.

Table 3.1: Model parameters for *control* and sensitivity runs

	Full	*constL*	*No Fe rediss.*	*Weak sed*	*Weak hydro*
α(unitless)	6.1 $\times 10^{-5}$	0	6.1 $\times 10^{-5}$	same	same
β(unitless)	1.3 $\times 10^{-5}$	same	same	same	same
γ(unitless)	0.5	0	0.5	0.5	0.5
$L_{refract}$(mol/m^3)	2.76 $\times 10^{-6}$	10^{-6}	2.76 $\times 10^{-6}$	same	same
K_1 (L/mol)	10^{12}	10^{12}	10^{12}	10^{12}	10^{12}
K_2 (L/mol)	10^{11}	10^{11}	10^{11}	10^{11}	10^{11}
Total L (mol/m^3)	variable	10^{-6}	variable	variable	variable
k_{org} ($m^3 \mathrm{g}C^{-1}s^{-1}$)	1.16 $\times 10^{-5}$	same	same	same	same
k_{inorg} (s^{-1})	2.0 $\times 10^{-7}$	same	same	same	same
R_{FeP} (unitless)	variable	variable	$R_{FeP(eu)}$	variable	variable
Global Sed.dFe flux(mol/s)	11938	11938	11938	358.1310	11938
$dFe/^3$He	variable	variable	variable	variable	4.5$\times 10^8$

CHAPTER 4
LIGAND BINDING STRENGTH EXPLAINS THE DISTRIBUTION OF IRON IN THE NORTH ATLANTIC OCEAN

This chapter is modified from an article published in *Geophysical Research Letters* as

Pham, A.L.D. and T. Ito, (2019) Ligand binding strength explains the distribution of iron in the North Atlantic Ocean, Geophys. Res. Lett., GRL59159, doi: 10.1029/2019GL083319

Abstract

Observations of dFe in the subtropical North Atlantic showed remarkable features: While the nearsurface dFe concentration is low despite receiving high dust deposition, the subsurface dFe concentration is high. In this chapter, I test several hypotheses that might explain this feature in an ocean biogeochemistry model with a refined Fe cycling scheme. These hypotheses invoke a stronger lithogenic scavenging rate, rapid biological uptake, and a weaker binding between Fe and a ubiquitous, refractory ligand. While the standard model overestimates the surface dFe concentration, a 10-time stronger biological uptake run causes a slight reduction in the model surface dFe. A tenfold decrease in the binding strength of the refractory ligand (from 10^{11} to $10^{10} L/mol$), suggested by recent observations, starts reproducing the observed dFe pattern and can significantly impact the global nutrient distribution. An extreme value for the lithogenic scavenging rate can also match the model dFe with observations, but this process is still poorly constrained.

4.1 Introduction

Fe is a crucial element in the marine ecosystem and biogeochemistry because it is one of the limiting nutrients for the phytoplankton growth (Boyd and Ellwood, 2010; Moore et al.,

2013). The GEOTRACES program is rapidly expanding the data coverage for the global Fe distribution over the last decade (Mawji et al., 2015; Schlitzer et al., 2018), which provides an excellent opportunity to advance our understanding of the ocean Fe cycling. One region of special interest is the oligotrophic subtropical North Atlantic, where the concentrations of dissolved and particulate Fe and their isotopic compositions are measured along the zonal (GA03) and meridional (GA03e) transects by the USGT10 and USGT11 cruises (Boyle et al., 2015; Conway and John, 2014; Fitzsimmons et al., 2015; Hatta et al., 2015). In this region, the biological productivity is considered to be less sensitive to Fe than to macronutrients (Moore et al., 2013). However, several observational and experimental studies showed that the availability of Fe here can limit the growth of nitrogen-fixing cyanobacteria and the phosphate acquisition by microbial community (Browning et al., 2017; Moore et al., 2009, 2006). In addition, this region has a dynamic Fe cycling with multiple Fe supplies from both internal cycling and external inputs (Conway and John, 2014; Hatta et al., 2015). Moreover, globally significant water masses are formed in the North Atlantic, and their preformed dFe can influence the far field via long-range transport (Conway et al., 2018). It is thus important to understand processes controlling the dFe distribution in this region.

The zonal and meridional GA03 transects reveal a unique feature of the dFe pattern in the subtropical North Atlantic. Despite receiving high dFe input from atmospheric deposition, the surface dFe concentration is relatively low (0.3 - 0.5 nM) (Figure 4.1)). In contrast, 9 out of 13 current ocean general circulation and biogeochemistry models (OGCBMs) compiled by Tagliabue et al., (2016) have a relatively high surface dFe concentration ($\sim$ 1-2 nM). Furthermore, the observed subsurface dFe maximum (1.4 - 1.6 nM) (Figure 4.1) are underestimated by 7 of 13 models included in Tagliabue et al., (2016). These models encapsulate our mechanistic understanding of the Fe cycling through parameterizations of relevant biochemical processes, thus these biases indicate gaps in our understanding.

Several hypotheses have been suggested to explain this unique feature and resolve the

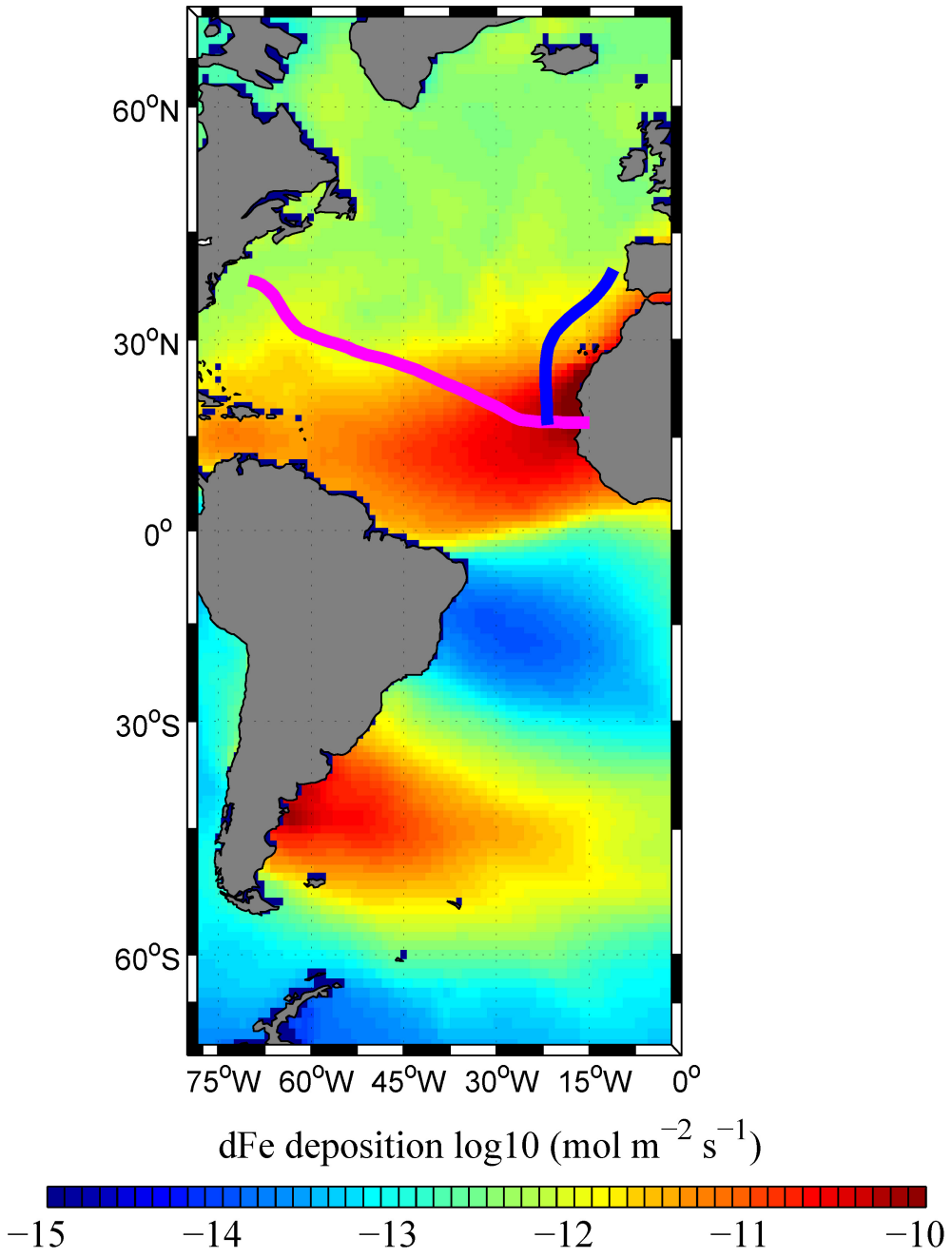

Figure 4.1: Atmospheric dFe deposition over the Atlantic Ocean used in this study. Blue and magenta lines indicate the tracks of the meridional GA03e and zonal GA03 cruises from GEOTRACES program, respectively.

systematic model biases. First, a recent model study suggested a stronger scavenging by lithogenic particles as a possible mechanism to decrease the surface dFe where dust deposition is high (Ye and Völker, 2017). Second, the Fe uptake rate of phytoplankton can significantly increase under the high dust plume to rapidly consume dFe. Twining and Baines, (2013) and Twining et al., (2015) showed a 3-fold higher for Fe quota in the North Atlantic cells, compared with those measured in the Pacific and Southern Oceans. However, the efficiency of these two mechanisms depends on the concentration and binding strength of organic ligands due to their dFe protection against removal processes (Tagliabue et al., 2017). Ye and Völker, (2017) pointed out that if their model uses a dynamic ligand scheme instead of a globally uniform ligand concentration of 1nM, it requires a greater lithogenic scavenging rate in order to bring the model surface dFe concentration closer to observations. While there has been significant advances in our understanding of ligands thanks to the expanding GEOTRACES dataset and experimental studies (Boiteau and Repeta, 2015; Buck et al., 2015; Gerringa et al., 2016), there still is a significant uncertainty in the ligand sources, sinks, and binding strength with $[Fe']$) (Hassler et al., 2017). This uncertainty leads to uncertainties on the relative importance of retention and removal processes in regulating the dFe distribution in the subtropical North Atlantic and how these processes might change in the future (Hutchins and Boyd, 2016; Tagliabue et al., 2016).

The objective of this chapter is to explore which mechanism would best explain the Fe distribution in the subtropical North Atlantic by performing a suite of sensitivity experiments in an OGCBM. Specifically, I purposefully alter different aspects of the model Fe parameter in each experiment and analyze the resulting dFe pattern. The model includes all major processes controlling the ocean Fe cycle such as dFe inputs from atmospheric dust, bottom sediment and hydrothermal sources, dFe scavenging onto and release from lithogenic and organic particles, biological dFe uptake, and dFe retention by spatially-varying ligands. The development of this model is documented in chapters 2 and 3, which shows major improvements in the large-scale ocean dFe distribution (Pham and Ito, 2018).

4.2 Model Configuration and Experimental Design

4.2.1 Model Configuration

The ocean biogeochemistry model used in this chapter is essentially the same as the model used in chapter 3 (Pham and Ito, 2018), which is based on the MITgcm model described in chapter 2.

As in chapter 3, I consider three ligand classes. L_1 is assumed to be the biologically produced siderophores with relatively high binding strength (Adly et al., 2015; Macrellis et al., 2001). This ligand class is parameterized as a linear function of the DOP concentration in the model, $L_1 = \alpha[DOP]$, and is given the strongest conditional stability constant of K_{L1} = 10^{12} L/mol. L_2 is essentially the DOC produced from the remineralization of particulate organic matter (Laglera and Berg, 2009; Velasquez et al., 2016; Vraspir and Butler, 2009). This ligand class is parameterized as a linear function of the AOU, $L_2 = \beta AOU$, and its binding strength is set to K_{L2} = 10^{11} L/mol. Different from chapter 3, in this chapter, I vary the binding strength (conditional stability constant) for L_3, which represents the refractory DOC (Hassler et al., 2011), from 10^{10} - 10^{11} L/mol in the sensitivity experiments. This variation in the binding strength of L_3 comes from the uncertainty in the binding strength of the refractory, humic-like L_3, as several studies reported to be weaker than 10^{11} L/mol (Gledhill and Buck, 2012). Given that $\sim$ 15 - 40% of the dFe speciation in the water column is FeL_3 (Figure 2.4 - Chapter 2), a decrease in the mean dFe concentration is anticipated. Following Pham and Ito, (2018), the empirical constants in this ligand parameterization are calibrated to fit the observed ligand distribution in the least squares sense (α = $6.1 \cdot 10^{-5}$, β =$1.3 \cdot 10^{-5}$), and $L_{refract} = 1.3nM$.

As described in chapter 2, dFe not bound to ligands (free Fe, $[Fe']$) can be removed from the water column by scavenging onto lithogenic and organic particles, based on a first-order bulk scavenging rate, and by precipitation. The scavenging of $[Fe']$ by lithogenic (inorganic) particles is enhanced under the high dust plume when lithogenic particle con-

centration increases (Ye and Völker, 2017; Ye et al., 2011). To represent this effect, I scale the inorganic scavenging rate k_{inorg} by atmospheric dust deposition (JFe_{dust}):

$$k_{inorg} = k_{inorg0} \left(\frac{JFe_{dust}}{\langle JFe_{dust} \rangle} \right)^n \tag{4.1}$$

In this chapter, the exponent n for the dust-flux dependence is set to 1 for the control simulation as in chapter 3 (Pham and Ito, 2018), but it is varied in the sensitivity runs.

4.2.2 Experimental Design

First, the model was integrated for 1,000 years with a standard parameterization (*Control* run) to reach a quasi-steady state. Five additional experiments were then started from the end of the *control* run with perturbed parameterizations, and were further run for 1,000 years to achieve new quasi-steady states. These experiments aim to evaluate the roles of various processes controlling the ocean dFe cycling in the subtropical North Atlantic. Model experiments are setup as follows:

- "*Control*" run applies the ligand and scavenging parameterizations as in Pham and Ito, (2018); ($K_{L3} = 10^{11} L/mol$, $n = 1$)
- "*Stronger scav.*" run allows a stronger inorganic scavenging rate in the surface water under the high dust deposition; ($K_{L3} = 10^{11} L/mol$, $n = 1.5$)
- "*Stronger uptake*" run has the same setup as the *Control* run but with a 10 times bigger biological uptake ratio between Fe and P
- "*Weaker L3*" run sets a weaker binding strength for L_3; ($K_{L3} = 10^{10} L/mol$, $n = 1$)
- "*Stronger scav. + weaker L3*" run is the combination of the *Weaker L3* run and *Stronger scav.* runs; ($K_{L3} = 10^{10} L/mol$, $n = 1.5$)
- " *Stronger scav. 2*" run allows a stronger inorganic scavenging rate under the high dust deposition for the whole euphotic layer (0-200m); ($K_{L3} = 10^{11} L/mol$, $n = 1.5$)

The *Stronger scav.* and *Weaker L3* runs examine the relative roles of ligand and scavenging in modulating the subtropical North Atlantic Fe cycling. The effect of increasing the power-law dependence (n) in the *Stronger scav.* and *Stronger scav. 2*" experiments roughly translates to a 1000-fold increase in the net scavenging rate relative to the reference value (K_{inorg0}) under the high dust plume. The difference between these two runs is that the *Stronger scav. 2* allows the increase in inorganic scavenging rate not just only at the surface water but also throughout the surface water column (200m). These experiments explore the uncertainty regarding the impact of a potentially high lithogenic scavenging rate on the upper ocean dFe distribution in the subtropical North Atlantic. The *Stronger scav. + weaker L3* run evaluates the combination effect of a weaker refractory-DOC component ligand class and a stronger inorganic scavenging rate. The *Stronger uptake* run investigates the uncertainty associated with the Fe-P uptake ratio of phytoplankton, as reported by a wide range for this value in Twining and Baines, (2013). Twining et al., (2015) shows a 3-fold higher Fe quota in the North Atlantic cells, compared with those measured in the Pacific and Southern Ocean, which may have an impact on the surface dFe concentration in this region.

4.3 Mechanisms Controlling the dFe Distribution in the Subtropical North Atlantic

Our model-data comparison is focused in the upper 1,000m, thus I zoom in the depth from 0 - 1,000m in Figures 4.2 and 4.3 and compress the rest of the water column. In addition, the pattern correlations between model runs and observations and mean model biases are calculated for the surface (0-250m), subsurface (250-1000m), and the upper 1,000m waters (Table 4.1).

The *control* run reproduces some features of the subsurface dFe maximum signals observed in both the western and eastern margins, which are formed by remineralization and/or by the dFe release from the adjacent reduced sediments (Hatta et al., 2015). However, as is the case with most models included in Tagliabue et al., (2016), it overestimates

the surface dFe concentration by $\sim$ 0.7 - 0.8 nM and underestimates the vertical and horizontal extent of the mid-depth dFe maximum in the eastern margin (Figures 4.2a and 4.3a). This leads to a model subsurface dFe maximum shallower than observed. The strong dFe gradients around 200m - 600m from 60 - 40°W (Figure 4.2a) and near the surface from 30 - 40°N (Figure 4.3a) are not reproduced in the model because the dFe concentration there is higher than observed. Thus, the pattern correlations between the *control* run and observations are low (0.44 and 0.54 for the upper 1000m water column of the GA03e and GA03 transects, respectively) and the mean model biases are generally positive (0.15 and 0.26) (Table 4.1). Our model is also not able to reproduce the high dFe hydrothermal level observed at 3,000-4,000m from 50 - 40°W.

A stronger inorganic scavenging rate in the surface water (*stronger scav.* run) slightly decreases the surface dFe concentration in both transects by $\sim$ 0.3 nM (Figures 4.2c and 4.3c), moderately increasing the pattern correlations with observations for the upper 1,000m water column relative to the control run (from 0.44 to 0.55 and from 0.54 to 0.66 - Table 4.1). The mean model biases in the upper 1,000m also decrease as more dFe is scavenged by lithogenic particles. However, the subsurface (200-1,000m) dFe maximum in the eastern margin is still shallower than observed. Observed subsurface dFe gradients in the central subtropical gyre (around 40°W in Figure 4.2c) and in the eastern subtropics (around 30°N in Figure 4.3c) are still not reproduced.

Allowing the inorganic scavenging rate to be increased from 0-200m under the high dust plume (*Stronger scav. 2* run) significantly decreases the dFe concentration in the surface water by more than 1 nM (Figure 4.5). The mean model biases are significantly decreased in the upper 1000m to negative values (Table 4.1). However, the subsurface dFe maximum in the eastern margin also decreases by more than 1 nM and further underestimates the observed subsurface dFe concentration, even though this dFe maximum signal starts to appear in a deeper level than the *control* run. Overall, the model thermocline dFe concentration in this run underestimates the observations, except for the extreme dFe signal

around 800-1000m in the western margin (Figure 4.5). The diminishing subsurface dFe is caused by the intense inorganic scavenging in this run, reducing the transport of dFe from the surface to subsurface waters. In contrast, the model subsurface dFe maximum in the western margin seems to overestimate observations, implying different formation mechanisms. The high level of dFe there might be formed via the subsurface dFe supply from continental shelves (Hatta et al., 2015), thus not being affected by the reduction of dFe transport from the surface. The pattern correlation with the observation is 0.1 and is much lower than the control run (Table 4.1) due to a greater misfit in the subsurface dFe concentration. The result of this sensitivity run implies that an extremely high scavenging rate in the upper water column could eventually bring the model surface dFe concentration down to the observed level but at the expense of further decreasing the model subsurface dFe.

The *stronger uptake* run applies a ten times higher value for the Fe-P uptake ratio (R_{FeP}), but its effect on the surface dFe concentration seems to be relatively minor when compared with the *control* run (Figures 4.2d and 4.3d). This experiment is intended to assess the ecosystem response to the high dust deposition by allowing a higher rate of dFe uptake under the dust plume. In our model, the biological productivity in the oligotrophic subtropical North Atlantic region is low due to the macronutrient limitation (Moore et al., 2013). Therefore, an increase in the uptake Fe-P ratio in this particular model did not show a major shift in the regional biological activity and dFe distribution. It is beyond the scope of this study to examine the response of nitrogen-fixing bacteria in the large and episodic dust dFe deposition (Moore et al., 2009), which requires an explicit ecosystem component.

The *weaker L3* run shows significant improvements. It significantly decreases the surface dFe ($\sim$ 0.8 nM) and deepens the subsurface dFe maximum (Figures 4.2e and 4.3e). When the binding strength of L_3 is decreased, dust-deposited dFe is more effectively scavenged onto sinking organic particles, which then release dFe back at mid-depth waters via remineralization. Thus, lowering the binding strength of L_3 is an effective mechanism not only in reducing the model surface dFe concentration but also in redistributing the model

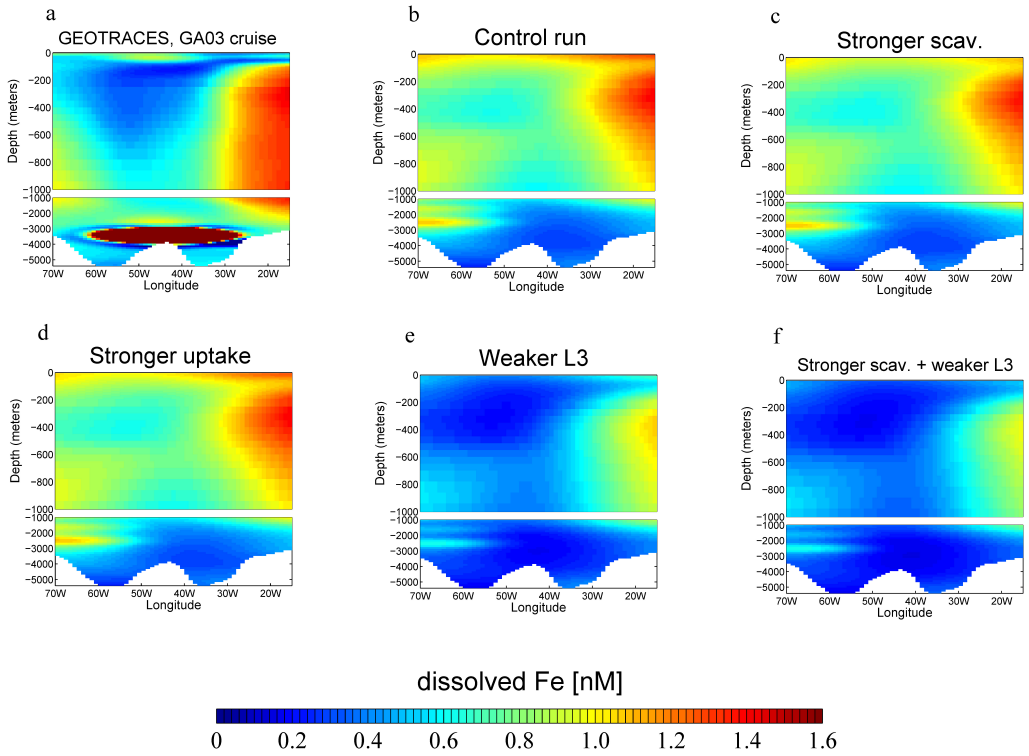

Figure 4.2: dFe distribution along the zonal GA03 transect: (a) *Observations*, (b) *Control* run, (c) *Stronger scav.* run, (d) *Stronger uptake*, (e) *Weaker L3* run, and (f) *Stronger scav. + weaker L3* run . White color indicates the seafloor bathymetry.

dFe into the thermocline. This model run also reproduces the strong dFe gradients around 200 - 600m around 40°W (Figure 4.2e) and near the surface water around 30°N (Figure 4.3e). The pattern correlations between the model and observation are greatly improved from the control run (improving from 0.44 to 0.72 for the meridional GA03e transect and from 0.54 to 0.89 for the zonal GA03 - see Table 4.1). The mean model biases also shift to underestimation of the upper 1,000m water (-0.25 for GA03e and -0.19 for GA03). However, the thermocline (200-1,000m) dFe concentration is decreased in magnitude, especially in the western margin. As discussed above, the high level of dFe in the western margin is likely to be formed by the dFe sedimentary source, not by the redistributing of dust-deposited Fe between the surface and subsurface waters as in the eastern margin.

I further examine underlying mechanisms behind changes in the sensitivity runs by ana-

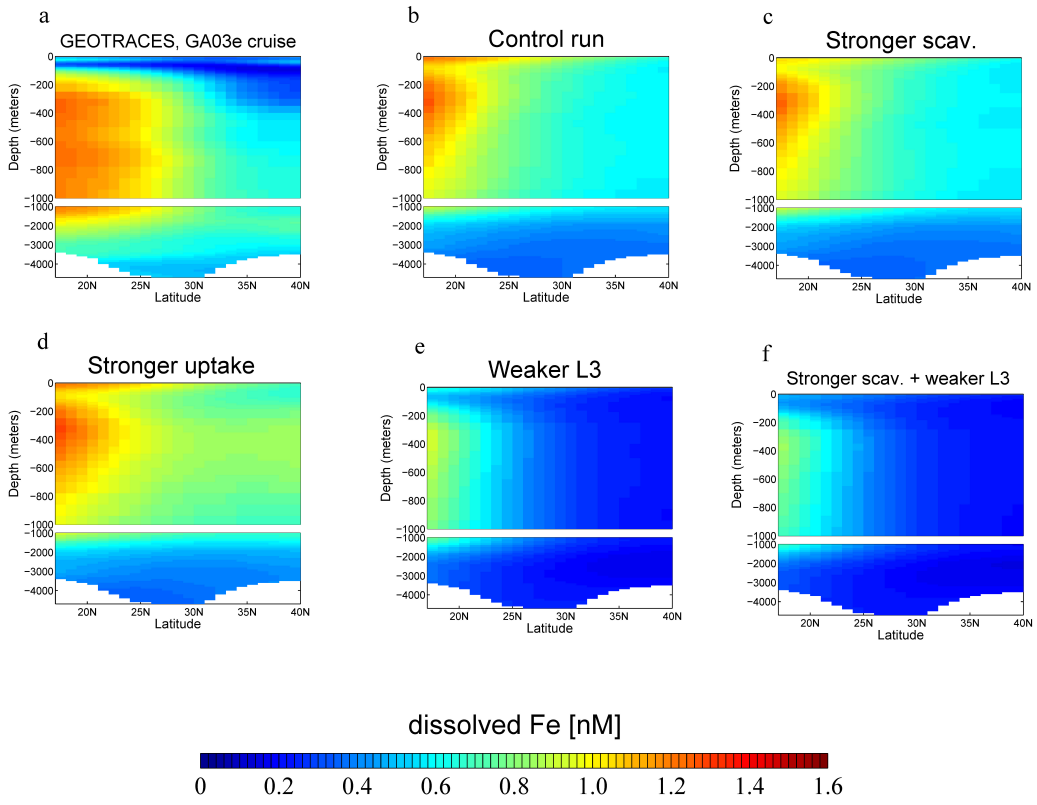

Figure 4.3: dFe distribution along the meridional GA03e transect: (a) *Observations*, (b) *Control* run, (c) *Stronger scav.* run, (d) *Stronger uptake*, (e) *Weaker L3* run, and (f) *Stronger scav.* + *weaker L3* run. White color indicates the seafloor bathymetry.

lyzing changes in the average dFe removal fluxes of each sensitivity run relative to the *Control* from 0-100m along 30°-15°W, 15°-25°N. Figure 4.4 shows 4 groups of bar chart for 4 model scenarios with each color representing different terms in the dFe removal fluxes. In the *Strongscav1* run, the inorganic scavenging increases by $\sim$ 0.18 $nM/year$ (light blue) relative to the *Control* at the expense of decreasing the other sink terms, especially the organic scavenging (dark blue). The lower concentration of dFe reduces the biological consumption (brown) and the production of particulate organic Fe (dark blue), leading to a modest decrease of the surface dFe concentration in this run. It is possible to significantly decrease the surface dFe by further increasing inorganic scavenging rate (*Strong scav. 2* run). Similar to the previous run, the other removal fluxes partially compensate for increased scavenging loss due to the decreased availability of dFe and biological production, but the inorganic scavenging flux is significantly increased ($\sim$ 0.4 $nM/year$) and dominates the dFe balance. As a result, it causes a large decrease ($\sim$ 1 nM) in the surface dFe concentration, but it also reduces the transport of dust-deposited dFe from the surface to subsurface waters, leading to underestimation of the subsurface dFe concentration. In the *Strong uptake* run, biological uptake increases by less than 0.1 $nM/year$ (brown bar), and changes in the other fluxes are even smaller. The impact of increasing biological uptake is insignificant due to the macro-nutrient limitation in this region. In the *Weaker L3* run, the total removal flux is similar to the *Strong scav. 2* (2.9 vs. 2.8 $nM/year$). However, the underlying mechanisms for increasing dFe removal fluxes are different. While the decrease of surface dFe in the *Strong scav.2* run relies solely on inorganic scavenging, the *Weaker L3* run decreases ligand binding strength, thereby enhancing both organic and inorganic scavenging fluxes. The difference in organic scavenging flux ($\sim$ +0.15$nM/year$) between *Weaker L3* and *Strong scav.2* enhances the downward transport of dFe through remineralization, thus improving the model dFe distribution in the thermocline.

A combination of both mechanisms (stronger inorganic scavenging at the surface + weaker L_3) further decreases the surface dFe concentration (Figures 4.2f and 4.3f). The

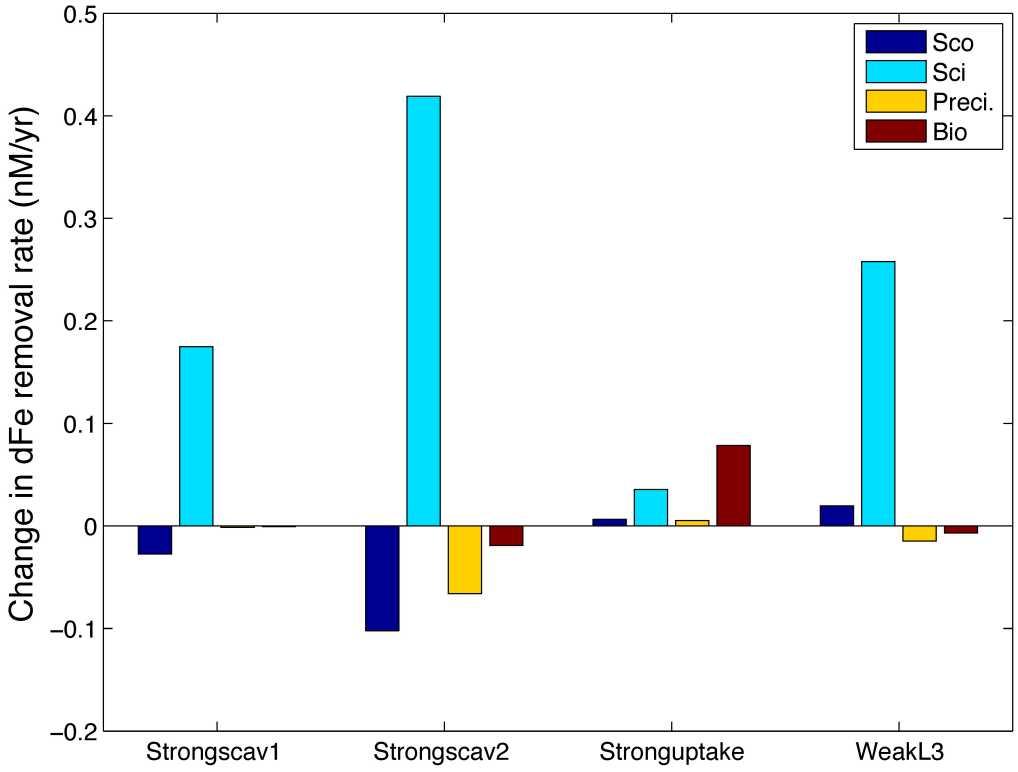

Figure 4.4: Changes in the average dFe removal fluxes ($nM/year$) from 0-100m along 30°-15°W, 15°-25°N for each sensitivity run relative to the control run. The dark blue, light blue, yellow, and brown bars indicate the removal fluxes from (Sco) organic scavenging, (Sci) inorganic scavenging, (Preci) precipitation, and (Bio) biological uptake, respectively.

eastern subsurface dFe maximum also seems to be further decreased. While the mean bias (underestimation) is slightly enhanced (Table 4.1), there is little change in the pattern of the dFe distribution between this run and the *weaker L3* run. Indeed, the pattern correlations between model and observations are essentially the same between these two runs. Comparison of all the sensitivity runs in Figures 4.2, 4.3, and 4.5 suggests that weakening the binding strength of L_3 is the mechanism that best explains dFe pattern in the subtropical North Atlantic and reduces model biases.

4.4 Discussion and Conclusion

The improved spatial coverage and quality of Fe data provides a unique opportunity to evaluate our understanding of the ocean Fe cycling (Mawji et al., 2015; Schlitzer et al., 2018). This study focused on the subtropical North Atlantic Ocean, where current OGCBMs have difficulty reproducing the observations (Tagliabue et al., 2016). This region is important for studying the ocean Fe cycling because of its diverse dFe sources and sinks, and the complex internal cycling of dFe within the water column (Conway et al., 2018; Hatta et al., 2015). Moreover, the dFe cycling in this region can have far-reaching impact on the global marine biogeochemistry and ecosystems because of the formation of deep water masses that transport preformed Fe to far-field regions and because of its control on the growth of nitrogen-fixing bacteria. As the subtropical North Atlantic receives high dust deposition (Conway and John, 2014), many models included in Tagliabue et al., (2016) show a relatively high surface dFe concentration of 1 - 2 nM. In contrast, the observed surface dFe is relatively low with a magnitude of 0.3 - 0.5 nM (Hatta et al., 2015). On the one hand, this feature indicates that these models underestimate the near-surface dFe sink including scavenging and/or biological uptake. On the other hand, the degree to which these mechanisms can decrease the surface dFe depends on the concentration and binding strength of ligands, which are still uncertain (Gledhill and Buck, 2012; Hassler et al., 2017). This study examines the relative importance of different mechanisms behind the observed dFe

patterns in the subtropical North Atlantic through model experiments in an OGCBM with an improved Fe cycling scheme (Pham and Ito, 2018).

The sensitivity run with a 10 times higher value for the biological uptake ratio R_{FeP} only has a negligible impact on the 0-1,000m dFe pattern due to the macronutrient-limited biological production in this region. A sensitivity run with a stronger lithogenic scavenging rate lowers the surface dFe concentration but causes a significant negative bias in the thermocline dFe concentration. In contrast, a sensitivity run with a 10 times weaker refractory ligand class significantly reduces the model surface dFe while sustaining the subsurface dFe maximum at a similar level to observations by increasing the release of scavenged Fe in the thermocline. Thus, a 10 times weaker binding strength for L_3 leads to a significant improvement in the pattern correlation between model and observations.

The observed ligand data has been greatly expanded over the last few years thanks to the GEOTRACES program (Buck et al., 2018, 2015; Gerringa et al., 2015). Several modeling studies have taken advantage of these data to develop a dynamic ligand scheme in OGCBMs, which could significantly improve the model ligand and dFe representations (Völker and Tagliabue, 2015). However, given a large uncertainty in the ligand binding strength, those models still represent only one ligand class, which is considered to be the most dominant and has the binding strength of $10^{11} L/mol$ (Völker and Tagliabue, 2015; Ye and Völker, 2017). Our results argue for the inclusion of different ligand classes, each with distinct sources and binding strength. Representing the refractory ligand L_3 with a weak binding strength of $10^{10} L/mol$ significantly improved our model in the subtropical North Atlantic. Our results are thus in line with a recent review on the ligand classification, which suggests a ligand spectrum of three groups (Hassler et al., 2017). In addition, the model binding strength of L_3 (K = $10^{10} L/mol$) is consistent with the measurement of Buck et al., (2015) for the weakest ligand class along the GA03 transect. Nevertheless, our simple ligand parameterization should be considered as only a first step towards a mechanistic ligand model, which should dynamically represent a continuum of ligand classes, rather

Table 4.1: The pattern correlations and mean biases (values in the parentheses) between model experiments and observations for the two subtropical Atlantic transects

Model	GA03e 0-1000m	GA03e 0-250m	GA03e 250-1000m	GA03 0-1000m	GA03 0-250m	GA03 250-1000m
Control	0.44 (0.15)	0.6 (0.33)	0.89 (-0.12)	0.54 (0.26)	0.71 (0.40)	0.84 (0.05)
Stronger scav.	0.55 (0.12)	0.68 (0.28)	0.9 (-0.14)	0.66 (0.22)	0.8 (0.34)	0.85 (0.03)
Weaker L3	0.72 (-0.25)	0.74 (-0.12)	0.92 (-0.46)	0.89 (-0.19)	0.81 (-0.15)	0.95 (-0.26)
Stronger scav. + weaker L3	0.77 (-0.28)	0.79 (-0.16)	0.92(-0.48)	0.90 (-0.25)	0.83 (-0.21)	0.95 (-0.3)
Stronger scav.2	0.4 (-0.22)	-0.62 (-0.13)	0.66(-0.38)	0.1 (-0.19)	-0.34(-0.16)	0.21 (-0.37)
Stronger uptake	0.56 (0.24)	0.63 (0.38)	0.71(0.012)	0.59 (0.26)	0.7 (0.38)	0.85 (0.06)

than a few discrete ones. The long-lived refractory-DOC ligand class can be a crucial factor for the Fe cycling in the subtropical North Atlantic, where ligand sources from microbial activity and remineralization are limited due to the low biological production (Buck et al., 2015). Given the ubiquitous and longevity of this ligand class, its binding strength and concentration could have an important impact on the global Fe distribution, especially for the Fe-depleted surface waters. Strong lithogenic scavenging and high biological Fe uptake could also play some roles but their effects are likely confined within regions of high dust deposition.

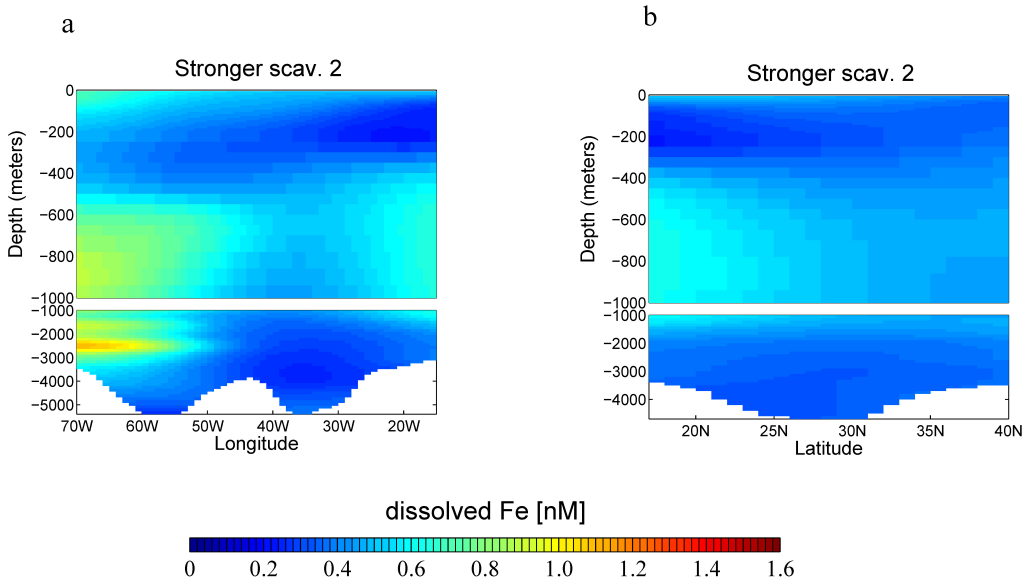

Figure 4.5: The dFe distribution along the horizontal GA03 (a) and meridional GA03e (b) transects of the model *Stronger scav. 2 run*. White color indicates the seafloor bathymetry.

CHAPTER 5
UPPER OCEAN IRON PATTERNS CONTROLLED BY INTERNAL CYCLING PROCESSES

Manuscript in preparation as

Pham, A.L.D. and T. Ito, (2019) Upper ocean iron patterns controlled by internal cycling processes

Abstract

Recent advances in measurement techniques and collaborative efforts rapidly expands the dataset of dFe distribution across the global oceans, which provides a unique opportunity to improve our understanding of the ocean Fe cycling. Previous efforts focused on constraining the magnitude of external dFe inputs such as hydrothermal vents and shelf sediments. However, biochemical processes within the water column also affect observed concentrations, and their interactions with diverse dFe sources are not yet fully understood. Here I show that the oceanic processing of Fe controls the observed gradients of dFe in the upper ocean through a series of computational experiments. Simulated dFe distributions are validated against observations, and the chemical mass balance is analyzed by the application of an unsupervised machine learning technique. Distinct regimes of dFe mass balance emerge, showing that the complex interior ocean Fe processes play a central role in setting the upper ocean dFe gradients. Even though external dFe inputs are an important factor setting the overall magnitude of dFe concentration in our model, the observed patterns cannot be captured without an appropriate set of internal cycling processes.

5.1 Introduction

Over the last three decades, the crucial role of the micronutrient Fe as a limiting factor for phytoplankton growth has been well established and its distribution in the ocean has been actively measured (Tagliabue et al., 2017). Starting from around 300 vertical profiles of dFe concentration spread out over several ocean stations in the 1990s (Johnson et al., 1997), we currently possess a global dFe dataset of more than 20,000 measurements (Tagliabue et al., 2016, 2012). This nearly 100-fold increase in the number of high-quality dFe measurements has significantly transformed our understanding of processes regulating the ocean dFe pattern. Started from a highly simplified conceptual dFe model in the ocean with atmospheric dust as the only external source (Archer and Johnson, 2000; Johnson et al., 1997), the key role of dFe inputs from hydrothermal vents and continental margins, especially in the Southern Ocean, has been revealed (Ardyna et al., 2019; Resing et al., 2015; Tagliabue et al., 2014b). In addition, a traditional assumption of a nearly constant value of 0.6 nM for deep dFe concentration has been replaced by a much more dynamic view where it varies significantly across the abyssal basins (Tagliabue et al., 2017). Deep dFe variability likely reflects major subsurface sources as well as the variation in the concentration and binding strengths of organic ligands that protect dFe from being removed by particle scavenging (Buck et al., 2018, 2015). Expansion in the dFe dataset also puts a more stringent constraint on computational models of ocean Fe. Comparison with observations along GEOTRACES sections showed significant biases in many ocean biogeochemistry models (Tagliabue et al., 2016). Models that incorporated new findings displayed improvements in reproducing some observed features (Pham and Ito, 2018; Pham and Ito, 2019; Tagliabue et al., 2016).

Despite the progress made, uncertainties persist. The mean residence time of dFe, calculated as the ratio between the global inventory and the rate of external supply, varies over two orders of magnitude among state-of-the-art models (Tagliabue et al., 2016). This vari-

ation reflects a wide range in the magnitude of total dFe fluxes from the continental shelves and hydrothermal vents. These models can maintain the dFe inventory close to observations ($\sim 1nM$) because of the non-linear removal processes mediated by organic ligands. Models are typically programmed to rapidly scavenge dFe if it is not bound to ligands, such that a large influx of dFe is often accompanied by an equally large scavenging loss. Parameterizations for ligands can therefore play a crucial role in setting dFe distribution (Pham and Ito, 2018; Pham and Ito, 2019). While previous studies have placed much emphasis on constraining magnitudes and contributions of external fluxes (Conway and John, 2014; Frants et al., 2016; Holzer et al., 2016), the role of interior ocean processes such as retention, scavenging, desorption, and remineralization has just recently come into focus (Boyd et al., 2017).

In this study, I aim to elucidate the relative contributions of external dFe inputs and oceanic Fe processes by performing four model simulations with different levels of complexity in external dFe inputs and oceanic Fe processing in the same three-dimensional ocean circulation model (ECCO-MITgcm (Marshall et al., 1997a,b; Wunsch and Heimbach, 2007)). In addition, I analyze how the vertically integrated dFe budgets are balanced in the upper 1000m ocean in these simulations by using the unsupervised machine learning technique (K-means). In general, eight dFe fluxes contribute to the balance of the dFe budgets: advection, mixing, biological uptake, remineralization (including desorption), scavenging, atmospheric dust, shelf sediment, and hydrothermal fluxes. Of these eight dFe fluxes, dust, shelf sediment, and hydrothermal fluxes are considered external fluxes, whereas the rest are interior oceanic processes. This clustering algorithm organizes the model's ocean into finite groups/regions of similar dFe balance, thereby demonstrating how the dFe fields in four simulations are regulated by various mechanisms.

This chapter is structured as follows. Section 5.2 describes the model and Fe schemes used in four simulations and the K-means clustering algorithm. Section 5.3 presents the results of these simulations and the dFe budget analysis. Section 5.4 discusses these results'

implications and concludes this chapter.

5.2 Methods

5.2.1 Ocean biogeochemistry models

The three-dimensional ocean circulation model (ECCO-MITgcm) used in this study was described in details in Chapter 2. Four simulations were setup as follows: Model *sFe-dust*, Model *sFe-all*, Model *cFe-dust*, and Model *cFe-all*. While Models *sFe-dust* and *cFe-dust* considered atmospheric dFe deposition as the only external source, Models *sFe-all* and *cFe-all* included dFe fluxes from bottom sediments and hydrothermal vents. More important, Models *sFe-dust* or *sFe-all* and *cFe-dust* or *cFe-all* were significantly different in their representations of interior oceanic Fe processes. Models *sFe-dust* and *sFe-all* represented a simple oceanic Fe processing including a single, uniform ligand with a relative strong binding strength with dFe ($K_L = 10^{11} L/mol$) and dFe scavenging removal onto organic particles. This scavenging loss was considered as a first-order loss process depending on the concentration of organic particles (organic scavenging). In contrast, Models *cFe-dust* and *cFe-all* used a more complex oceanic Fe processing (Pham and Ito, 2019) including three spatially varying ligand classes, scavenging onto organic and lithogenic particles, desorption and remineralization of scavenged Fe. Essentially, the scheme for oceanic dFe processes in Models *sFe-dust* and *sFe-all* was the approach by (Parekh et al., 2005), whereas the scheme for oceanic dFe processes in Models *cFe-dust* and *cFe-all* was the scheme I described in chapter 2 of this dissertation.

5.2.2 Unsupervised classification: K-means clustering

K-means clustering is a statistical approach to describe and classify data (Kubat, 2015; MacQueen, 1967). It divides n data points (observations) of a specific dataset into k groups (clusters). The value of k for the number of clusters is a free parameter that is chosen a priori. This division/classification is based on how the data points are distributed in a

parameter space. The dimensions of this parameter space are defined by a set of features that characterize each data point. Specifically, each data point (x) is grouped into a specific cluster such that the Euclidean distance between that data point and the center of that cluster (centroid c) in the parameter space is minimum.

The k-means approach first places centroids of k clusters randomly in the parameter space. It then calculates the distances between all the centroids and all n data points to determine to which cluster a specific data point belongs to (cluster membership).

$$J = ||x^i - c_j||^2; i = 1...n; j = 1...k \tag{5.1}$$

After that, it involves an iterative process in which the centroid of each cluster and its distance to data points are re-calculated at each step. The centroid's position of a cluster in the parameter space is determined as the mean position of all the data points belong to that cluster. This process is repeated until there is no change in the position of c in the parameter space as well as no change in the cluster membership for each data point.

Our goal is to apply K-means clustering to determine the spatial patterns of the model ocean Fe cycling based on mechanisms that dominate the dFe budget balance at each model grid point. For this application, data points in the dataset are all the model grid points. Each model grid point is characterized by all the dFe sources, sinks, and transport terms, which are features defining the parameter space. For Model *sFe-dust* or *cFe-dust* the dFe fluxes are: advection, diffusion (mixing), biological uptake, scavenging, remineralization, and dust deposition. Model *sFe-all* or *cFe-All* has two more fluxes: sedimentary and hydrothermal inputs. Before applying K-means to the dFe budgets, all the dFe flux terms were normalized so that each term has a zero mean and unit variance globally.

Adding more clusters can increase the accuracy of data classification but with the risk of overfitting. An optimal value for the free parameter k - the number of clusters - can be determined using the Bayesian Information Criterion (BIC). BIC provides a measure of the

quality of a statistical model, rewarding increased likelihood and penalizing the number of clusters k (Jones et al., 2019; Sonnewald et al., 2019):

$$BIC = kln(n) - 2ln(\iota) \tag{5.2}$$

where ι is the likelihood and is calculated as follows:

$$\iota = \Sigma_{i=1}^{n} \frac{1}{\sqrt{2\pi\sigma^2}} exp(\frac{(x_i - \hat{\xi}_i)^2}{2\sigma^2}) \tag{5.3}$$

where x_i is the observed data point and $\hat{\xi}_i$ is the prediction, so $(x_i - \hat{\xi}_i)^2$ are the prediction residuals. In this framework, the optimum value of k minimizes the BIC score. For all the model analyses, BIC scores stabilized at $\sim$ k = 50, suggesting that no information is gained by further increasing the number of clusters. Thus, k = 50 was used.

5.3 Results

Comparison with the GEOTRACES transects (Mawji et al., 2015; Schlitzer et al., 2018) demonstrated the improved representation of dFe patterns in Model *cFe-All* (Figures 5.1 and 5.3). All models were driven by identical physical circulation and biological parameterizations; they only differed in external dFe sources and oceanic processing of Fe. The observed dFe vertical gradients and the thermocline dFe maximum in the subtropical GA03 Atlantic Ocean were captured in Model *cFe-All*. Similarly, the strong dFe meridional gradient in the tropical thermocline along the GI04 Indian Ocean transect was well represented. The strong subsurface dFe signals observed in the tropical western Atlantic GA02 and the northwestern Pacific GP02 were also reproduced in this model. Models *cFe-dust* and *cFe-all* employed a more sophisticated parameterization of oceanic Fe processing, and their simulated dFe started to capture the correct sign of the vertical gradients in the thermocline water where the near surface dFe is depleted even under the increased deposition of atmospheric dust. In these two models, the accumulation of dFe in the main thermocline

Table 5.1: The total dFe input, dFe inventory, mean dFe concentration, and mean dFe residence time for four model simulations

Model run	Total dFe input	dFe inventory	mean concentration	mean residence time
Model sFe-dust	2.03 Gmol/yr	$2.73 \cdot 10^{11}$ mol	$2.06 \cdot 10^{-7}$ mol/m^3	134.8 years
Model sFe-all	54.06 Gmol/yr	$8.91 \cdot 10^{11}$ mol	$6.72 \cdot 10^{-7}$ mol/m^3	16.5 years
Model cFe-dust	2.03 Gmol/yr	$4.24 \cdot 10^{10}$ mol	$3.2 \cdot 10^{-8}$ mol/m^3	20.9 years
Model cFe-all	54.06 Gmol/yr	$3.31 \cdot 10^{11}$ mol	$2.5 \cdot 10^{-7}$ mol/m^3	6.13 years

was in part due to the remineralization and desorption of Fe from sinking particles. Model *cFe-dust* considered atmospheric deposition as the sole dFe input, thus it generally underestimated the water column dFe concentration. In contrast, Models *sFe-dust* and *sFe-all* employed a simple ocean Fe processing, and they failed to reproduce the correct sign of the dFe vertical gradients. Specifically, these two models overestimated the near-surface dFe under the high dust regions and exhibited nearly uniform deep dFe concentration. Model *sFe-dust* exhibited lower water column dFe concentration due to the lack of hydrothermal and sedimentary dFe, while Model *sFe-all* significantly overestimated both the surface as well as deep dFe concentrations.

The mean residence time of dFe in four simulations spanned two orders of magnitude from 6.1 years (Model *cFe-all*, see Table 4. 1) to 135 years (Model *sFe-dust*). As expected, the inclusion of sedimentary and hydrothermal Fe inputs shortened the residence time significantly in Models *sFe-all* and *cFe-all*. The inclusion of complex oceanic processing also reduced the mean residence time of dFe and decreased the total ocean dFe inventory when compared between Models *sFe-dust* and *cFe-dust* or between Models *sFe-all* and *cFe-all*, which had the same external dFe sources. In Models *cFe-dust* and *cFe-all*, the production of organic ligand was linked to biological productivity with feedback onto the dFe concentration. Specifically, when the biological activity is weak, the ligand production is reduced, resulting in less retention of dFe that decreases the Fe inventory.

Simulated dFe budget terms, which were calculated online and recorded annually, were analyzed using the unsupervised machine learning technique (K-means). Specifically, this clustering algorithm analyzed dFe fluxes at each model's grid points (Figure 5.2bdfh) and

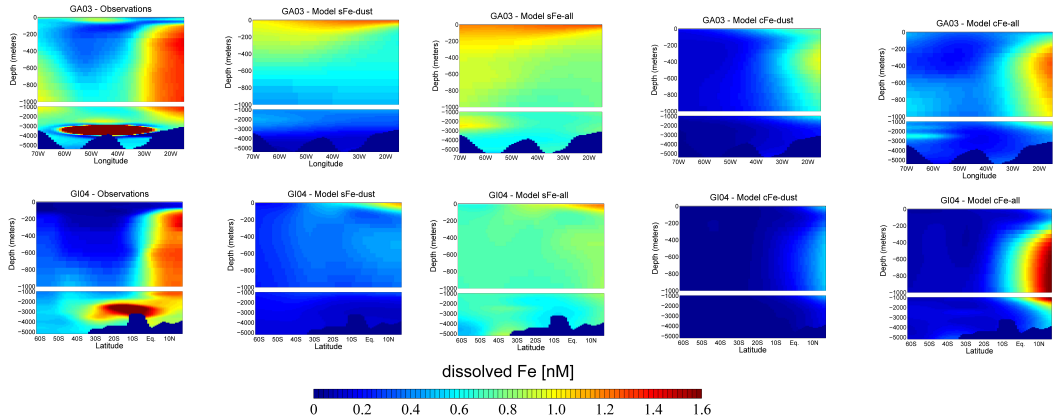

Figure 5.1: dFe distribution along the GEOTRACES transect GA03 (top) and GI04 (bottom). From left to right: First column: measurements from observations; Second column: Results from Model *sFe-dust*; Third column: Model *sFe-all*; Fourth column: *cFe-dust*; Final column: Model *cFe-all*. Model output (annual mean) is objectively mapped onto the cruise track.

then organized grid points that have similar fluxes dominating the local dFe budget into the same cluster (Figure 5.2aceg). Clusters with similar budget structures were further categorized into four cluster groups for the simplicity of presentation. The remarkable aspect of this algorithm is that the Fe budget clusters exhibited organized spatial structure even though the algorithm only analyzed the dFe budget terms without any geographic information (Figure 5.2). In Model *cFe-All* (Figure 5.2gh), which showed the most realistic dFe pattern, the first 22 clusters collectively covered more than 95% of the global ocean and generally fell into three types of dFe balance. The first cluster group (Clusters 1 - 3, 60% surface area) was the low Fe flux region covering the vast areas of the Southern Ocean, subtropical gyres, and most of the Pacific Ocean. In the second and third cluster groups (Clusters 4 - 15, 30% surface area), the dFe source was dominated by shelf sediments and/or remineralization, which were balanced by the scavenging loss. For this model, remineralization included both the biological release of Fe from organic particles as well as desorption. Finally, the higher order clusters (Group 4: Clusters 15 - 22, 5% surface area) were dominated by a significant amount of dFe inputs from dust and sediments, which is a

typical feature in regions along the coastline or under the high dust plume. Large dFe inputs from dust and sediments were balanced by the enhanced scavenging in these regions. Scavenged dFe can be released back to the water column via remineralization and desorption from sinking particles, thus effectively transporting dFe vertically downward and was the key to sustain the subsurface maximum of dFe.

In contrast, Model *sFe-dust* (and *sFe-all*) exhibited a fundamentally different Fe balance with the tightly couple of biological uptake and remineralization, which is somewhat similar to that of macro-nutrient (Figure 5.2ab and Figure 5.2cd). For these two models, remineralization dFe flux only included the biological release of Fe from organic particles but not the Fe desorption. In Model *sFe-dust*, the first 28 clusters covered $\sim$ 95% of the area, and they were also categorized into four groups. The first cluster group (Clusters 1 - 7, 51% surface area) was characterized by very low dFe fluxes, mostly in the oligotrophic subtropical gyres (Figure 5.2ab). The second and third groups (Clusters 8 - 19, 37% surface area) featured a moderate Fe supply via advection and atmospheric deposition, which stimulated biological uptake and remineralization. These groups were in the biologically productive upwelling regions such as the subantarctic region (40°S), eastern tropical Pacific, subpolar North Pacific, and North Atlantic. For the fourth group (Clusters 20 - 28, 7% surface area), atmospheric dust input became dominant, which was balanced by the combination of biological uptake, scavenging, and advective transport. This group fell into regions of the subtropical Atlantic, south western Atlantic, and northern Indian Oceans. With the exception of the fourth cluster group, the biological uptake and remineralization were the two dominant terms for the majority (>88%) of the global oceans in Model *sFe-dust*. This macro-nutrient like balance was modified when the sedimentary Fe source was included in Model *sFe-all* (Figures 5.2cd). However, Models *sFe-dust* and *sFe-all* were similar in the general distribution of cluster groups (Figures 5.2ac) and in structures of the first two groups covering oligotrophic gyres and productive upwelling regions. The large sedimentary dFe fluxes were evident in the third (Clusters 11-18, 15% surface area) and

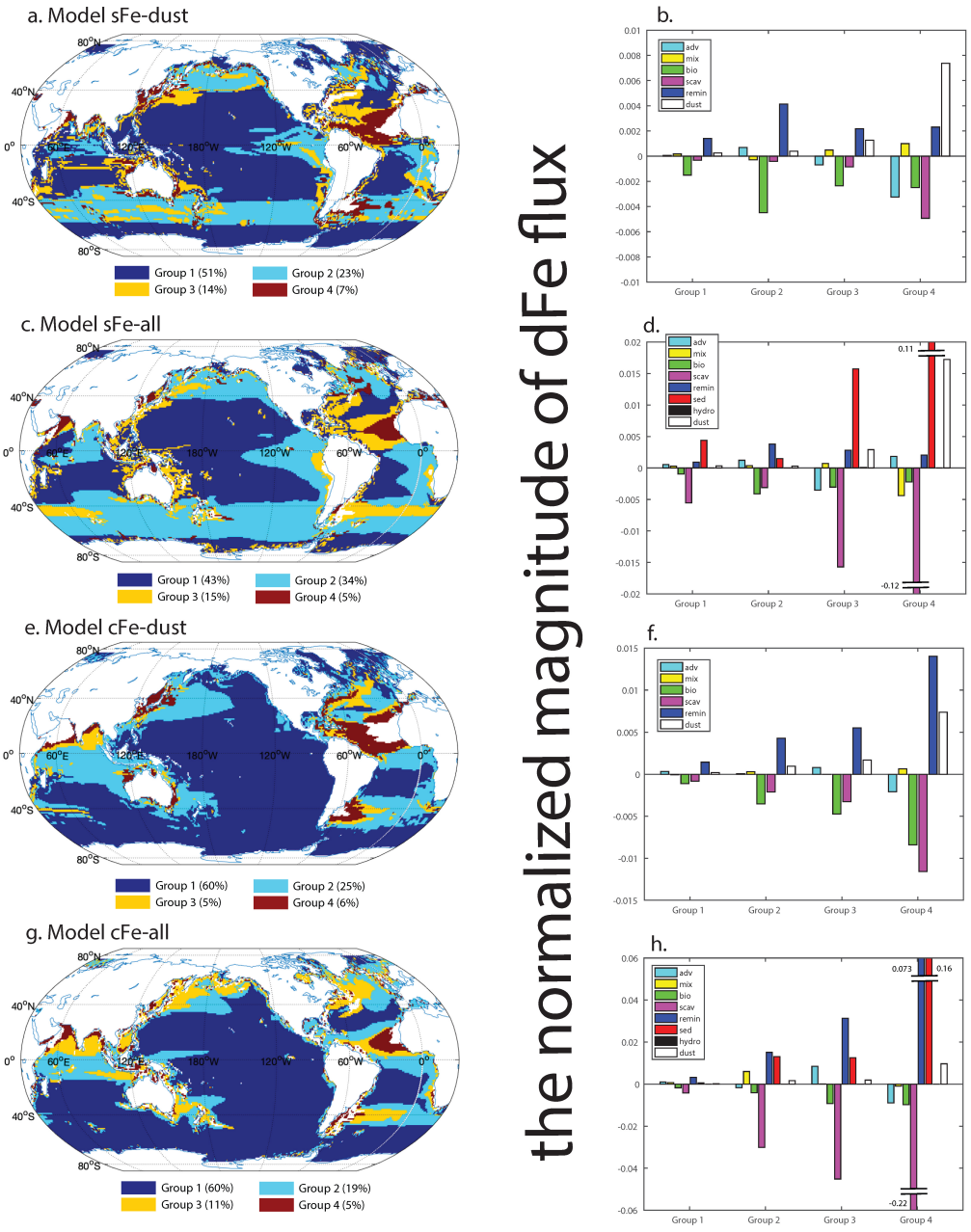

Figure 5.2: K-means clustering of upper ocean Fe budget: (a) Cluster group distribution map for Model *sFe-dust*, (b) the normalized magnitude of dFe flux averaged over each cluster group, (c,d) same for Model *sFe-all*, (e,f) same for Model *cFe-dust*, and (g,h) same for Model *cFe-all*. The budget terms are denoted as adv: advection; dif: mixing; bio: biological uptake; scav: scavenging; remin: remineralization including desorption, sed: sedimentary input, hydro: hydrothermal input, and dust: atmospheric soluble dust deposition.

fourth (Clusters 19-25, 5% surface area) groups of Model *sFe-all*, which were balanced by the enhanced scavenging. Even when all major dFe sources were considered, Model *sFe-all* could not produce a realistic pattern of dFe (Figures 5.1 and 5.3). Rather, it produced broadly uniform dFe pattern that underestimated the subsurface dFe maximum. This uniform dFe pattern demonstrates the importance of a proper parameterization for internal Fe transformations.

Model *cFe-dust* exhibited the lowest dFe concentrations among all the models, but its parameterization for the internal Fe processing was identical to Model *cFe-all* , and their cluster groups showed similar features (Figure 5.2eg). The majority of the surface ocean area was dominated by low dFe fluxes ($\sim$ 70%). As the atmospheric input increased from cluster group 1 to 4, scavenging and remineralization fluxes both increased (Figure 5.2f). These mechanisms worked together to transport dFe downward and formed the subsurface maximum in the thermocline. However, Model *cFe-dust* received a much weaker external Fe input, therefore the magnitude of the budget terms as well as the interior dFe concentrations were low (Figure 5.2f).

The dFe gradient between the surface and subsurface waters in high dust regions was successfully captured by Model *cFe-all*. The key factor behind this success is in the more detailed description of interior ocean processes including variation in ligand binding strength and concentration as well as more sophisticated scavenging parameterization. Atmospheric dust deposits a significant amount of dFe into the surface ocean of the subtropical Atlantic, south western Atlantic, and northern Indian Oceans. In Model *sFe-dust* or *sFe-all*, scavenging rate increased to keep the dFe budget in balance, but it could not deplete the surface dFe due to a low concentration of organic particles in these oligotrophic regions and the dFe protection by a uniformly distributed and strong ligand class (Figure 5.2). This ineffective scavenging loss caused an elevated surface dFe concentration (Figure 5.1). In contrast, Model *cFe-dust* or *cFe-all* included the scavenging onto lithogenic particles and allowed spatial variation in the ligand binding strength and concentration.

These parameterizations led to a more complete depletion of surface dFe under the high dust plume in oligotrophic regions where low biological activity caused a low concentration of the strong-binding ligand class. Furthermore, Model *sFe-dust* or *sFe-all* considered scavenging as the ultimate sink of dFe, thereby removing the dust-deposited dFe out of the water column. Model *cFe-dust* or *cFe-all* allowed the desorption and remineralization of scavenged Fe from particles along the sinking pathway, thus transporting the dust-deposited dFe downward and redistributing dFe in the upper ocean. This internal transformation of Fe makes the ocean dFe cycling distinct from macronutrient cycles.

5.4 Conclusion

The ocean cycling of Fe is regulated by complex interactions between external inputs and internal cycling processes (Tagliabue et al., 2017). Isolating the relative contribution from each process is challenging but is necessary to formulate a biogeochemistry modeling system that correctly simulates the impacts of anthropogenic perturbation and physical climate variabilities (Hutchins and Boyd, 2016). Recently, measurements of the stable isotope ratios of dFe (δ^{56}Fe) have been used to quantify the contribution of external dFe fluxes based on the unique δ^{56}Fe signature of each source (Conway et al., 2019, 2018; Fitzsimmons et al., 2016). These observational studies may motivate modeling community to include the stable Fe isotope in ocean models. In addition, ventilation-based framework (Tagliabue et al., 2014c) can be applied to track various Fe processes along potential density surfaces. Together with these efforts, machine learning algorithms can be applied to uncover previously unnoticed patterns from the volume of observational and/or model-generated data. If effectively applied and interpreted, these new tools can reveal key processes and mechanisms that can be linked to explain specific interactions of processes and tracer budgets. While there are large uncertainties in the magnitude of continental shelf fluxes, our analysis showed that the dFe spatial pattern depends largely on the parameterization of oceanic Fe processing rather than specifications of external sources. The interplay among these interior

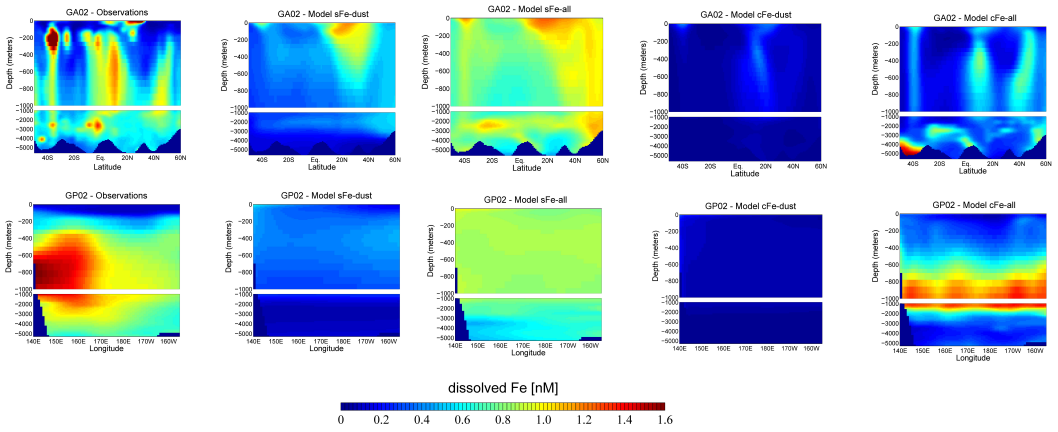

Figure 5.3: dFe distribution along the GEOTRACES transect GA02 (top) and GP02 (bottom). From left to right: First column: measurements from observations; Second column: Results from Model *sFe-dust*; Third column: Model *sFe-all*; Fourth column: *cFe-dust*; Final column: Model *cFe-all*. Model output (annual mean) is objectively mapped onto the cruise track.

ocean processes makes the Fe cycling distinct from that of macronutrients. Thus, without an appropriate representation of these processes, ocean Fe models cannot fully capture the observed Fe distributions. Given the crucial role of these internal dFe transformations, I speculate that their sensitivity to future changes under human impacts will have important consequences to the ocean biogeochemical cycle.

CHAPTER 6

ANTHROPOGENIC IRON DEPOSITION ALTERS THE ECOSYSTEM AND CARBON BALANCE OF THE INDIAN OCEAN

Manuscript in preparation as

Pham, A.L.D. and T. Ito, (2019) Anthropogenic iron deposition alters the ecosystem and carbon balance of the Indian Ocean

Abstract

Phytoplankton growth in the Indian Ocean is generally limited by macronutrients (N, P) in the north and by micronutrient (Fe) in the south. Increasing atmospheric deposition of N and Fe to the open ocean due to human activities can lead to significant responses from both the northern and southern Indian Ocean ecosystems. Previous modeling studies investigated the impacts of anthropogenic nutrient deposition from the atmosphere to the open ocean, but the modeled responses are uncertain due to incomplete representation of the Fe cycling. This study uses a state-of-the-art ocean ecosystem and Fe cycling model to evaluate the sensitivity of ocean productivity and carbon uptake in the Indian Ocean. The model includes three major Fe sources and represents internal Fe cycling modulated by scavenging, desorption, and complexation with multiple, spatially varying ligand classes. A suite of equilibrium sensitivity simulations shows that increased Fe deposition stimulates diatoms productivity in the southern Indian Ocean poleward of 40°S. Anthropogenic N flux has a relatively minor impact. Diatoms production weakens around 40°S due to the P limitation, and diatom are outcompeted there by coccolithophores, which have a lower P demand. These changes in diatoms and coccolithophores production alter the balance between the organic and carbonate pumps in the region, increasing the carbon uptake poleward of 40°S and decreasing it in the equatorward. Our results reveal the important role of ecosystem dynamics in controlling the sensitivity of carbon fluxes in the Indian Ocean

under the impact of anthropogenic nutrient pollution.

6.1 Introduction

The Indian Ocean accounts for around one-fifth of the ocean net primary production (Behrenfeld and Falkowski, 1997) and contains two of the largest O_2 minimum zones (OMZs) of the world oceans in the northern part (the Arabian Sea and the Bay of Bengal) (Stramma et al., 2010). In these two regions, phytoplankton growth is generally limited by macronutrients because of the relatively shallow mixed layer and the Ekman downwelling that transports nutrients away from the euphotic layer. Furthermore, the low O_2 waters in the OMZs promote nitrogen (N) loss through denitrification (Moore et al., 2013; Wang et al., 2019). The concentration of micronutrient Fe is relatively high in the northern Indian Ocean ($\sim$ 1.6 - 2nM) due to relatively high Fe inputs from atmospheric deposition and reduced sediments over the continental shelves (Nishioka et al., 2013). However, Fe can still be a limiting factor for the nitrogen-fixer diazotrophs, which have a higher demand for Fe than other phytoplankton (Moore et al., 2013). In contrast, the southern part of the Indian Ocean shows a very low dFe concentration ($\sim$ 0.2 nM), indicating that biological productivity in this region can be Fe-limited (Nishioka et al., 2013). These contrasting biogeochemical regimes between different parts of the Indian Ocean imply a diverse and complex response of the marine ecosystem to perturbations. Atmospheric deposition of N and Fe in the Indian Ocean has been increasing due to human activities including burning of fossil fuels, agriculture, and land use changes (Baker et al., 2017; Duce et al., 2008; Mahowald et al., 2009). Human activities also emit anthropogenic aerosols, which modify mobilization processes and atmospheric processing. Atmospheric dust deposition, which is generally stronger in the northern Indian Ocean, provides a direct input of bioavailable N, potentially relieving the macronutrient limitation. Increased atmospheric dFe deposition can also stimulate diazotroph production, and the deposited dFe can be transported to the southern Indian Ocean via the long-range ocean transport where photosynthesis is limited by the availabil-

ity of dFe (Boyd and Tagliabue, 2015). In general, a significant response of the Indian Ocean ecosystem to anthropogenic deposition from the atmosphere is expected, including a higher organic carbon export flux, stronger O_2 demand, and thus an expansion of OMZs.

Recent modeling studies have examined the impact of anthropogenic nutrient deposition from the atmosphere into the ocean by driving ocean biogeochemistry models with atmospheric deposition fields derived from atmospheric chemical transport models (Guieu et al., 2019; Ito et al., 2016; Krishnamurthy et al., 2009, 2007). These studies concluded that increasing Fe and N inputs stimulate marine nitrogen fixation in the subtropical North and South Pacific, enhance primary production and export in HNLC regions (Krishnamurthy et al., 2009), and accelerate O_2 consumption in the tropical Pacific Ocean (Ito et al., 2016). Concurrently, the data coverage of dFe and other trace metal species expanded significantly thanks to the GEOTRACES program (Mawji et al., 2015; Schlitzer et al., 2018). The new observations revealed shortcomings of the earlier generations of the Fe cycling models, which did not include all of the dFe sources such as hydrothermal vents. Also, earlier models typically assumed a single ligand class with a uniform distribution. Thus, results from these earlier studies can contain significant uncertainty (Tagliabue et al., 2016). Significant model biases have been identified relative to the observed pattern of dFe revealed by the recent GEOTRACES observations (Mawji et al., 2015; Schlitzer et al., 2018). Models with constant ligand concentrations may underestimate the feedback between biological activity, ligand production, and dFe concentration to environmental changes (Völker and Tagliabue, 2015). Furthermore, impacts of anthropogenic deposition on the Indian Ocean, where the nutrient cycling is complex and the phytoplankton community is diverse, has not been examined thoroughly and systematically.

This chapter aims to investigate the impact of increasing anthropogenic atmospheric N and dFe deposition on nutrient distribution, phytoplankton productivity, and carbon uptake of the Indian Ocean. To this end, I use an ocean ecosystem model, which represents major phytoplankton types (Dutkiewicz et al., 2014), coupled with a recently improved

Fe cycling scheme (Pham and Ito, 2018; Pham and Ito, 2019). The Fe scheme includes many crucial processes controlling the ocean Fe cycling and demonstrated improvements in the representation of dFe distribution as observed by the GEOTRACES cruises. The ecosystem model has been used in several previous studies that examined the ocean biogeochemistry response to human perturbations (Dutkiewicz et al., 2013, 2014) and the interplay between different bigeochemical processes shaping the phytoplankton community structure (Dutkiewicz et al., 2012). Atmospheric deposition of dFe and N is derived from the three-dimensional atmospheric chemical transport model GEOS-Chem coupled with a comprehensive dust-Fe dissolution scheme (Ito et al., 2016; Johnson and Meskhidze, 2013). The rest of this chapter is organized as follows. In section 2, we describe the model configuration and the experimental design. In section 3, we present results of sensitivity experiments. In section 4, we summarize and discuss the implication of these results.

6.2 Model configuration and experimental design

The ocean model used in this study is based on the Massachusetts Institute of Technology general circulation model (Marshall et al., 1997a,b, MITgcm) with a biogeochemistry and ecosystem component (Dutkiewicz et al., 2012, 2014). The model domain is configured for a 2.8°x 2.8°horizontal grid spacing and 23 vertical z-levels with grid spacing ranging from 10 m in the surface to 500 m at 5000 m. Ocean boundary layer physics is parameterized using the K-Profile Parameterization scheme (Large et al., 1994), and the effects of mesoscale eddies is parameterized using the isopycnal tracer and thickness diffusion scheme (Gent and McWilliams, 1990). The physical ocean circulation is forced by climatological wind and buoyancy forcing derived from the National Center for Environmental Prediction Reanalysis product (Kalnay et al., 1996).

The biogeochemical component of the model is based on Dutkiewicz et al., (2014) including the cycling of C, P, N, Si, Fe and O_2 through inorganic, living, dissolved, and particulate organic phases. Two grazers and six phytoplankton types (diatoms, coccol-

ithophores, large eukaryotes, *prochlorococcus*, other pico-phytoplankton, and diazotrophs) are represented in the model. The phytoplankton growth rate is a function of the Chlorophyll: C ratio, temperature, light, and nutrient availability, following Hickman et al., (2010) and Geider et al., (1998).

The refined Fe scheme encompasses important processes in the ocean Fe cycling including multiple sources and internal cycling of Fe such as scavenging onto and release from lithogenic and organic particles and dFe retention by spatially varying ligands. Details on the Fe cycling model and its capability to reproduce observations were documented in Chapters 2, 3, and 4 (Pham and Ito, 2018; Pham and Ito, 2019). Atmospheric deposition fields of N and dFe were taken from the output of atmospheric chemical transport model GEOS-Chem (Johnson and Meskhidze, 2013). Anthropogenic effects on N and dFe deposition were calculated using the emission inventories for the year 2009, and the pre-industrial fluxes were calculated by turning off all anthropogenic emission sources. Details on this model and on how the industrial fluxes were calculated based on anthropogenic emission were described in Ito et al., (2016) and Johnson and Meskhidze, (2013).

The model was first spun up under the pre-industrial deposition of N and dFe for 1,000 years (*PreIn* run). Initialized from the last time step of the *PreIn* run, three additional integrations were performed using the anthropogenic deposition of N and Fe separately and together. The model was further integrated for 1,000 years to achieve new quasi-steady states, and the equilibrium response of the ecosystem and carbon cycle was then analyzed. These experiments were intended to examine and isolate the impacts of anthropogenic N and Fe deposition on the Indian Ocean. In reality, a variety of transient perturbations to the marine ecosystem and its biogeochemistry exists, including warming and increased stratification, circulation changes, riverine nutrient input, and acidification. Account for all these changes are beyond the scope of this paper. Rather, we focus on the equilibrium response to a single perturbation. In summary, the model experiments were set up as follows:

- "*PreIn*" run forced by the pre-industrial atmospheric Fe and N deposition fields

- "*Ind*" run forced by the contemporary atmospheric Fe and N deposition fields
- "*Pre-Fe*" run forced by the contemporary atmospheric N deposition field and pre-industrial condition for Fe
- "*Pre-N*" run forced by the contemporary atmospheric Fe deposition field and pre-industrial condition for N

Results of these model runs were analyzed by comparing the differences in nutrient fields, biological productivity, phytoplankton community structure, and carbon uptake, all in relation to the *PreIn* run.

6.3 Results

6.3.1 Model validation

We first evaluated the model performance and its ability to reproduce major biogeochemical features of the Indian Ocean by comparing the observed, modern distributions of nutrient tracers with the *Ind* run forced by the contemporary forcings.

First, we evaluated the model NO_3^- distribution using the World Ocean Atlas (Garcia et al., 2014) as the observational benchmark (Figure 6.1). The model reproduced the general pattern of the near-surface NO_3- distribution reasonably well. When compared with the World Ocean Atlas, the model captured the low concentration north of 40°S and high concentration at high latitudes. The model is certainly not perfect as it underestimated the NO_3- concentrations at high latitudes. Next, we examined the meridional transect of dFe along the GEOTRACES line GI04 (Schlitzer et al., 2018) (Figure 6.2), focusing on the upper ocean (0-1000m). dFe in the upper ocean is more important for sustaining biological productivity, which mainly occurs in the euphotic zone. The model captured the pattern of dFe remarkably well especially in the top 1,000m, consistent with results shown by Pham and Ito, (2018). Specifically, it captured the strong meridional gradient of dFe centered at around 10°S where the dFe concentration is high (0.8 - 1.3 nM) in the subsurface water of

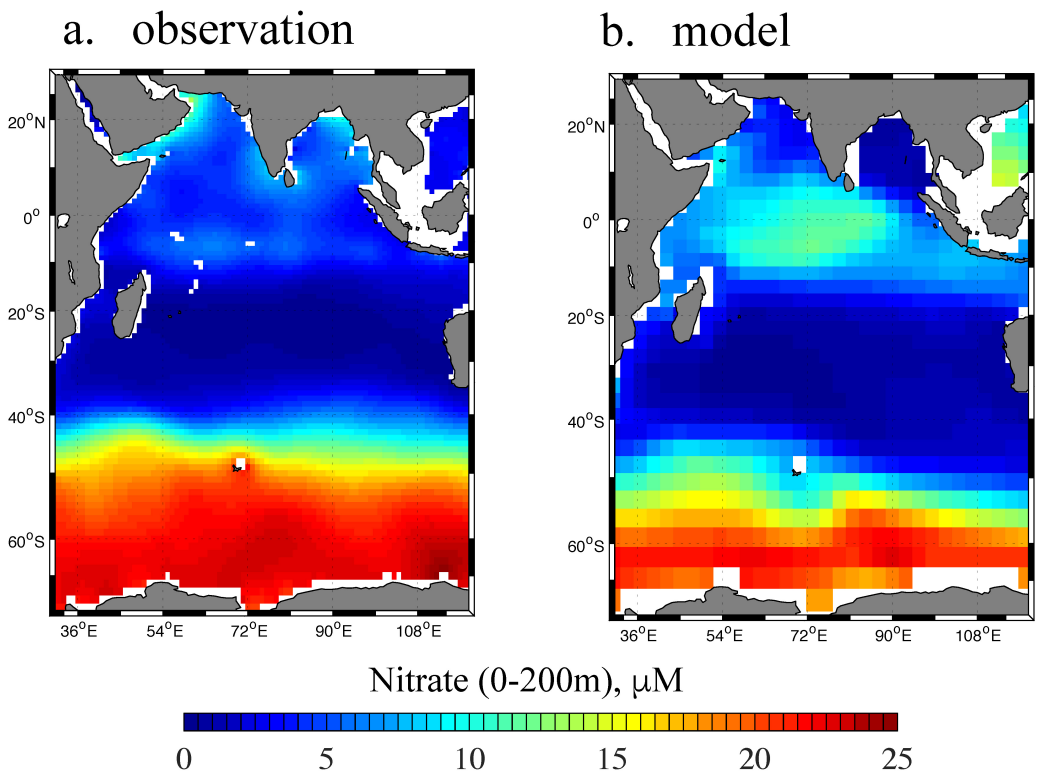

Figure 6.1: Left panel (a): World Ocean Atlas Annual Mean NO_3- averaged over the top 200 m. Right panel (b): results from the *Ind* run

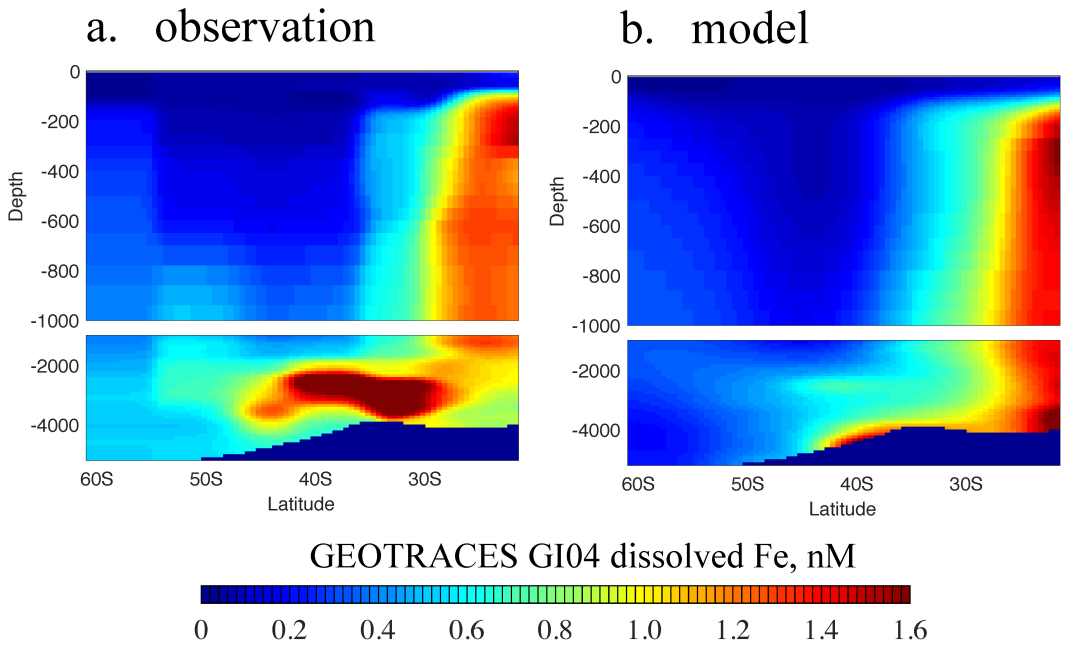

Figure 6.2: Left panel (a): dFe concentration observed along the GEOTRACES Indian Ocean transect GI04. Right panel (b): results from the *Ind* run. The model output is objectively mapped onto the GI04 transect. The top 1,000m is stretched for a better comparison for the upper ocean thermocline.

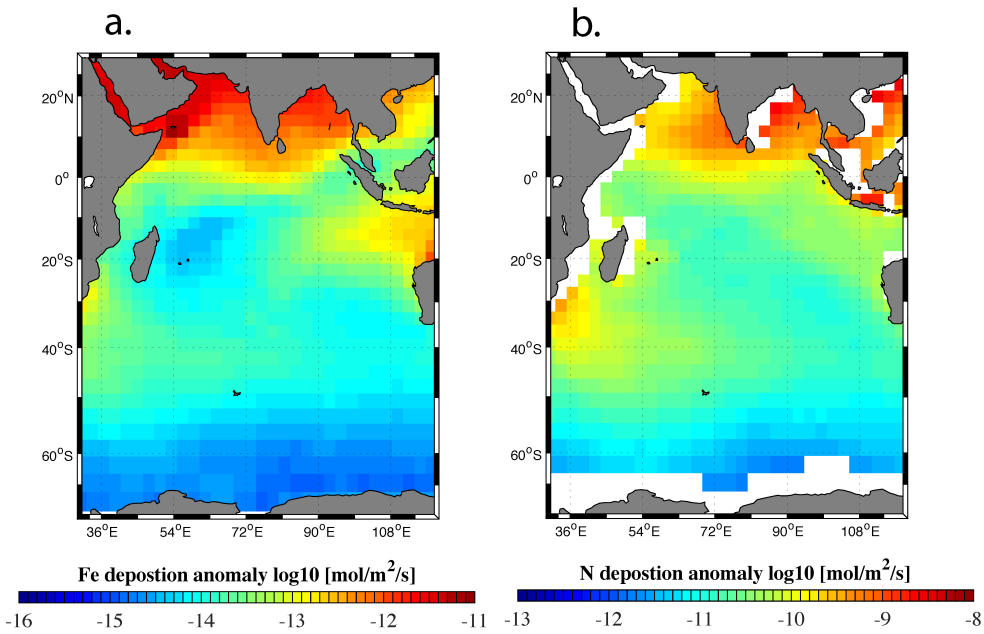

Figure 6.3: Atmospheric deposition anomaly (*Ind* run - *PreIn* run) for (Left, a) dFe and (Right, b) fixed N into the surface of the Indian Ocean used in this study. Note that the value is plotted on a logarithmic scale.

the tropical thermocline but it is very low in the southern part ($\sim$ 0.2 nM). It also reproduced the subsurface peak of dFe in the northern Arabian Sea ($\sim$ 10°N) and the strong vertical gradient in the dFe concentration observed there between the surface (0-200m) and subsurface waters ($>$ 200m). The only major setback of our model is that it cannot reproduce the hydrothermal signal around the Central Indian Ridge segment. Biological productivity is influenced by nutrients distribution, and it is therefore essential that the model captures the nutrient fields well.

6.3.2 Sensitivity experiments

The increase in atmospheric deposition of fixed N and dFe into the Indian Ocean is shown in Figure 6.3. A large increase in the dFe deposition occurred in the coastal regions of the northern Indian Ocean and north of Australia, while it moderately increased over the equatorial and southern regions. Integrating over the Indian Ocean (30°E-110°E, 80°S-30°N),

the dFe flux increased from 38.78 mol/s to 87.78 mol/s, more than doubling the pre-industrial deposition. N deposition exhibited similar spatial patterns to dFe (Figure 6.3b). Again integrating over the Indian Ocean, the fixed N flux increased from $6.3 \cdot 10^3$ mol/s to $1.3 \cdot 10^4$ mol/s, approximately doubling from its pre-industrial value.

Comparing *PreIn* and *Ind* runs, the response of the Fe concentration for the upper 300m was an increase of approximately 0.3nM in the northern Indian Ocean, whereas the response was much weaker in the poleward of 40°S (Figure 6.4a). The pattern was generally similar to the atmospheric deposition of Fe where the northern Indian Ocean received more anthropogenic Fe deposition relative to the Southern Ocean by several orders of magnitude. In contrast, the response of the near-surface NO_3- (Figure 6.4b) was very different from the atmospheric deposition pattern (Figure 6.3b). NO_3- concentration decreased in the upper 300m water of the Indian Ocean even though the ocean received more N from atmospheric deposition. In particular, the N decrease was significant in the subantarctic region between 40°and 60°S. There was also a region of significant N decrease in the eastern tropical Indian Ocean. The northern Bay of Bengal represents one of a few regions where the upper 300m NO_3- concentration increased. This changes in the upper 300m NO_3- concentration implies that the biological N uptake was enhanced in many parts of the Indian Ocean.

Other macro nutrients (P and Si) were also decreasing with distinct patterns (Figure 6.4cd). The P decrease was widespread, but it was more enhanced in the Bay of Bengal and in the subtropics between 20°- 40°S. In contrast, the Si decrease was more focused in the southern high latitudes, the eastern tropics, and the bay of Bengal. The difference between P and Si depletion reflects the regions of strong increase in diatoms productivity. The decline of macronutrients in the southern high latitudes suggests that the increased Fe and N input was altering the productivity there even though the anthropogenic deposition was relatively weak in these region and dFe is always close to be depleted.

In Figure 6.5, we only show changes in two species: diatoms and coccolithophores al-

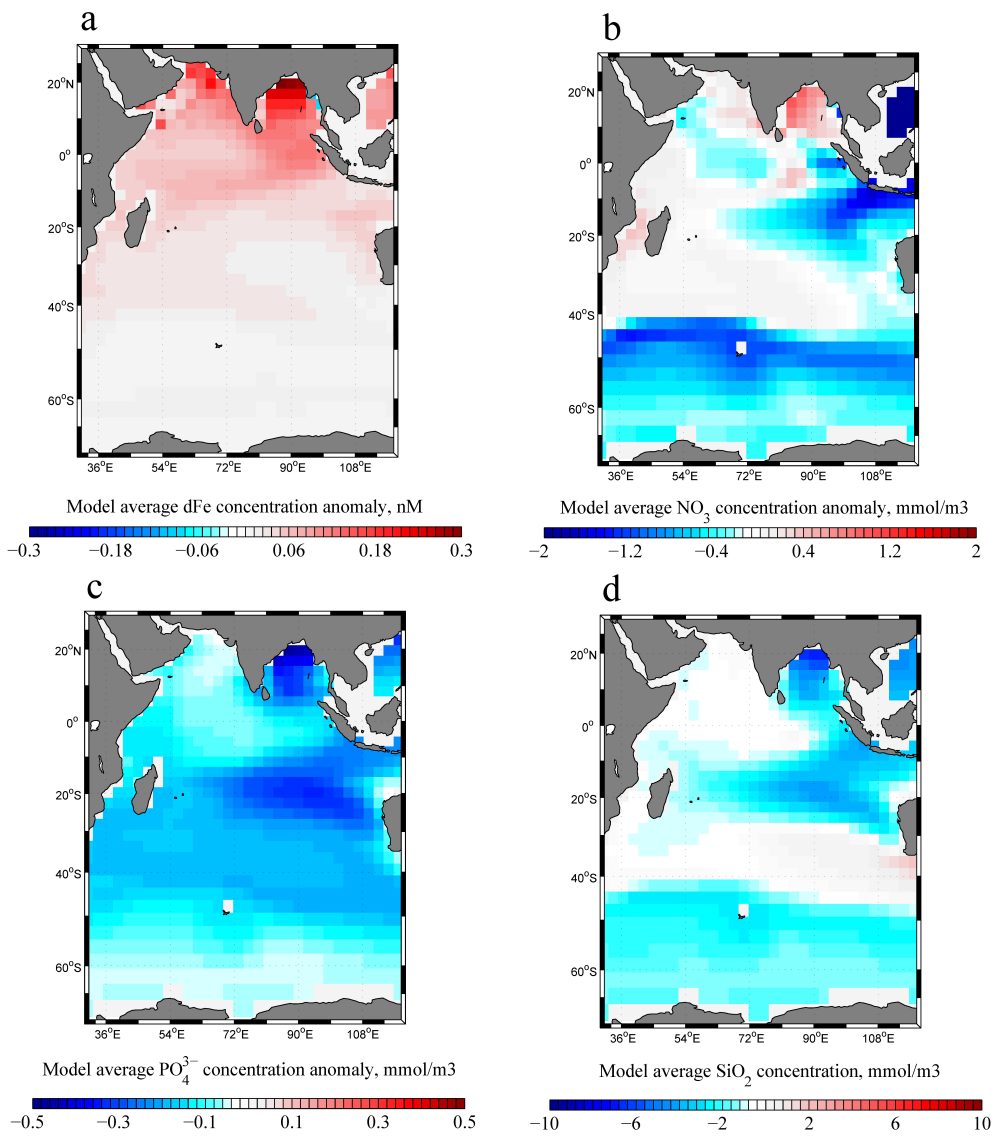

Figure 6.4: Model (*Ind* run) concentration anomaly relative to the *PreIn* run averaged from 0-300m in the Indian Ocean for (a) dFe, (b) NO_3^-, (c) PO_4^{3-} and, (d) silicate.

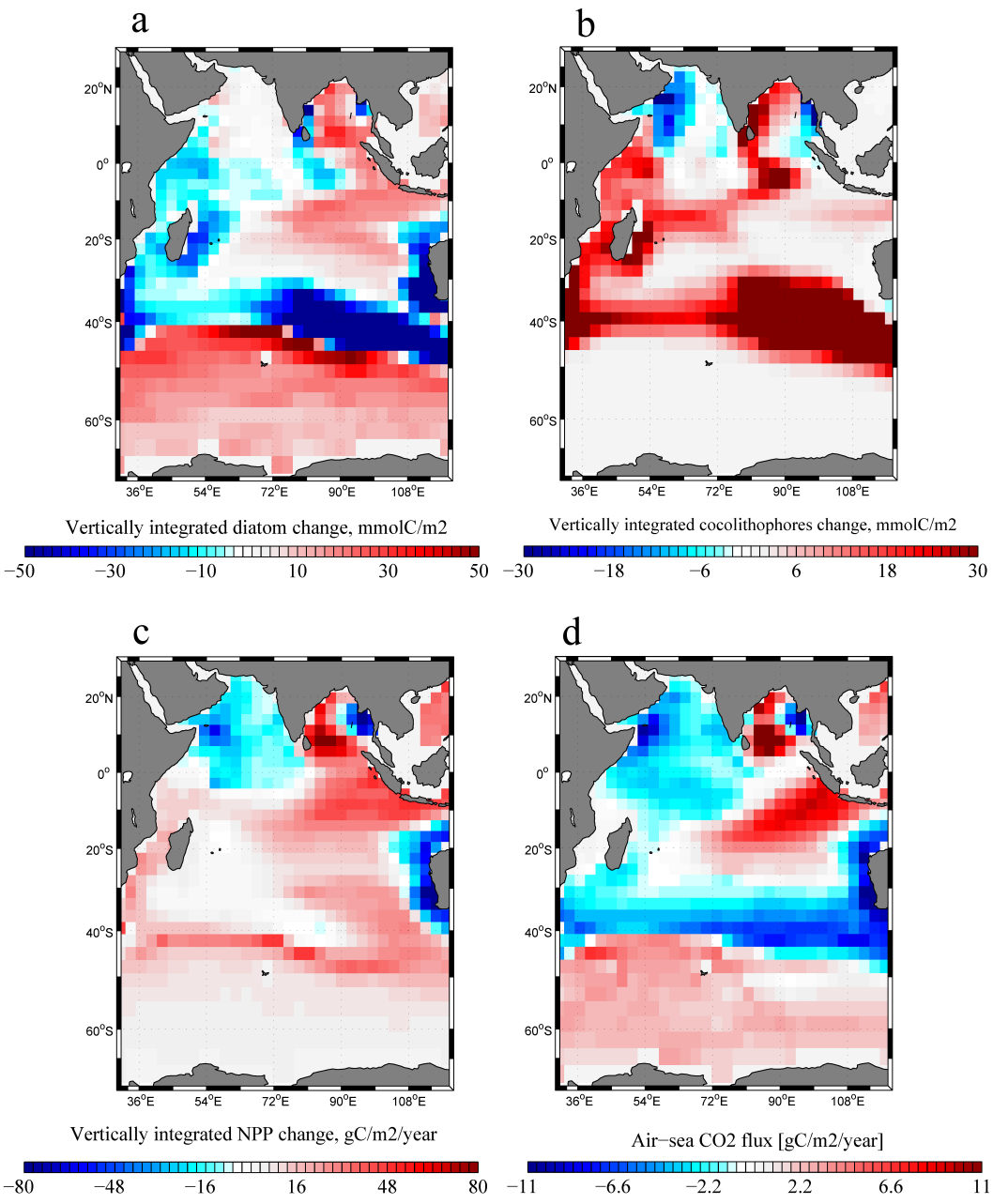

Figure 6.5: Vertically integrated phytoplankton concentration anomaly between the *Ind* and the *PreIn* runs. All phytoplankton biomass is measured in the units of P in the model. (a) diatoms, (b) coccolithophores, (c) primary production, and (d) air-sea CO_2 flux. The air-sea CO_2 flux is positive into the ocean.

though the model includes 6 phytoplankton types. This is because the majority of changes in the total primary production and ocean carbon uptake are explained by changes in diatoms and coccolithophores growth. Figure 6.8 shows changes in the other 4 phytoplankton species for a complete description. Diatoms concentration increased significantly in the south of 40°S, in the Bay of Bengal, and in the eastern tropics (west of Malaysia) which are co-located with the decrease of N, P, and Si in these regions (Figure 6.4). Diatoms are the only phytoplankton type that utilizes Si, therefore the decrease of Si confirms the role played by diatoms in these regions. In contrast, diatoms concentrations weakened along 40°S and in the west of Australia, which coincides with an increase in coccolithophore (Figure 6.5b) and picoplankton abundance (Figure 6.8c). These changes indicate that diatoms were out-competed here by coccolithophores and picoplankton. The reason for these changes is that diatoms have a faster maximum growth rate but require a higher P concentration relative to coccolithophores and picoplankton (Riegman et al., 2000). Thus, the decrease in P supply along 40°S caused diatoms to be less competitive and helped coccolithophores become more dominated. This change caused a shift in the biological carbon pump in this region from organic carbon to calcium carbonate pumps. Moreover, an increase in coccolithophores and decrease in diatoms decreased the surface alkalinity relative to DIC. This decrease in surface alkalinity shifted the carbonate chemistry of this region towards a more acidic condition with a lower pH, leading to an increase in the partial pressure of CO_2 (pCO_2). Consequently, it decreased the rate of ocean CO_2 uptake along 40°S (Figure 6.5d). This is somewhat counter-intuitive because the primary productivity indeed increased along 40°S in the Indian Ocean under the anthropogenic deposition. However, the intensification of the carbonate pump led to a decrease in the regional air-sea CO_2 fluxes. In contrast, the increase in diatoms productivity at southern high latitudes, the Bay of Bengal, and the eastern tropical Indian Ocean contributed to the stronger organic carbon pump, thus increasing the ocean CO_2 uptake (Figure 6.5d).

Turning our attention to the northern Indian Ocean, the increased Fe deposition stim-

ulated the growth of nitrogen-fixer diazotroph in the northern Bay of Bengal (Figure 6.8). Thus, N concentration increased in this region even though there was a significant decrease in P and Si levels (Figure 6.4). In contrast, diazotroph concentration decreased in the Arabian Sea together with diatoms and coccolithophores, likely due to more intense P limitation in this region which ultimately limited phytoplankton growth.

The changes described so far are between *PreIn* run and *Ind* run, in which both anthropogenic effects on Fe and N were considered. However, these changes were mostly caused by the increase in dFe deposition alone, whereas the increase in anthropogenic N deposition only caused a minor effect. This is shown in Figure 6.6 and 6.7 where changes between *Pre-N* and *PreIn* runs were almost the same as changes between *Ind* and *PreIn* runs. In contrast, changes between *Pre-Fe* and *PreIn* runs were relatively small. Thus, further refinement and development of Fe model will likely influence model results of ecosystem changes in this region.

6.4 Discussion and Conclusion

Human activities have heavily perturbed atmospheric deposition of micro-nutrient Fe and macro-nutrient N into the ocean since the start of the industrial era (Mahowald et al., 2009; Mahowald et al., 2017). This perturbation has a crucial consequence to the marine ecosystem especially in regions where phytoplankton growth is limited by the availability of these nutrients, such as the oligotrophic regions limited by N and/or P and the HNLC regions limited by Fe. Earlier modeling studies estimated a modest response of the ocean primary production and air-sea CO_2 exchange to the anthropogenic nutrient deposition at the global scale, but also predicted striking responses of biogeochemical cycles at regional scales (Ito et al., 2016; Krishnamurthy et al., 2009, 2007; Somes et al., 2016). Specifically, Krishnamurthy et al., (2009) suggested that increasing N and Fe inputs stimulate marine nitrogen fixation in the subtropical North and South Pacific where Fe limitation of diazotroph is relieved but decrease diazotroph growth in the Indian Ocean where P becomes limited.

This study focused on the equilibrium response of the Indian Ocean ecosystem and carbon cycle to increased atmospheric nutrient inputs caused by anthropogenic effects on aerosol deposition. We used a state-the-art ocean ecosystem and Fe cycling model, constrained by the new high-quality data of Fe from the the GEOTRACES program (Mawji et al., 2015; Schlitzer et al., 2018). This new dataset puts a much more stringent constraint on the representation of Fe cycling in the ocean biogeochemistry models, thereby improving our process-level understanding and quantification of key processes (Tagliabue et al., 2016; Tagliabue et al., 2017). Our ocean model, when forced under the contemporary deposition (evaluated at year 2009), was able to reproduce many important features of the observed nutrient distribution. Although the model still has some biases in the macronutrient patterns, it captured major aspects of the subsurface dFe pattern along the Indian Ocean GI04 transect remarkably well. Model experiments were designed to examine the impacts of anthropogenic N and Fe deposition to the open ocean, separated from the other anthropogenic and natural drivers, such that we can clearly understand the mechanisms at play. Of course, several different types of perturbations affect marine ecosystems and their biogeochemistry since the industrial revolution, including ocean warming, ocean circulation changes, riverine nutrient input, and acidification due to the uptake of fossil fuel CO_2. Among these perturbations, the anthropogenic nutrient input from rivers can provide a significant mount of N and P to the open ocean (Sharples et al., 2017). Thus, if this input were included in the model, the phytoplankton community in the northern Indian Ocean could be relieved of P-limitation, and therefore could significantly enhance. Nevertheless, a comprehensive analysis of the realistic, transient ecosystem changes is beyond the scope of this chapter. Even in this idealized experiment, the response of ecosystems and the carbon cycle is complex and exhibited unique spatial patterns.

The atmospheric fluxes of N and Fe into the Indian Ocean both doubled their values since the industrial revolution due to anthropogenic effects. However, the increase in primary production summed up over the whole basin increased only moderately ($\sim 6.4\%$, see

Table 6.1). Interestingly, the ocean CO_2 uptake decreased by 18 % if integrated over the Indian Ocean. This decrease can be explained by analyzing changes in the ocean CO_2 uptake pattern and phytoplankton community structure, which did not increase uniformly. In particular, both productivity and carbon uptake intensified in the southern high latitudes and in the eastern tropics. These changes were influenced by increasing diatoms productivity and a stronger organic carbon pump. In contrast, ocean productivity and carbon uptake decreased significantly in other regions. The northwestern part of the Indian Ocean exhibited decreased productivity and weaker carbon uptake due to the intensification of P limitation. An increase in coccolithophores production along 40°S led to a stronger calcium carbonate pump at the expense of diatoms productivity. This caused the ocean carbon uptake to weaken even though the local primary productivity increased. Overall, the regional pattern of changes and responses of the phytoplankton community were much more complicated than changes in the basin-scale primary production and carbon uptake. In our model experiments, an increase Fe deposition represented the main factor that drives biogeochemical changes. The increase in N deposition only played a minor role, which is consistent with results by Guieu et al., (2019), perhaps due to the relatively small magnitude of N deposition in comparison to the upwelling source.

The Indian Ocean is an important region of the world ocean, containing a large volume of low O_2 water in the north where phytoplankton is limited by macronutrient (Stramma et al., 2010) and a HNLC region in the southern sector where biological productivity is limited by Fe (Twining et al., 2019). This diverse and complex region is vulnerable to an increase in atmospheric inputs of N and Fe due to industrial activities (Baker et al., 2017; Duce et al., 2008; Mahowald et al., 2009). Our results suggested that anthropogenic aerosol inputs may slightly increase basin-scale primary productivity but may cause significant changes in the pattern of productivity and the composition of the community structure. The latter change can alter the functioning of the biological carbon pumps with non-negligible impacts on the basin-scale carbon uptake. Previous studies have pointed to an increase in coccolithophores

Table 6.1: The total primary production (PP) and air-sea CO_2 flux (positive values mean the ocean uptakes CO_2) over the Indian Ocean 30°E-110°E, 80°S-30°N

Model run	PP (PgC/year)	air-sea CO_2 flux (gC/year)
PreIn	6.36	0.13
Pre-Fe	6.39	0.14
Pre-N	6.77	0.11
Ind	6.77	0.11

under global warming and an increasing CO_2 concentration with important consequences to the ocean calcification and global carbon cycle (Krumhardt et al., 2016, 2019; Krumhardt et al., 2017a,b). We further emphasized the crucial role of this calcifier phytoplankton due to its sensitivity to nutrient inputs. In conclusion, our results suggested a complicated and strong sensitivity of the ecosystem and carbon fluxes near the water mass boundaries of the southern Indian Ocean under the impact of anthropogenic pollution.

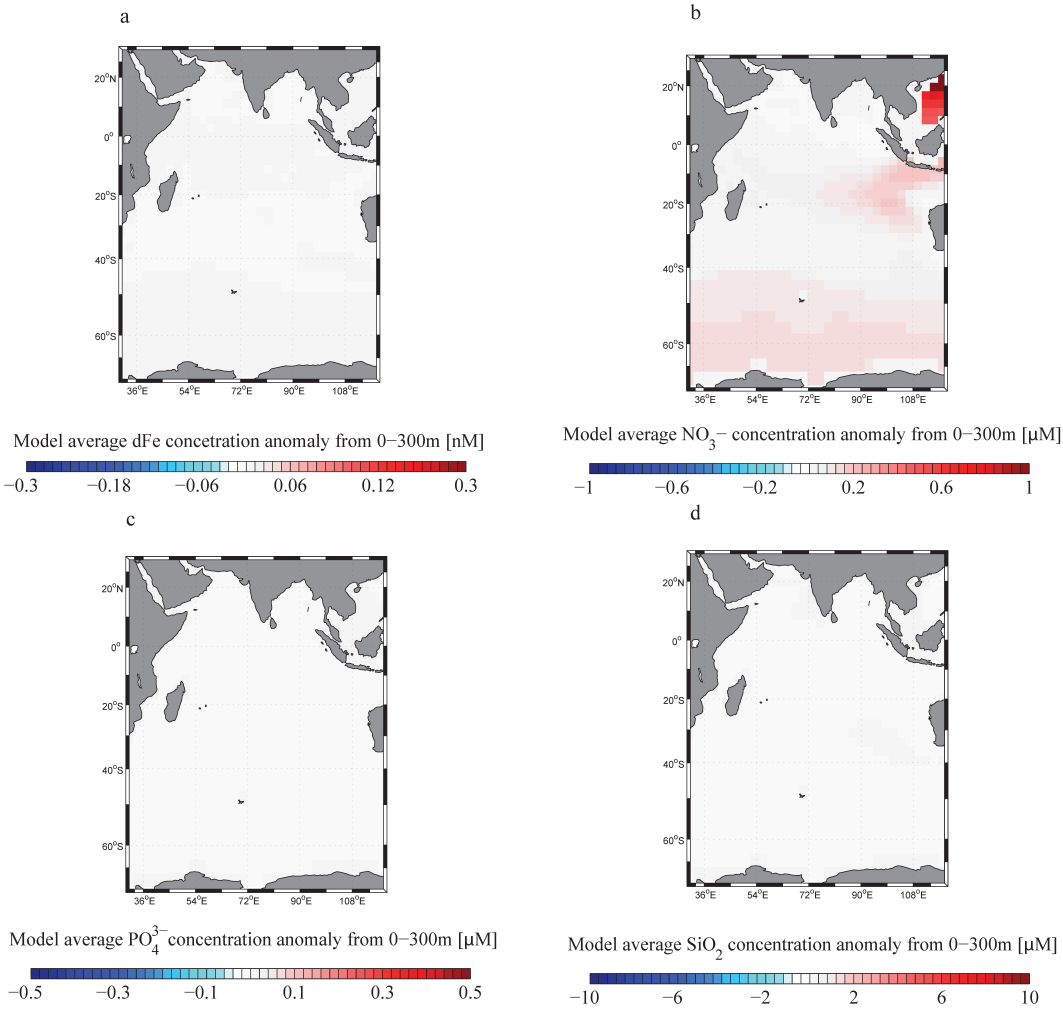

Figure 6.6: Model (*Pre-Fe* run) concentration anomaly relative to the *PreIn* run averaged from 0-300m in the Indian Ocean for dFe (a), NO_3^- (b), PO_4^{3-} (c), and silicate(d)

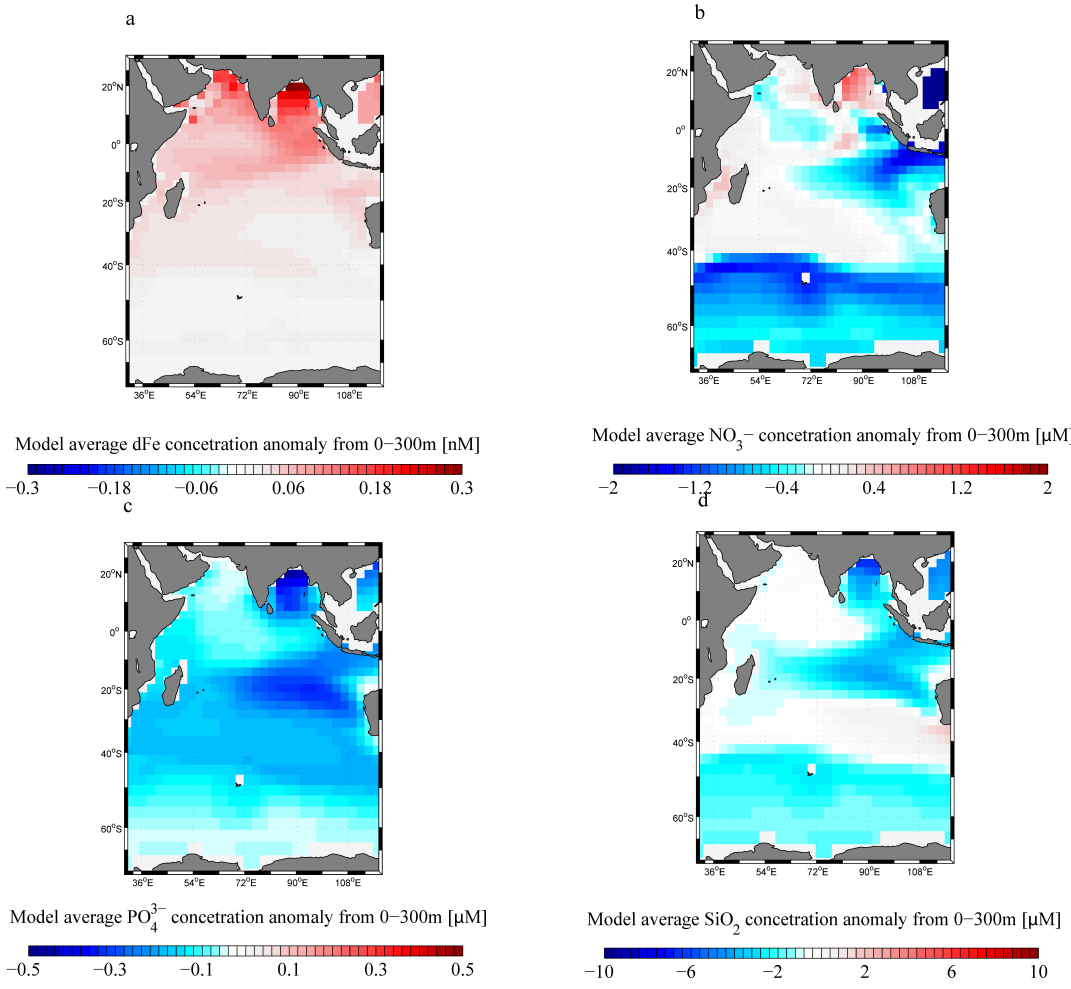

Figure 6.7: Model (*Pre-N* run) concentration anomaly relative to the *PreIn* run averaged from 0-300m in the Indian Ocean for dFe (a), NO_3^- (b), PO_4^{3-} (c), and silicate(d)

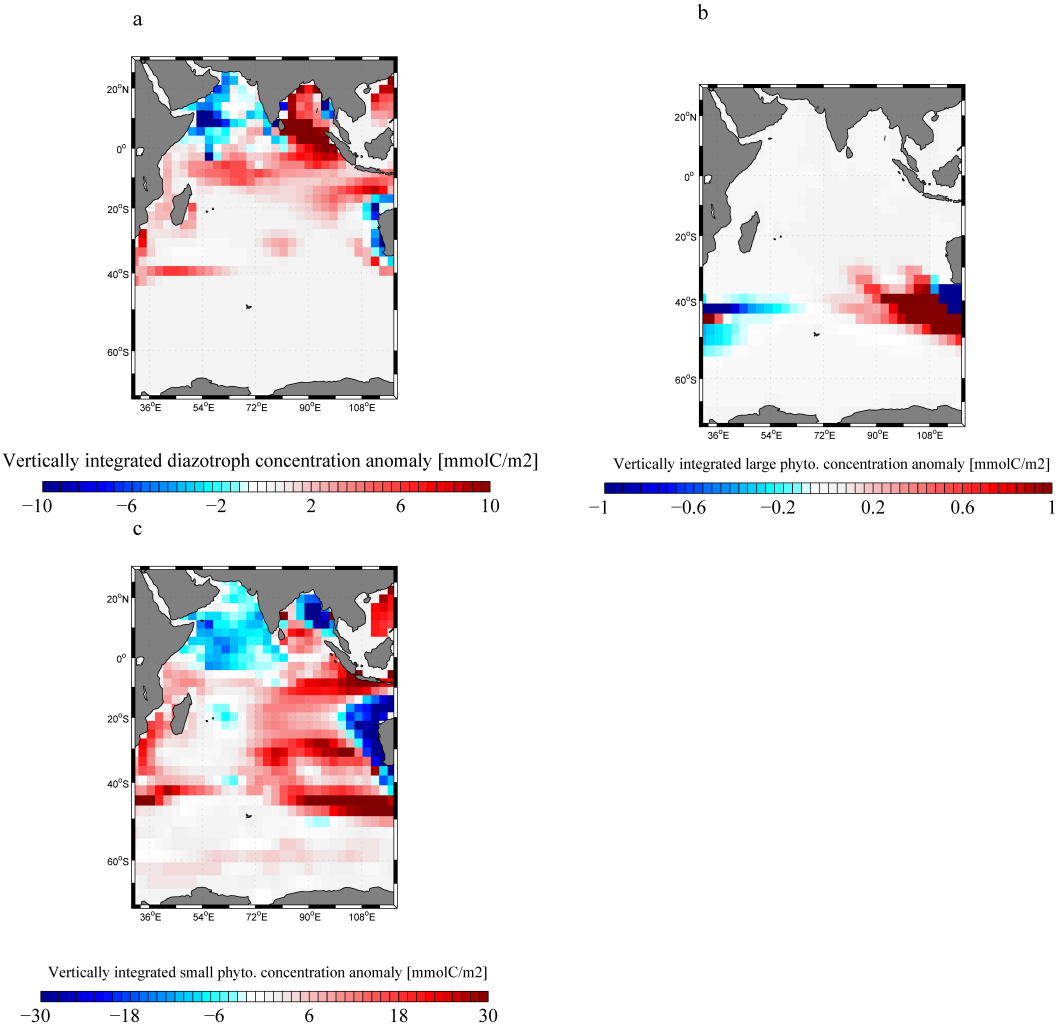

Figure 6.8: Model (*Ind* run) vertically integrated concentration anomaly relative to the *PreIn* run for diazotroph (a), large phytoplankton (b), and picophytoplankton (c)

CHAPTER 7

CONCLUSION AND RECOMMENDATIONS FOR FUTURE STUDIES

This dissertation aimed to understand mechanisms controlling the upper (0-1000m) ocean dFe distribution revealed by the GEOTRACES program and evaluate the impact of increasing anthropogenic atmospheric dFe deposition on the ocean ecosystem and carbon balance. In this chapter, I summarize the main results of this dissertation and discuss their implications as well as important remaining questions for future work.

7.1 What controls the dFe pattern in the ocean thermocline?

The GEOTRACES program has greatly increased our ocean Fe dataset, providing a unique opportunity to further our understanding of the Fe cycling and improve Fe models. In chapter 2, taking advantage of the new GEOTRACES dataset, I significantly improved the Fe parameterization in an OGCBM (MITgcm), which still applied many traditional approaches and assumptions to represent the ocean Fe cycling. The improved Fe parameterization includes all three major sources of dFe and represents the internal Fe transformation modulated by scavenging, desorption and remineralization, and binding with multiple, spatially varying ligand classes.

A prominent feature of GEOTRACES observations is the existence of local dFe concentration maxima at the depths of the main thermocline (300-1,000m) in various ocean transects. These subsurface dFe maxima can be an important source of dFe to marine phytoplankton in the euphotic layer through upwelling and vertical exchange processes, especially for the Fe-limited upwelling regions (Tagliabue et al., 2014a). However, comparison between these new GEOTRACES data and the current Fe models showed significant biases in model representation of these subsurface maxima, indicating our incomplete understanding of the key Fe processes.

These thermocline dFe maxima can be formed by dFe supplies from external sources (Resing et al., 2015) such as atmospheric deposition, continental shelves, and hydrothermal vents or by the release of dFe from particles (Boyd et al., 2010). After being released from the sources, dFe needs to be protected from scavenging removal by binding with organic ligands (Gledhill and Buck, 2012). Thus, the formation and maintenance of the subsurface dFe maxima is likely a phenomenon involving multiple processes.

In chapter 3, I explored the mechanism behind the subsurface dFe maxima through a suite of simulations in an ocean biogeochemistry model with a much improved Fe cycling scheme. Results from the model simulations showed that the subsurface dFe maxima observed in different ocean basins are formed by different mechanisms. In high-dust regions such as the subtropical Atlantic and northern Indian Oceans, the dust-deposited Fe is mostly scavenged onto particles, which then sink and release Fe in the thermocline through remineralization and desorption, enhancing the subsurface dFe concentration. In contrast, in regions where dust deposition is low such as the Pacific Ocean, dFe sources from continental shelves and hydrothermal vents are found to be important. For all these regions, subsurface ligands produced by particle remineralization process retain dFe released from the sources, thus play a central role in the maintenance of the subsurface maxima in our model.

Another unique feature of the ocean dFe pattern revealed by the GEOTRACES program is the low-surface-high-subsurface dFe concentrations under the dust plume in the subtropical Atlantic (Hatta et al., 2015). Many state-of-the-art ocean Fe models compiled in Tagliabue et al., (2016) overestimated the surface and underestimated the subsurface dFe features. These model biases indicate problems in the model representation of Fe scavenging process or the Fe biological uptake or the Fe retention by ligands. Recent modeling studies by Pagnone et al., (2019) and Ye and Völker, (2017) argued for a stronger scavenging rate by dust-deposited particles in this region; however, the efficiency of this mechanism depends on the dFe protection of organic ligands. In chapter 4, I explained the

observed features and model biases in the subtropical North Atlantic by sensitivity simulations in my improved Fe model. In these simulations, I respectively altered the model parameterization for scavenging, biological uptake, and ligand to quantify the role of each process. I suggested that biases of the models compiled by Tagliabue et al., (2016) are largely due to their representation of a single, relatively strong ligand class. Scavenging cannot effectively remove the dust-deposited Fe when it is outcompeted by ligand protection. The representation of a weaker ligand class in the model allows dust-deposited dFe to be effectively removed from the surface by scavenging and be released to the subsurface water through desorption and remineralization. I argued for the inclusion of multiple ligand classes with various binding strength in Fe models rather than a traditional approach of assuming only one ligand.

Although the rapidly expanding GEOTRACES data has transformed our understanding of Fe cycling by revealing the key role of dFe inputs from bottom sediments and hydrothermal vents, relative contributions from these external sources versus internal ocean processes are still poorly constrained. I addressed this issue in chapter 5 by analyzing the simulated dFe distribution fields and budgets in different ocean Fe models using an unsupervised classification method. These Fe models differed in their representations of the external dFe sources and oceanic dFe processing. The classification method identified Fe regimes in these ocean models based on how the simulated dFe budget was balanced in different ocean regions. My analysis suggested that the upper ocean dFe patterns are largely controlled by the interaction between internal transformation processes: dFe scavenging by particles, dFe release by desorption and remineralization, and dFe retention by ligands. Even though external sources are important in setting the overall magnitude of the ocean dFe concentration, ocean models cannot explain observations without a proper representation of the internal processes. Moreover, distinct dFe regimes emerged from my analysis demonstrated a complex picture for the ocean Fe dynamics, not just a simple coupling to the cycling of major macronutrients.

Despite the progress made in this work, challenges remain. My current Fe model still shows biases when compared with GEOTRACES observations. For instance, the model significantly underestimated the hydrothermal dFe signals in the deep ocean along the subtropical Atlantic GA03 and the Indian Ocean GI04 transects. In addition, it cannot correctly capture the magnitude and extension of several subsurface dFe maxima observed along coastal regions of the Atlantic and Pacific Oceans. These biases indicate problems in our model's representation of hydrothermal and sedimentary dFe inputs. Several studies suggested that dFe can be released from the non-reductive Fe dissolution of continental margins (Eitel et al., 2019; Homoky et al., 2013; John et al., 2017). Moreover, the abiotic particulate Fe flux from sediments and hydrothermal vents, previously considered as refractory material and not positively impacts the dFe pool, has been shown to be prone to dissolution (Cheize et al., 2019; Fitzsimmons and Boyle, 2014; Fitzsimmons et al., 2017). These processes have not yet been included in my model. Quantifying the contribution of these processes to the total dFe pool is important, especially in the Southern Ocean where the dust deposition of dFe is low and phytoplankton is Fe-limited. Recent observations around the Antarctic Circumpolar Current showed evidence of two massive phytoplankton blooms triggered by the upwelling of hydrothermally influenced deep water, potentially fueling the ocean carbon dioxide uptake (Ardyna et al., 2019).

7.2 What are the impacts of the anthropogenic Fe deposition on marine ecosystems?

Human activities have been intensifying the atmospheric input of dFe and N into the ocean (Baker et al., 2017; Duce et al., 2008; Mahowald et al., 2009) with important consequences for the marine ecosystem. Previous modeling studies (Guieu et al., 2019; Ito et al., 2016; Krishnamurthy et al., 2009, 2007) on the topic concluded that this anthropogenic nutrient deposition stimulates N fixation in the subtropical Pacific, enhances organic carbon export in the Southern Ocean, and exacerbates O_2 consumption in the tropical Pacific Ocean. However, these studies incorporated an incomplete parameterization of the ocean Fe cy-

cling due to the sparsity of ocean Fe data at that time, which may cause significant uncertainty in their results (Tagliabue et al., 2016).

In chapter 6, I used a state-of-the-art ocean ecosystem model coupled with the new Fe scheme to investigate the impact of anthropogenic atmospheric N and dFe deposition on the Indian Ocean where phytoplankton is limited by N and/or P in the north and by Fe in the south. The ecosystem model represented two grazers and six major phytoplankton types: diatoms, coccolithophores, large eukaryotes, *prochlorococcus*, other pico-phytoplankton, and diazotrophs (Dutkiewicz et al., 2014). Atmospheric deposition fields of N and dFe into the ocean under pre-industrial and industrial conditions were derived from atmospheric chemical transport model GEOS-Chem (Johnson and Meskhidze, 2013). I performed several equilibrium sensitivity simulations in which the ocean was forced under the pre-industrial deposition of N and dFe, then under the industrial deposition of N and dFe, separately and together. I found that the impact of anthropogenic N input was relatively minor. In contrast, the anthropogenic dFe input enhanced diatoms growth poleward of 40°S by relieving Fe-limitation in this region. This increase in diatoms growth led to an increase in the ocean carbon uptake in the Southern Ocean sector of the Indian Ocean. However, the diatoms growth decreased north of 40°S because diatoms were outcompeted by calcifying coccolithophores. The decrease in diatoms weakened the organic carbon flux, whereas the intensified growth of coccolithophores strengthened the calcium carbonate flux. This shift in the phytoplankton structure and carbon export caused the ocean carbon (CO_2) uptake to decrease in this region. Taken together, these changes led to a decrease in the total CO_2 uptake in the Indian Ocean.

Even though our study used a much improved ocean Fe scheme than previous modeling work, it is far from perfect. Specifically, our ligand parameterization is still simple and should be considered as only a first step toward a mechanistic scheme, such as that developed by Völker and Tagliabue, (2015). Our current understanding of ligand suggests a continuum of ligand classes encompassing a diverse range of production pathways and

binding strength rather than a few discrete classes (Hassler et al., 2017). Another worth-testing hypothesis is that organic ligands are linked to a spectrum of DOC types in the ocean, characterized by their different lifetimes (Hansell, 2013). At the moment, ligand models are poorly constrained due to the sparsity of ligand data. In this regard, future ligand measurements along ocean transects such as those done by Buck et al., (2018) and Gerringa et al., (2016) would be of great benefit. In general, gaps in our ligand knowledge could propagate to significant biases in model projections of ocean responses to human perturbations.

REFERENCES

Adly, Carol L., Jean-Eric Tremblay, Rodney T. Powell, Evelyn Armstrong, Graham Peers, and Neil M. Price (2015). "Response of heterotrophic bacteria in a mesoscale iron enrichment in the northeast subarctic Pacific Ocean". In: *Limnology and Oceanography* 60.1, pp. 136–148.

Anderson, R. F., H. Cheng, R. L. Edwards, M. Q. Fleisher, C. T. Hayes, K.-F. Huang, D. Kadko, P. J. Lam, W. M. Landing, Y. Lao, Y. Lu, C. I. Measures, S. B. Moran, P. L. Morton, D. C. Ohnemus, L. F. Robinson, and R. U. Shelley (2016). "How well can we quantify dust deposition to the ocean?" In: *Philosophical Transactions of the Royal Society A: Mathematical, Physical and Engineering Sciences* 374.2081.

Anderson, R. F., Edward MAwji, Gregory A. Cutter, C. I. Measures, and Catherine Jeandel (2014). "GEOTRACES: Changing the way we explore ocean chemistry". In: *Oceanography* 27.1, pp. 50–61.

Archer, D. E. and K. Johnson (2000). "A model of the iron cycle in the ocean". In: *Global Biogeochemical Cycles* 14.1, pp. 269–279.

Ardyna, Mathieu, Léo Lacour, Sara Sergi, Francesco d́ Ovidio, Jean-Baptiste Sallée, Mathieu Rembauville, Stéphane Blain, Alessandro Tagliabue, Reiner Schlitzer, Catherine Jeandel, Kevin Robert Arrigo, and Hervé Claustre (2019). "Hydrothermal vents trigger massive phytoplankton blooms in the Southern Ocean". In: *Nature Communications* 10.1, p. 2451.

Baker, A. R., M. Kanakidou, K. E. Altieri, N. Daskalakis, G. S. Okin, S. Myriokefalitakis, F. Dentener, M. Uematsu, M. M. Sarin, R. A. Duce, J. N. Galloway, W. C. Keene, A. Singh, L. Zamora, J. F. Lamarque, S. C. Hsu, S. S. Rohekar, and J. M. Prospero (2017). "Observation- and model-based estimates of particulate dry nitrogen deposition to the oceans". In: *Atmos. Chem. Phys.* 17.13, pp. 8189–8210.

Barbeau, K., E. L. Rue, K. W. Bruland, and A. Butler (2001). "Photochemical cycling of iron in the surface ocean mediated by microbial iron(iii)-binding ligands". In: *Nature* 413.6854, pp. 409–413.

Behrenfeld, Michael J. and Paul G. Falkowski (1997). "A consumer's guide to phytoplankton primary productivity models". In: *Limnology and Oceanography* 42.7, pp. 1479–1491.

Berg, Constant M. G. van den (1995). "Evidence for organic complexation of iron in seawater". In: *Marine Chemistry* 50.1, pp. 139–157.

Blain, Stéphane. and A. Tagliabue (2016). "Analytical Methods". In: *Iron Cycle in Oceans*, pp. 23–34.

Boiteau, Rene M. and Daniel J. Repeta (2015). "An extended siderophore suite from Synechococcus sp. PCC 7002 revealed by LC-ICPMS-ESIMS". In: *Metallomics* 7.5, pp. 877–884.

Boyd, P. W. and M. J. Ellwood (2010). "The biogeochemical cycle of iron in the ocean". In: *Nature Geosci* 3.10, pp. 675–682.

Boyd, P. W., E. Ibisanmi, S. G. Sander, K. A. Hunter, and G. A. Jackson (2010). "Remineralization of upper ocean particles: Implications for iron biogeochemistry". In: *Limnology and Oceanography* 55.3, pp. 1271–1288.

Boyd, P. W. and A. Tagliabue (2015). "Using the L* concept to explore controls on the relationship between paired ligand and dissolved iron concentrations in the ocean". In: *Marine Chemistry* 173, pp. 52–66.

Boyd, Philip W., Michael J. Ellwood, Alessandro Tagliabue, and Benjamin S. Twining (2017). "Biotic and abiotic retention, recycling and remineralization of metals in the ocean". In: *Nature Geosci* 10.3, pp. 167–173.

Boyd, Philip W., Andrew J. Watson, Cliff S. Law, Edward R. Abraham, Thomas Trull, Rob Murdoch, Dorothee C. E. Bakker, Andrew R. Bowie, K. O. Buesseler, Hoe Chang, Matthew Charette, Peter Croot, Ken Downing, Russell Frew, Mark Gall, Mark Hadfield, Julie Hall, Mike Harvey, Greg Jameson, Julie LaRoche, Malcolm Liddicoat, Roger Ling, Maria T. Maldonado, R. Michael McKay, Scott Nodder, Stu Pickmere, Rick Pridmore, Steve Rintoul, Karl Safi, Philip Sutton, Robert Strzepek, Kim Tanneberger, Suzanne Turner, Anya Waite, and John Zeldis (2000). "A mesoscale phytoplankton bloom in the polar Southern Ocean stimulated by iron fertilization". In: *Nature* 407.6805, pp. 695–702.

Boye, Marie, Constant M. G. van den Berg, Jeroen T. M. de Jong, Harry Leach, Peter Croot, and Hein J. W. de Baar (2001). "Organic complexation of iron in the Southern Ocean". In: *Deep Sea Research Part I: Oceanographic Research Papers* 48.6, pp. 1477–1497.

Boyle, Edward A., Robert F. Anderson, Gregory A. Cutter, Rana Fine, William J. Jenkins, and Mak Saito (2015). "Introduction to the U.S. GEOTRACES North Atlantic Transect (GA-03): USGT10 and USGT11 cruises". In: *Deep Sea Research Part II: Topical Studies in Oceanography* 116, pp. 1–5.

Browning, Thomas J., E. P. Achterberg, J. C. Yong, I. Rapp, C. Utermann, A. Engel, and C. M. Moore (2017). "Iron limitation of microbial phosphorus acquisition in the tropical North Atlantic". In: *Nature Communications* 8, p. 15465.

Buck, Kristen N., Peter N. Sedwick, Bettina Sohst, and Craig A. Carlson (2018). "Organic complexation of iron in the eastern tropical South Pacific: Results from US GEOTRACES Eastern Pacific Zonal Transect (GEOTRACES cruise GP16)". In: *Marine Chemistry* 201, pp. 229–241.

Buck, Kristen N., Karen E. Selph, and Katherine A. Barbeau (2010). "Iron-binding ligand production and copper speciation in an incubation experiment of Antarctic Peninsula shelf waters from the Bransfield Strait, Southern Ocean". In: *Marine Chemistry* 122.1-4, pp. 148–159.

Buck, Kristen N., Bettina Sohst, and Peter N. Sedwick (2015). "The organic complexation of dissolved iron along the U.S. GEOTRACES (GA03) North Atlantic Section". In: *Deep Sea Research Part II: Topical Studies in Oceanography* 116, pp. 152–165.

Cheize, M., H. F. Planquette, J. N. Fitzsimmons, E. Pelleter, R. M. Sherrell, C. Lambert, E. Bucciarelli, G. Sarthou, M. Le Goff, C. Liorzou, S. Chéron, E. Viollier, and N. Gayet (2019). "Contribution of resuspended sedimentary particles to dissolved iron and manganese in the ocean: An experimental study". In: *Chemical Geology* 511, pp. 389–415.

Conway, Tim M., Douglas S. Hamilton, Rachel U. Shelley, Ana M. Aguilar-Islas, William M. Landing, Natalie M. Mahowald, and Seth G. John (2019). "Tracing and constraining anthropogenic aerosol iron fluxes to the North Atlantic Ocean using iron isotopes". In: *Nature Communications* 10.1, p. 2628.

Conway, Tim M. and Seth G. John (2014). "Quantification of dissolved iron sources to the North Atlantic Ocean". In: *Nature* 511.7508, pp. 212–215.

Conway, Tim M., Jaime B. Palter, and Gregory F. de Souza (2018). "Gulf Stream rings as a source of iron to the North Atlantic subtropical gyre". In: *Nature Geoscience*.

Dale, A. W., L. Nickelsen, F. Scholz, C. Hensen, A. Oschlies, and K. Wallmann (2015). "A revised global estimate of dissolved iron fluxes from marine sediments". In: *Global Biogeochemical Cycles* 29.5, pp. 691–707.

Duce, R. A., J. LaRoche, K. Altieri, K. R. Arrigo, A. R. Baker, D. G. Capone, S. Cornell, F. Dentener, J. Galloway, R. S. Ganeshram, R. J. Geider, T. Jickells, M. M. Kuypers, R. Langlois, P. S. Liss, S. M. Liu, J. J. Middelburg, C. M. Moore, S. Nickovic, A. Oschlies, T. Pedersen, J. Prospero, R. Schlitzer, S. Seitzinger, L. L. Sorensen, M. Uematsu, O. Ulloa, M. Voss, B. Ward, and L. Zamora (2008). "Impacts of Atmospheric Anthropogenic Nitrogen on the Open Ocean". In: *Science* 320.5878, pp. 893–897.

Duce, Robert A. and Neil W. Tindale (1991). "Atmospheric transport of iron and its deposition in the ocean". In: *Limnology and Oceanography* 36.8, pp. 1715–1726.

Dutay, J. C., A. Tagliabue, I. Kriest, and M. M. P. van Hulten (2015). "Modelling the role of marine particle on large scale 231Pa, 230Th, Iron and Aluminium distributions". In: *Progress in Oceanography* 133, pp. 66–72.

Dutkiewicz, S., M. J. Follows, and P. Parekh (2005). "Interactions of the iron and phosphorus cycles: A three-dimensional model study". In: *Global Biogeochemical Cycles* 19.1, GB1021.

Dutkiewicz, S., A. E. Hickman, O. Jahn, W. W. Gregg, C. B. Mouw, and M. J. Follows (2015). "Capturing optically important constituents and properties in a marine biogeochemical and ecosystem model". In: *Biogeosciences* 12.14, pp. 4447–4481.

Dutkiewicz, S., J. R. Scott, and M. J. Follows (2013). "Winners and losers: Ecological and biogeochemical changes in a warming ocean". In: *Global Biogeochemical Cycles* 27.2, pp. 463–477.

Dutkiewicz, S., B. A. Ward, F. Monteiro, and M. J. Follows (2012). "Interconnection of nitrogen fixers and iron in the Pacific Ocean: Theory and numerical simulations". In: *Global Biogeochemical Cycles* 26.1.

Dutkiewicz, S., B. A. Ward, J. R. Scott, and M. J. Follows (2014). "Understanding predicted shifts in diazotroph biogeography using resource competition theory". In: *Biogeosciences* 11.19, pp. 5445–5461.

Eitel, Eryn, Shannon Owings, Keaton Belli, J.S. Beckler, A. Williams, B.P. Fields, M. Brown, J. Craig, O. Studebaker, D.B. Nuzzio, and M. Taillefert (2019). "Iron flux and speciation in continental margin sediments not exposed to major upwelling or riverine inputs." In: *In Review*.

Ellwood, Michael J., Andrew R. Bowie, Alex Baker, Melanie Gault-Ringold, Christel Hassler, Cliff S. Law, William A. Maher, Andrew Marriner, Scott Nodder, Sylvia Sander, Craig Stevens, Ashley Townsend, Pier van der Merwe, E. Malcolm S. Woodward, Kathrin Wuttig, and Philip W. Boyd (2018). "Insights Into the Biogeochemical Cycling of Iron, Nitrate, and Phosphate Across a 5,300 km South Pacific Zonal Section (153°E-150°W)". In: *Global Biogeochemical Cycles*, n/a–n/a.

Elrod, Virginia A., William M. Berelson, Kenneth H. Coale, and Kenneth S. Johnson (2004). "The flux of iron from continental shelf sediments: A missing source for global budgets". In: *Geophysical Research Letters* 31.12, p. L12307.

Fitzsimmons, Jessica N. and Edward A. Boyle (2014). "Both soluble and colloidal iron phases control dissolved iron variability in the tropical North Atlantic Ocean". In: *Geochimica et Cosmochimica Acta* 125, pp. 539–550.

Fitzsimmons, Jessica N., Edward A. Boyle, and William J. Jenkins (2014). "Distal transport of dissolved hydrothermal iron in the deep South Pacific Ocean". In: *Proceedings of the National Academy of Sciences* 111.47, pp. 16654–16661.

Fitzsimmons, Jessica N., Gonzalo G. Carrasco, Jingfeng Wu, Saeed Roshan, Mariko Hatta, Christopher I. Measures, Tim M. Conway, Seth G. John, and Edward A. Boyle (2015). "Partitioning of dissolved iron and iron isotopes into soluble and colloidal phases along the GA03 GEOTRACES North Atlantic Transect". In: *Deep Sea Research Part II: Topical Studies in Oceanography* 116, pp. 130–151.

Fitzsimmons, Jessica N., Tim M. Conway, Jong-Mi Lee, Richard Kayser, Kristen M. Thyng, Seth G. John, and Edward A. Boyle (2016). "Dissolved iron and iron isotopes in the southeastern Pacific Ocean". In: *Global Biogeochemical Cycles* 30, pp. 1372–1395.

Fitzsimmons, Jessica N., Seth G. John, Christopher M. Marsay, Colleen L. Hoffman, Sarah L. Nicholas, Brandy M. Toner, Christopher R. German, and Robert M. Sherrell (2017). "Iron persistence in a distal hydrothermal plume supported by dissolved-particulate exchange". In: *Nature Geosci* advance online publication.

Fowler, Scott W. and George A. Knauer (1986). "Role of large particles in the transport of elements and organic compounds through the oceanic water column". In: *Progress in Oceanography* 16.3, pp. 147–194.

Frants, Marina, Mark Holzer, Timothy DeVries, and Richard Matear (2016). "Constraints on the global marine iron cycle from a simple inverse model". In: *Journal of Geophysical Research: Biogeosciences* 121.1, pp. 28–51.

Galbraith, E. D., A. Gnanadesikan, J. P. Dunne, and M. R. Hiscock (2010). "Regional impacts of iron-light colimitation in a global biogeochemical model". In: *Biogeosciences* 7.3, pp. 1043–1064.

Garcia, Herncin E. and Louis I. Gordon (1992). "Oxygen solubility in seawater: Better fitting equations". In: *Limnology and Oceanography* 37.6, pp. 1307–1312.

Garcia, Herncin E., R.A. Locarini, T.P. Boyer, J.I. Antono, O.K. Baranova, M.M. Zweng, J.R. Reagan, and D.R. Johnson (2014). "World Ocean Atlas 2013, Volume 3: Dissolved Oxygen, Apparent Oxygen Utilization, and Oxygen Saturation". In: *S. Levitus, Ed., A. Mishonov Technical Ed.;* 3, NOAA Atlas NESDIS 75, 27 pp.

Geider, Richard J., Hugh L. MacIntyre, and Todd M. Kana (1998). "A dynamic regulatory model of phytoplanktonic acclimation to light, nutrients, and temperature". In: *Limnology and Oceanography* 43.4, pp. 679–694.

Gent, Peter R. and James C. McWilliams (1990). "Isopycnal Mixing in Ocean Circulation Models". In: *Journal of Physical Oceanography* 20.1, pp. 150–155.

Gerringa, L. J. A., M. J. A. Rijkenberg, V. Schoemann, P. Laan, and H. J. W. de Baar (2015). "Organic complexation of iron in the West Atlantic Ocean". In: *Marine Chemistry* 177, Part 3, pp. 434–446.

Gerringa, Loes J.A., Micha J.A. Rijkenberg, Johann Bown, Andrew R Margolin, Patrick Laan, and Hein J. W. De Baar (2016). "Fe-binding dissolved organic ligands in the oxic and suboxic waters of the Black Sea". In: *Frontiers in Marine Science* 3.

Gledhill, Martha and Kristen Buck (2012). "The Organic Complexation of Iron in the Marine Environment: A Review". In: *Frontiers in Microbiology* 3.69.

Guieu, Cécile, Muchamad Al Azhar, Olivier Aumont, Natalie Mahowald, Marina Levy, Christian Ethé, and Zouhair Lachkar (2019). "Major Impact of Dust Deposition on the Productivity of the Arabian Sea". In: *Geophysical Research Letters* 46.12, pp. 6736–6744.

Hansell, Dennis A. (2013). "Recalcitrant Dissolved Organic Carbon Fractions". In: *Annual Review of Marine Science* 5.1, pp. 421–445.

Hassler, Christel S., Véronique Schoemann, Carol Mancuso Nichols, Edward C. V. Butler, and Philip W. Boyd (2011). "Saccharides enhance iron bioavailability to Southern Ocean phytoplankton". In: *Proceedings of the National Academy of Sciences* 108.3, pp. 1076–1081.

Hassler, Christel, Constant van den Berg, and Philip Boyd (2017). "Towards a regional classification to provide a more inclusive examination of the ocean biogeochemistry of iron-binding ligands". In: *Frontiers in Marine Science* 4.19.

Hatta, Mariko, Chris I. Measures, Jingfeng Wu, Saeed Roshan, Jessica N. Fitzsimmons, Peter Sedwick, and Pete Morton (2015). "An overview of dissolved Fe and Mn distributions during the 2010-2011 U.S. GEOTRACES north Atlantic cruises: GEOTRACES GA03". In: *Deep Sea Research Part II: Topical Studies in Oceanography* 116, pp. 117–129.

Henderson, G.M., R. F. Anderson, J. Adkins, E.A. Andersson P. Boyle, Gregory A. Cutter, H. J. W. De Baar, A. Eisenhauer, Martin Frank, R. Francois, Kristin Orians, Toshitaka Gamo, Chris German, William J. Jenkins, James Moffett, Catherine Jeandel, T. D. Jickells, C. I. Measures, J. K. Moore, and A. Oschlies (2007). "GEOTRACES - An international study of the global marine biogeochemical cycles of trace elements and their isotopes". In: *Chemie der Erde - Geochemistry* 67.2, pp. 85–131.

Hickman, A. E., S. Dutkiewicz, R. G. Williams, and M. J. Follows (2010). "Modelling the effects of chromatic adaptation on phytoplankton community structure in the oligotrophic ocean". In: *Marine Ecology Progress Series* 406, pp. 1–17.

Holzer, Mark, Marina Frants, and Benoît Pasquier (2016). "The age of iron and iron source attribution in the ocean". In: *Global Biogeochemical Cycles* 30.10, pp. 1454–1474.

Homoky, William B., Seth G. John, Tim M. Conway, and Rachel A. Mills (2013). "Distinct iron isotopic signatures and supply from marine sediment dissolution". In: *Nature Communications* 4.1, p. 2143.

Honeyman, B. D. and P. H. Santschi (1989). "A Brownian-pumping model for oceanic trace metal scavenging: Evidence from Th isotopes". In: *Journal of Marine Research* 47.4, pp. 951–992.

Honeyman, Bruce D., Laurie S. Balistrieri, and James W. Murray (1988). "Oceanic trace metal scavenging: the importance of particle concentration". In: *Deep Sea Research Part A. Oceanographic Research Papers* 35.2, pp. 227–246.

Hunter, Keith A. and Philip W. Boyd (2007). "Iron-binding ligands and their role in the ocean biogeochemistry of iron". In: *Environmental Chemistry* 4.4, pp. 221–232.

Hutchins, D. A. and P. W. Boyd (2016). "Marine phytoplankton and the changing ocean iron cycle". In: *Nature Clim. Change* 6.12, pp. 1072–1079.

Hutchins, David A., Amy E. Witter, Alison Butler, and George W. Luther (1999). "Competition among marine phytoplankton for different chelated iron species". In: *Nature* 400.6747, pp. 858–861.

Ibisanmi, Enitan, Sylvia G. Sander, Philip W. Boyd, Andrew R. Bowie, and Keith A. Hunter (2011). "Vertical distributions of iron-(III) complexing ligands in the Southern Ocean". In: *Deep Sea Research Part II: Topical Studies in Oceanography* 58.21, pp. 2113–2125.

Ingall, Ellery D., Julia M. Diaz, Amelia F. Longo, Michelle Oakes, Lydia Finney, Stefan Vogt, Barry Lai, Patricia L. Yager, Benjamin S. Twining, and Jay A. Brandes (2013). "Role of biogenic silica in the removal of iron from the Antarctic seas". In: *Nat Commun* 4.

Ito, T., A. Nenes, M. S. Johnson, N. Meskhidze, and C. Deutsch (2016). "Acceleration of oxygen decline in the tropical Pacific over the past decades by aerosol pollutants". In: *Nature Geosci* 9.6, pp. 443–447.

Jackson, George A. and Adrian B. Burd (2015). "Simulating aggregate dynamics in ocean biogeochemical models". In: *Progress in Oceanography* 133, pp. 55–65.

Jeandel, Catherine, Michiel Rutgers van der Loeff, Phoebe J. Lam, Matthieu Roy-Barman, Robert M. Sherrell, Sven Kretschmer, Chris German, and Frank Dehairs (2015). "What did we learn about ocean particle dynamics in the GEOSECS-JGFOS era?" In: *Progress in Oceanography* 133, pp. 6–16.

Jickells, T. D., Z. S. An, K. K. Andersen, A. R. Baker, G. Bergametti, N. Brooks, J. J. Cao, P. W. Boyd, R. A. Duce, K. A. Hunter, H. Kawahata, N. Kubilay, J. laRoche, P. S. Liss, N. Mahowald, J. M. Prospero, A. J. Ridgwell, I. Tegen, and R. Torres (2005). "Global Iron Connections Between Desert Dust, Ocean Biogeochemistry, and Climate". In: *Science* 308.5718, pp. 67–71.

John, Seth G., Joshua Helgoe, Emily Townsend, Tom Weber, Tim DeVries, Alessandro Tagliabue, Keith Moore, Phoebe Lam, Chris M. Marsay, and Claire Till (2017). "Biogeochemical cycling of Fe and Fe stable isotopes in the Eastern Tropical South Pacific". In: *Marine Chemistry*.

Johnson, Kenneth S., Francisco P. Chavez, and Gernot E. Friederich (1999). "Continental-shelf sediment as a primary source of iron for coastal phytoplankton". In: *Nature* 398.6729, pp. 697–700.

Johnson, Kenneth S., R. Michael Gordon, and Kenneth H. Coale (1997). "What controls dissolved iron concentrations in the world ocean?" In: *Marine Chemistry* 57.3, pp. 137–161.

Johnson, M. S. and N. Meskhidze (2013). "Atmospheric dissolved iron deposition to the global oceans: effects of oxalate-promoted Fe dissolution, photochemical redox cycling, and dust mineralogy". In: *Geosci. Model Dev.* 6.4, pp. 1137–1155.

Jones, Daniel C., Harry J. Holt, Andrew J. S. Meijers, and Emily Shuckburgh (2019). "Unsupervised Clustering of Southern Ocean Argo Float Temperature Profiles". In: *Journal of Geophysical Research: Oceans* 124.1, pp. 390–402.

Kalnay, E., M. Kanamitsu, R. Kistler, W. Collins, D. Deaven, L. Gandin, M. Iredell, S. Saha, G. White, J. Woollen, Y. Zhu, M. Chelliah, W. Ebisuzaki, W. Higgins, J. Janowiak, K. C. Mo, C. Ropelewski, J. Wang, A. Leetmaa, R. Reynolds, Roy Jenne, and Dennis Joseph (1996). "The NCEP/NCAR 40-Year Reanalysis Project". In: *Bulletin of the American Meteorological Society* 77.3, pp. 437–472.

Krishnamurthy, A., J. K. Moore, N. Mahowald, C. Luo, S. C. Doney, K. Lindsay, and C. S. Zender (2009). "Impacts of increasing anthropogenic soluble iron and nitrogen deposition on ocean biogeochemistry". In: *Global Biogeochemical Cycles* 23.3.

Krishnamurthy, A., J. K. Moore, C. S. Zender, and C. Luo (2007). "Effects of atmospheric inorganic nitrogen deposition on ocean biogeochemistry". In: *Journal of Geophysical Research: Biogeosciences* 112.G2.

Krumhardt, K. M., N. S. Lovenduski, N. M. Freeman, and N. R. Bates (2016). "Apparent increase in coccolithophore abundance in the subtropical North Atlantic from 1990 to 2014". In: *Biogeosciences* 13.4, pp. 1163–1177.

Krumhardt, K. M., N. S. Lovenduski, M. C. Long, M. Levy, K. Lindsay, J. K. Moore, and C. Nissen (2019). "Coccolithophore Growth and Calcification in an Acidified Ocean: Insights From Community Earth System Model Simulations". In: *Journal of Advances in Modeling Earth Systems* 11.5, pp. 1418–1437.

Krumhardt, Kristen M., Nicole S. Lovenduski, M. Debora Iglesias-Rodriguez, and Joan A. Kleypas (2017a). "Coccolithophore growth and calcification in a changing ocean". In: *Progress in Oceanography* 159, pp. 276–295.

Krumhardt, Kristen M., Nicole S. Lovenduski, Matthew C. Long, and Keith Lindsay (2017b). "Avoidable impacts of ocean warming on marine primary production: Insights from the CESM ensembles". In: *Global Biogeochemical Cycles* 31.1, pp. 114–133.

Kubat, M. (2015). *Introduction to Machine Learning*. 2nd. New York: Spring Publishers.

Kustka, Adam B., Bethan M. Jones, Mariko Hatta, M. Paul Field, and Allen J. Milligan (2015). "The influence of iron and siderophores on eukaryotic phytoplankton growth rates and community composition in the Ross Sea". In: *Marine Chemistry* 173, pp. 195–207.

Laglera, Luis M. and Constant M. G. van den Berg (2009). "Evidence for geochemical control of iron by humic substances in seawater". In: *Limnology and Oceanography* 54.2, pp. 610–619.

Large, W. G., J. C. McWilliams, and S. C. Doney (1994). "Oceanic vertical mixing: A review and a model with a nonlocal boundary layer parameterization". In: *Reviews of Geophysics* 32.4, pp. 363–403.

Laws, Edward A., Eurico D'Sa, and Puneeta Naik (2011). "Simple equations to estimate ratios of new or export production to total production from satellite-derived estimates of sea surface temperature and primary production". In: *Limnology and Oceanography: Methods* 9.12, pp. 593–601.

Liu, Xuewu and Frank J. Millero (2002). "The solubility of iron in seawater". In: *Marine Chemistry* 77.1, pp. 43–54.

MacQueen, J. B. (1967). "Some methods for classification and analysis of multivariate observations". In: *Proceedings of 5-th Berkeley Symposium on Mathematical Statistics and Probability*. Vol. 1. University of California Press., pp. 281–297.

Macrellis, Heather M., Charles G. Trick, Eden L. Rue, Geoffrey Smith, and Kenneth W. Bruland (2001). "Collection and detection of natural iron-binding ligands from seawater". In: *Marine Chemistry* 76.3, pp. 175–187.

Mahowald, N., S. Engelstaedter, C. Luo, A. Sealy, P. Artaxo, Claudia Benitez-Nelson, Sophie Bonnet, Ying Chen, Patrick Y. Chuang, David D. Cohen, Francois Dulac, Barak Herut, Anne M. Johansen, Nilgun Kubilay, Remi Losno, Willy Maenhaut, Adina Paytan, Joseph M. Prospero, Lindsey M. Shank, and Ronald L. Siefert (2009). "Atmospheric Iron Deposition: Global Distribution, Variability, and Human Perturbations". In: *Annual Review of Marine Science* 1.1, pp. 245–278.

Mahowald, Natalie M., Rachel Scanza, Janice Brahney, Christine L. Goodale, Peter G. Hess, J. Keith Moore, and Jason Neff (2017). "Aerosol Deposition Impacts on Land and Ocean Carbon Cycles". In: *Current Climate Change Reports* 3.1, pp. 16–31.

Marshall, John, Alistair Adcroft, Chris Hill, Lev Perelman, and Curt Heisey (1997a). "A finite-volume, incompressible Navier Stokes model for studies of the ocean on parallel computers". In: *Journal of Geophysical Research: Oceans* 102.C3, pp. 5753–5766.

Marshall, John, Chris Hill, Lev Perelman, and Alistair Adcroft (1997b). "Hydrostatic, quasi-hydrostatic, and nonhydrostatic ocean modeling". In: *Journal of Geophysical Research: Oceans* 102.C3, pp. 5733–5752.

Martin, John H., George A. Knauer, David M. Karl, and William W. Broenkow (1987). "VERTEX: carbon cycling in the northeast Pacific". In: *Deep Sea Research Part A. Oceanographic Research Papers* 34.2, pp. 267–285.

Mawji, Edward, Reiner Schlitzer, Elena Masferrer Dodas, Cyril Abadie, Wafa Abouchami, Robert F. Anderson, Oliver Baars, Karel Bakker, Mark Baskaran, Nicholas R. Bates, Katrin Bluhm, Andrew Bowie, Johann Bown, Marie Boye, Edward A. Boyle, Pierre Branellec, Kenneth W. Bruland, Mark A. Brzezinski, Eva Bucciarelli, Ken Buesseler, Edward Butler, Pinghe Cai, Damien Cardinal, Karen Casciotti, Joaquin Chaves, Hai Cheng, Fanny Chever, Thomas M. Church, Albert S. Colman, Tim M. Conway, Peter L. Croot, Gregory A. Cutter, Hein J. W. de Baar, Gregory F. de Souza, Frank Dehairs, Feifei Deng, Huong Thi Dieu, Gabriel Dulaquais, Yolanda Echegoyen-Sanz, R. Lawrence Edwards, Eberhard Fahrbach, Jessica Fitzsimmons, Martin Fleisher, Martin Frank, Jana Friedrich, François Fripiat, Stephen J. G. Galer, Toshitaka Gamo, Ester Garcia Solsona, Loes J. A. Gerringa, José Marcus Godoy, Santiago Gonzalez, Emilie Grossteffan, Mariko Hatta, Christopher T. Hayes, Maija Iris Heller, Gideon Henderson, Kuo-Fang Huang, Catherine Jeandel, William J. Jenkins, Seth John, Timothy C. Kenna, Maarten Klunder, Sven Kretschmer, Yuichiro Kumamoto, Patrick Laan, Marie Labatut, Francois Lacan, Phoebe J. Lam, Delphine Lannuzel, Frederique le Moigne, Oliver J. Lechtenfeld, Maeve C. Lohan, Yanbin Lu, Pere Masqué, Charles R. McClain, Christopher Measures, Rob Middag, James Moffett, Alicia Navidad, Jun Nishioka, Abigail Noble, Hajime Obata, Daniel C. Ohnemus, Stephanie Owens, Frédéric Planchon, Catherine Pradoux, Viena Puigcorbé, Paul Quay, Amandine Radic, Mark Rehkämper, Tomas Remenyi, Micha J. A. Rijkenberg, Stephen Rintoul, Laura F. Robinson, Tobias Roeske, Mark Rosenberg, Michiel Rutgers van der Loeff, Evgenia Ryabenko, Mak A.

Saito, et al. (2015). “The GEOTRACES Intermediate Data Product 2014”. In: *Marine Chemistry* 177, Part 1, pp. 1–8.

Middag, R., M. M. P. van Hulten, H. M. Van Aken, M. J. A. Rijkenberg, L. J. A. Gerringa, P. Laan, and H. J. W. de Baar (2015). “Dissolved aluminium in the ocean conveyor of the West Atlantic Ocean: Effects of the biological cycle, scavenging, sediment resuspension and hydrography”. In: *Marine Chemistry* 177, Part 1, pp. 69–86.

Misumi, Kazuhiro, Keith Lindsay, J. Keith Moore, Scott C. Doney, Daisuke Tsumune, and Yoshikatsu Yoshida (2013). “Humic substances may control dissolved iron distributions in the global ocean: Implications from numerical simulations”. In: *Global Biogeochemical Cycles* 27.2, pp. 450–462.

Moore, C. M., M. M. Mills, K. R. Arrigo, I. Berman-Frank, L. Bopp, P. W. Boyd, E. D. Galbraith, R. J. Geider, C. Guieu, S. L. Jaccard, T. D. Jickells, J. La Roche, T. M. Lenton, N. M. Mahowald, E. Maranon, I. Marinov, J. K. Moore, T. Nakatsuka, A. Oschlies, M. A. Saito, T. F. Thingstad, A. Tsuda, and O. Ulloa (2013). “Processes and patterns of oceanic nutrient limitation”. In: *Nature Geosci* 6.9, pp. 701–710.

Moore, C Mark., Matthew M. Mills, Eric P. Achterberg, Richard J. Geider, Julie LaRoche, Mike I. Lucas, Elaine L. McDonagh, Xi Pan, Alex J. Poulton, Micha J. A. Rijkenberg, David J. Suggett, Simon J. Ussher, and E. Malcolm S. Woodward (2009). “Large-scale distribution of Atlantic nitrogen fixation controlled by iron availability”. In: *Nature Geoscience* 2, p. 867.

Moore, C Mark., Matthew M. Mills, Milne Angela, Langlois Rebecca, Achterberg Eric P., Lochte Karin, Geider Richard J., and La Roche Julie (2006). “Iron limits primary productivity during spring bloom development in the central North Atlantic”. In: *Global Change Biology* 12.4, pp. 626–634.

Moore, J. K. and O. Braucher (2008). “Sedimentary and mineral dust sources of dissolved iron to the world ocean”. In: *Biogeosciences* 5.3, pp. 631–656.

Nishioka, J., H. Obata, and D. Tsumune (2013). “Evidence of an extensive spread of hydrothermal dissolved iron in the Indian Ocean”. In: *Earth and Planetary Science Letters* 361, pp. 26–33.

Nishioka, Jun and Hajime Obata (2017). “Dissolved iron distribution in the western and central subarctic Pacific: HNLC water formation and biogeochemical processes”. In: *Limnology and Oceanography* 62.5, pp. 2004–2022.

Noble, Abigail E., Carl H. Lamborg, Dan C. Ohnemus, Phoebe J. Lam, Tyler J. Goepfert, Chris I. Measures, Caitlin H. Frame, Karen L. Casciotti, Giacomo R. DiTullio, Joe Jennings, and Mak A. Saito (2012). “Basin-scale inputs of cobalt, iron, and manganese

from the Benguela-Angola front to the South Atlantic Ocean". In: *Limnology and Oceanography* 57.4, pp. 989–1010.

Pagnone, Anna, Christoph Völker, and Ying Ye (2019). "Processes affecting dissolved iron across the Subtropical North Atlantic: a model study". In: *Ocean Dynamics* 69.9, pp. 989–1007.

Parekh, P., M. J. Follows, and E. A. Boyle (2005). "Decoupling of iron and phosphate in the global ocean". In: *Global Biogeochemical Cycles* 19.2, GB2020.

Pham, Anh L. D. and T. Ito (2018). "Formation and Maintenance of the GEOTRACES Subsurface-Dissolved Iron Maxima in an Ocean Biogeochemistry Model". In: *Global Biogeochemical Cycles* 32.6, pp. 932–953.

Pham, Anh L. D. and Takamitsu Ito (2019). "Ligand Binding Strength Explains the Distribution of Iron in the North Atlantic Ocean". In: *Geophysical Research Letters* 46.13, pp. 7500–7508.

Raven, John A. (1988). "The iron and molybdenum use efficiencies of plant growth with different energy, carbon and nitrogen sources". In: *New Phytologist* 109.3, pp. 279–287.

Redi, Martha H. (1982). "Oceanic Isopycnal Mixing by Coordinate Rotation". In: *Journal of Physical Oceanography* 12.10, pp. 1154–1158.

Resing, Joseph A., Peter N. Sedwick, Christopher R. German, William J. Jenkins, James W. Moffett, Bettina M. Sohst, and Alessandro Tagliabue (2015). "Basin-scale transport of hydrothermal dissolved metals across the South Pacific Ocean". In: *Nature* 523.7559, pp. 200–203.

Revels, Brandi N., Daniel C. Ohnemus, Phoebe J. Lam, Tim M. Conway, and Seth G. John (2015). "The isotopic signature and distribution of particulate iron in the North Atlantic Ocean". In: *Deep Sea Research Part II: Topical Studies in Oceanography* 116, pp. 321–331.

Riegman, Roel, Willem Stolte, Anna A. M. Noordeloos, and Doris Slezak (2000). "Nutrient uptake and alkaline phosphatase (ec 3:1:3:1) activity of emiliania huxleyi (PRYMNESIOPHYCEAE) during growth under n and p limitation in continuous cultures". In: *Journal of Phycology* 36.1, pp. 87–96.

Rijkenberg, Micha J. A., Rob Middag, Patrick Laan, Loes J. A. Gerringa, Hendrik M. van Aken, Véronique Schoemann, Jeroen T. M. de Jong, and Hein J. W. de Baar (2014). "The Distribution of Dissolved Iron in the West Atlantic Ocean". In: *PLoS ONE* 9.6, e101323.

Rue, Eden L. and Kenneth W. Bruland (1995). "Complexation of iron(III) by natural organic ligands in the Central North Pacific as determined by a new competitive ligand equilibration/adsorptive cathodic stripping voltammetric method". In: *Marine Chemistry* 50.1, pp. 117–138.

Saito, Mak A., Abigail E. Noble, Alessandro Tagliabue, Tyler J. Goepfert, Carl H. Lamborg, and William J. Jenkins (2013). "Slow-spreading submarine ridges in the South Atlantic as a significant oceanic iron source". In: *Nature Geosci* 6.9, pp. 775–779.

Salt, L. A., S. M. A. C. van Heuven, M. E. Claus, E. M. Jones, and H. J. W. de Baar (2015). "Rapid acidification of mode and intermediate waters in the southwestern Atlantic Ocean". In: *Biogeosciences* 12.5, pp. 1387–1401.

Schlitzer, Reiner, Robert F. Anderson, Elena Masferrer Dodas, Maeve Lohan, Walter Geibert, Alessandro Tagliabue, Andrew Bowie, Catherine Jeandel, Maria T. Maldonado, William M. Landing, Donna Cockwell, Cyril Abadie, Wafa Abouchami, Eric P. Achterberg, Alison Agather, Ana Aguliar-Islas, Hendrik M. van Aken, Morten Andersen, Corey Archer, Maureen Auro, Hein J. de Baar, Oliver Baars, Alex R. Baker, Karel Bakker, Chandranath Basak, Mark Baskaran, Nicholas R. Bates, Dorothea Bauch, Pieter van Beek, Melanie K. Behrens, Erin Black, Katrin Bluhm, Laurent Bopp, Heather Bouman, Katlin Bowman, Johann Bown, Philip Boyd, Marie Boye, Edward A. Boyle, Pierre Branellec, Luke Bridgestock, Guillaume Brissebrat, Thomas Browning, Kenneth W. Bruland, Hans-Jũrgen Brumsack, Mark Brzezinski, Clifton S. Buck, Kristen N. Buck, Ken Buesseler, Abby Bull, Edward Butler, Pinghe Cai, Patricia Cámara Mor, Damien Cardinal, Craig Carlson, Gonzalo Carrasco, Núria Casacuberta, Karen L. Casciotti, Maxi Castrillejo, Elena Chamizo, Rosie Chance, Matthew A. Charette, Joaquin E. Chaves, Hai Cheng, Fanny Chever, Marcus Christl, Thomas M. Church, Ivia Closset, Albert Colman, Tim M. Conway, Daniel Cossa, Peter Croot, Jay T. Cullen, Gregory A. Cutter, Chris Daniels, Frank Dehairs, Feifei Deng, Huong Thi Dieu, Brian Duggan, Gabriel Dulaquais, Cynthia Dumousseaud, Yolanda Echegoyen-Sanz, R. Lawrence Edwards, Michael Ellwood, Eberhard Fahrbach, Jessica N. Fitzsimmons, A. Russell Flegal, Martin Q. Fleisher, Tina van de Flierdt, Martin Frank, Jana Friedrich, Francois Fripiat, Henning Fr"ollje, Stephen J. G. Galer, Toshitaka Gamo, Raja S. Ganeshram, Jordi Garcia-Orellana, Ester Garcia-Solsona, Melanie Gault-Ringold, Ejin George, et al. (2018). "The GEOTRACES Intermediate Data Product 2017". In: *Chemical Geology*.

Sedwick, P. N., T. M. Church, A. R. Bowie, C. M. Marsay, S. J. Ussher, K. M. Achilles, P. J. Lethaby, R. J. Johnson, M. M. Sarin, and D. J. McGillicuddy (2005). "Iron in the Sargasso Sea (Bermuda Atlantic Time-series Study region) during summer: Eolian imprint, spatiotemporal variability, and ecological implications". In: *Global Biogeochemical Cycles* 19.4, n/a–n/a.

Sharples, Jonathan, Jack J. Middelburg, Katja Fennel, and Timothy D. Jickells (2017). "What proportion of riverine nutrients reaches the open ocean?" In: *Global Biogeochemical Cycles* 31.1, pp. 39–58.

Solomon, Harold (1971). "On the Representation of Isentropic Mixing in Ocean Circulation Models". In: *Journal of Physical Oceanography* 1.3, pp. 233–234.

Somes, Christopher J., Angela Landolfi, Wolfgang Koeve, and Andreas Oschlies (2016). "Limited impact of atmospheric nitrogen deposition on marine productivity due to biogeochemical feedbacks in a global ocean model". In: *Geophysical Research Letters* 43.9, pp. 4500–4509.

Sonnewald, Maike, Carl Wunsch, and Patrick Heimbach (2019). "Unsupervised Learning Reveals Geography of Global Ocean Dynamical Regions". In: *Earth and Space Science* 6.5, pp. 784–794.

Stramma, Lothar, Sunke Schmidtko, Lisa A. Levin, and Gregory C. Johnson (2010). "Ocean oxygen minima expansions and their biological impacts". In: *Deep Sea Research Part I: Oceanographic Research Papers* 57.4, pp. 587–595.

Sunda, William (2012). "Feedback Interactions between Trace Metal Nutrients and Phytoplankton in the Ocean". In: *Frontiers in Microbiology* 3.204.

Tagliabue, A., O. Aumont, R. DeAth, J. P. Dunne, S. Dutkiewicz, Eric Galbraith, Kazuhiro Misumi, J. Keith Moore, Andy Ridgwell, Elliot Sherman, Charles Stock, Marcello Vichi, Christoph V"olker, and Andrew Yool (2016). "How well do global ocean biogeochemistry models simulate dissolved iron distributions?" In: *Global Biogeochemical Cycles* 30.2, pp. 149–174.

Tagliabue, A., T. Mtshali, O. Aumont, A. R. Bowie, M. B. Klunder, A. N. Roychoudhury, and S. Swart (2012). "A global compilation of dissolved iron measurements: focus on distributions and processes in the Southern Ocean". In: *Biogeosciences* 9.6, pp. 2333–2349.

Tagliabue, A., Jean-Baptiste Sallee, Andrew R. Bowie, Marina Levy, Sebastiaan Swart, and Philip W. Boyd (2014a). "Surface-water iron supplies in the Southern Ocean sustained by deep winter mixing". In: *Nature Geosci* 7.4, pp. 314–320.

Tagliabue, A. and C. Völker (2011). "Towards accounting for dissolved iron speciation in global ocean models". In: *Biogeosciences* 8.10, pp. 3025–3039.

Tagliabue, Alessandro, Olivier Aumont, and Laurent Bopp (2014b). "The impact of different external sources of iron on the global carbon cycle". In: *Geophysical Research Letters* 41.3, pp. 920–926.

Tagliabue, Alessandro, Laurent Bopp, Jean-Claude Dutay, Andrew R. Bowie, Fanny Chever, Philippe Jean-Baptiste, Eva Bucciarelli, Delphine Lannuzel, Tomas Remenyi, Geraldine Sarthou, Olivier Aumont, Marion Gehlen, and Catherine Jeandel (2010). "Hydrothermal contribution to the oceanic dissolved iron inventory". In: *Nature Geosci* 3.4, pp. 252–256.

Tagliabue, Alessandro, Andrew R. Bowie, Philip W. Boyd, Kristen N. Buck, Kenneth S. Johnson, and Mak A. Saito (2017). "The integral role of iron in ocean biogeochemistry". In: *Nature* 543.7643, pp. 51–59.

Tagliabue, Alessandro and Joseph Resing (2016). "Impact of hydrothermalism on the ocean iron cycle". In: *Philosophical Transactions of the Royal Society A: Mathematical, Physical and Engineering Sciences* 374.2081.

Tagliabue, Alessandro, Richard G. Williams, Nicholas Rogan, Eric P. Achterberg, and Philip W. Boyd (2014c). "A ventilation-based framework to explain the regeneration-scavenging balance of iron in the ocean". In: *Geophysical Research Letters* 41.20, pp. 7227–7236.

Twining, B., Sara Rauschenberg, Peter L. Morton, and Stefan Vogt (2015). "Metal contents of phytoplankton and labile particulate material in the North Atlantic Ocean". In: *Progress in Oceanography* 137, pp. 261–283.

Twining, Benjamin S. and Stephen B. Baines (2013). "The Trace Metal Composition of Marine Phytoplankton". In: *Annual Review of Marine Science* 5.1, pp. 191–215.

Twining, Benjamin S., Sara Rauschenberg, Steven E. Baer, Michael W. Lomas, Adam C. Martiny, and Olga Antipova (2019). "A nutrient limitation mosaic in the eastern tropical Indian Ocean". In: *Deep Sea Research Part II: Topical Studies in Oceanography* 166, pp. 125–140.

Velasquez, Imelda B., Enitan Ibisanmi, Elizabeth W. Maas, Philip W. Boyd, Scott Nodder, and Sylvia G. Sander (2016). "Ferrioxamine Siderophores Detected amongst Iron Binding Ligands Produced during the Remineralization of Marine Particles". In: *Frontiers in Marine Science* 3.172.

Voelker, Antje H. L., Albert Colman, Gerard Olack, Joanna J. Waniek, and David Hodell (2015). "Oxygen and hydrogen isotope signatures of Northeast Atlantic water masses". In: *Deep Sea Research Part II: Topical Studies in Oceanography* 116, pp. 89–106.

Völker, Christoph and Alessandro Tagliabue (2015). "Modeling organic iron-binding ligands in a three-dimensional biogeochemical ocean model". In: *Marine Chemistry* 173, pp. 67–77.

Vraspir, Julia M. and Alison Butler (2009). “Chemistry of Marine Ligands and Siderophores”. In: *Annual Review of Marine Science* 1.1, pp. 43–63.

Wang, Wei-Lei, J. Keith Moore, Adam C. Martiny, and François W. Primeau (2019). “Convergent estimates of marine nitrogen fixation”. In: *Nature* 566.7743, pp. 205–211.

Witter, Amy E., David A. Hutchins, Alison Butler, and George W. Luther (2000). “Determination of conditional stability constants and kinetic constants for strong model Fe-binding ligands in seawater”. In: *Marine Chemistry* 69.1, pp. 1–17.

Wu, Jingfeng and Edward Boyle (2002). “Iron in the Sargasso Sea: Implications for the processes controlling dissolved Fe distribution in the ocean”. In: *Global Biogeochemical Cycles* 16.4, pp. 331–338.

Wu, Jingfeng, Edward Boyle, William Sunda, and Liang-Saw Wen (2001). “Soluble and Colloidal Iron in the Oligotrophic North Atlantic and North Pacific”. In: *Science* 293.5531, pp. 847–849.

Wu, Jingfeng and George W. Luther (1995). “Complexation of Fe(III) by natural organic ligands in the Northwest Atlantic Ocean by a competitive ligand equilibration method and a kinetic approach”. In: *Marine Chemistry* 50.1, pp. 159–177.

Wunsch, Carl and Patrick Heimbach (2007). “Practical global oceanic state estimation”. In: *Physica D* 230, pp. 197–208.

Ye, Y. and C. Völker (2017). “On the Role of Dust-Deposited Lithogenic Particles for Iron Cycling in the Tropical and Subtropical Atlantic”. In: *Global Biogeochemical Cycles* 31.10, pp. 1543–1558.

Ye, Y., T. Wagener, C. Völker, C. Guieu, and D. A. Wolf-Gladrow (2011). “Dust deposition: iron source or sink? A case study”. In: *Biogeosciences* 8.8, pp. 2107–2124.